Wright State University
CORE Scholar

Browse all Theses and Dissertations | Theses and Dissertations

2010

Atmospheric Effects on the Propagation of MMW and Sub-MMW Radiation

John S. Cetnar
Wright State University

Follow this and additional works at: https://corescholar.libraries.wright.edu/etd_all

 Part of the Physics Commons

Repository Citation

Cetnar, John S., "Atmospheric Effects on the Propagation of MMW and Sub-MMW Radiation" (2010). *Browse all Theses and Dissertations*. 341.
https://corescholar.libraries.wright.edu/etd_all/341

This Thesis is brought to you for free and open access by the Theses and Dissertations at CORE Scholar. It has been accepted for inclusion in Browse all Theses and Dissertations by an authorized administrator of CORE Scholar. For more information, please contact library-corescholar@wright.edu.

Atmospheric Effects on the Propagation of MMW and Sub-MMW Radiation

A thesis submitted in partial fulfillment
of the requirements for the degree of
Master of Science

by

John Scott Cetnar
B.S. in Engineering, Wright State University, 1989
M.B.A., Wright State University, 1998

2010
Wright State University

Wright State University
SCHOOL OF GRADUATE STUDIES

June 16, 2010

I HEREBY RECOMMEND THAT THE THESIS PREPARED UNDER MY SUPERVISION BY John Scott Cetnar ENTITLED Atmospheric Effects on the Propagation of MMW and Sub-MMW Radiation BE ACCEPTED IN PARTIAL FULFILLMENT OF THE REQUIREMENTS FOR THE DEGREE OF Master of Science.

Douglas Petkie, Ph.D.
Thesis Advisor

Lok C. Lew Yan Voon, Ph.D.
Department Chair

Committee on Final Examination

Douglas Petkie, Ph.D.

Gregory Kozlowski, Ph.D.

Jerry Clark, Ph.D.

Jason Deibel, Ph.D.

John A. Bantle, Ph.D.
Vice President for Research and Graduate Studies
and Interim Dean of Graduate Studies

ABSTRACT

Cetnar, John. M.S., Department of Physics, Wright State University, 2010. *Atmospheric Effects on the Propagation of MMW and Sub-MMW Radiation.*

This thesis is a study of the propagation of millimeter wavelength (MMW) and sub-millimeter wavelength (sub-MMW) electromagnetic radiation (a.k.a. THz radiation) through the Earth's atmosphere. THz radiation is electromagnetic radiation that exists between the microwave and far infrared regions of the electromagnetic spectrum. It is nonionizing radiation but can penetrate through materials that are opaque to visible light so therefore has many new and useful applications. Unfortunately, THz radiation is heavily attenuated by the Earth's atmosphere as it propagates through it. This therefore represents a challenge to communications and sensing applications at millimeter and sub-millimeter wavelengths. In this work, the general theory of how the atmosphere attenuates propagating THz radiation by absorption and scattering is discussed. From this discussion, we find that water vapor is the constituent of the Earth's atmosphere most responsible for the absorption of THz radiation.

The absorption of THz radiation by water vapor was measured at 325 and 620 GHz using steady state or frequency domain absorption spectroscopy. The absorption lines of these frequencies lie in the far wings of a very strong water absorption line at 557 GHz. Spectral line shapes were recorded across a range of pressures and fitted to Voigt profiles. The resulting relationship between the line width and pressure was shown to be linear and very close to published values. Finally, transient signals associated with population and polarization relaxation times were measured at 325 GHz using transient or time domain spectroscopy techniques. Experimental results associated with the steady state and transient measurements will be presented and discussed.

Constants

c	299,792,458 m/s	Speed of light in vacuum
h	6.626 x 10^{-34} J·s	Planck Constant
$\hbar$	$\frac{h}{2\pi}$ = 1.055 x 10^{-34} J·s	Reduced Planck Constant
k	1.381 x 10^{-23} J/K	Boltzmann Constant
R	8.314 J/moles·K	Universal Gas Constant
N_0	6.022 x 10^{23} mol^{-1}	Avogadro's number

Contents

List of Figures

List of Tables

Acknowledgement

I would like to extend my thanks to the following.

To my advisor, Dr. Douglas Petkie for all the guidance you gave to me and the copious amount of ideas you always seemed to have. You have shown me many spectroscopic techniques that were not only effective but fun and interesting. I really appreciate your help.

To my thesis committee: Dr. Jerry Clark, Dr. Jason Deibel, and Dr. Gregory Kozlowski for your inputs and advice.

To the Father, the Son, and the Holy Spirit for giving me the wisdom, the courage, and the strength to do this work.

Dedicated to

My wonderful wife Robyn and three children: Sarah, Luke, and Daniel. Thank you for putting up with my ”hiding”away on nights and weekends to do physics.

Introduction

Millimeter wave and submillimeter wave (MMW and sub-MMW) radiation, also called terahertz (THz) radiation occupies a region of the electromagnetic spectrum between microwaves and far infrared. For this work, we define THz radiation in the frequency band starting at 100 GHz and going up to 1000 GHz or 3 mm to 0.3 mm wavelengths. This region is part of a broader area of the spectrum known as the THz gap. A diagram of the entire electromagnetic spectrum is shown in Fig. 1.1. Also shown are some well known objects of various sizes for reference so that one can get a feel of the relative sizes of the wavelengths.

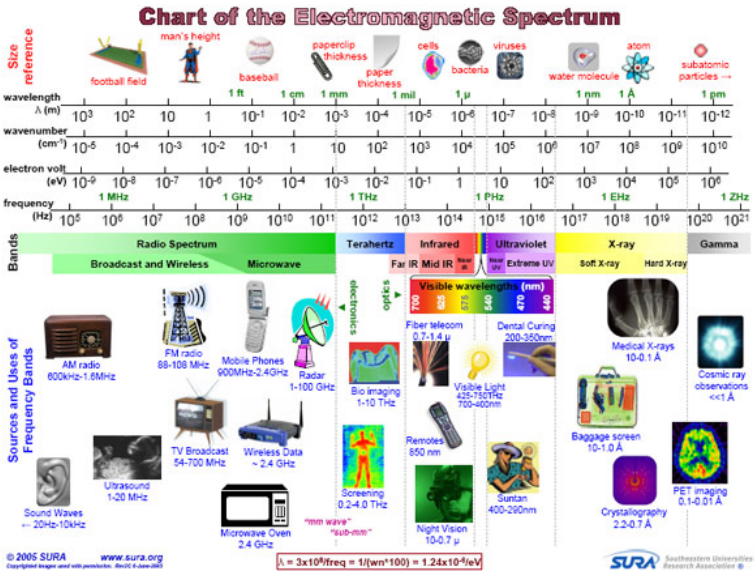

Figure 1.1: The electromagnetic spectrum as measured in wavelength (m), wavenumber (cm^{-1}), energy (eV), and frequency (Hz). Note: 300 GHz = 1 mm = 10 cm^{-1} $\approx$ 1.24 meV. From SUMA (Southeastern Universities Research Association) - www.suma.org

The THz region has many interesting properties from both purely scientific as well as applications standpoints. From the scientific standpoint, it is not an area of the electromagnetic spectrum that has been explored or exploited to the degree that other parts of the spectrum have. It is only within the last decade that advances in photonics and electronics have made THz sources more widely available [12]. Therefore, one could say that THz science is in many respects unplowed ground. From the applications side, new technologies are emerging from both ends of the THz gap. Microwave and radar technologies are trending toward shorter wavelengths with the hope of achieving better resolutions for imaging [13]. Optical and infrared technologies are trending towards longer wavelengths. The main reason behind this is that THz radiation has better transmission properties through most dielectrics than optical or IR radiation [14]. In addition, THz radiation is non-ionizing. These are very desirable attributes for applications such as the detection of objects concealed by dielectric mediums that are opaque to optical and IR radiation, for instance clothing or packaging. Furthermore, THz radiation can penetrate dust, light rain, and fog and therefore is superior to optical and IR radiation in navigation applications under these conditions [15]. All in all, the THz regime is gaining in importance and interest.

THz radiation has some of the best properties of both microwave and optical/IR wavelengths and is therefore a very appealing region of the electromagnetic spectrum to learn more about and to eventually use. Many workers in the spectroscopy field are now building instrumentation to take measurements in the THz region [16] [17]. New sources of THz radiation are being built and new types of detectors and detection methods are being developed. Many new applications are developing from the hardware and methodologies. Some of these applications include THz imaging systems for security [18], THz radar systems that detect displacement and velocity [19], THz profilometry sensors for characterizing surfaces [20], THz interferometers for measuring displacements [21], THz spectrometers for non-destructive materials evaluation [22], and many other devices and techniques too numerous to fully enumerate in this work. Most of these techniques would come under

the broad category of remote sensing, since THz radiation is being used to detect physical phenomena at some distance without contact.

There is however a trade off for using THz radiation for remote sensing. The transmission characteristics of MMW radiation are highly affected by the Earth's atmosphere. Fig. 1.2 shows the attenuation of electromagnetic radiation in the atmosphere as a function of frequency from microwave (30 cm) through ultraviolet (300 nm) as calculated by the LEEDR (Laser Environmental Effects Definition and Reference) atmospheric propagation modeling software developed at the Air Force Institute of Technology's Center for Directed Energy (AFIT/CDE) at Wright Patterson Air Force Base, Dayton, Ohio [1].

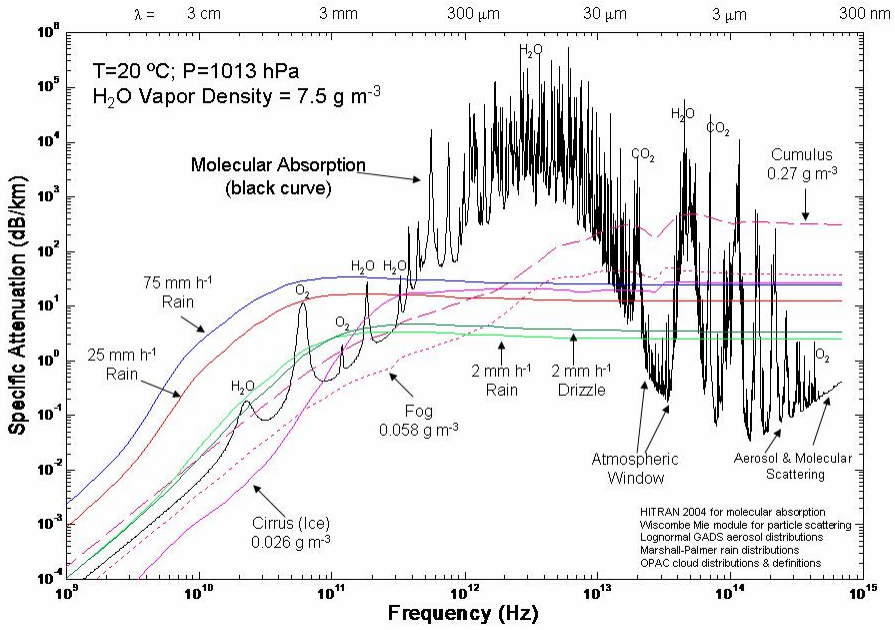

Figure 1.2: Atmospheric attenuation of electromagnetic radiation across the MMW region. From Fiorino et al. [1].

The black curve in the figure shows atmospheric attenuation at a given temperature, pressure, and humidity. This curve is considered the attenuation in dry atmosphere (no precipitation). The solid colored curve shows the effect due to rain. The dashed colored curves show the effects due to fog and clouds. As one can see, attenuation in the dry atmosphere for the 3 mm to 300 μm region is marked by several resonant peaks of high attenuation

and windows of lower attenuation between the peaks. Wavelengths in the windows are what are typically used for transmission in this region. The minimum attenuation in the windows is the result of the far wings of the peak line shapes and an underlying floor, or continuum. Note that attenuation due to the continuum increases with frequency starting in the microwave region and eventually exceeds the attenuation from heavy rain at a wavelength of 1 mm. The continuum peaks well into the far infrared region, then falls through the infrared until reaching a minimum in the visible region. Past the visible region, continuum attenuation increases again in the ultraviolet. The effect of rain, fog, cloud cover, and other hydrometeors is to raise the continuum at wavelengths below 1 mm and in the visible region. The primary fact to note from these calculations for this work is that atmospheric attenuation of THz radiation is strong and extremely variable!

There are three major causes of attenuation in the atmosphere: absorption, scattering, and scintillation. Absorption of radiation in the THz range is caused by certain atmospheric gases, most notably water vapor (H_2O) and molecular oxygen (O_2) as shown in Fig. 1.2. At millimeter and sub-millimeter wavelengths, electromagnetic energy absorbed by these molecules excites transitions to higher quantized rotational states. Absorption decreases the energy of the propagating signal, particularly at the absorption lines but also to a varying degree between the absorption lines. Scattering is caused primarily by hydrometeors: rain drops, sleet, snow flakes, ice particles, fog droplets, and clouds. These are basically objects made of water that are falling to Earth as precipitation or suspended in the atmosphere. In addition, there can be significant scattering from particulates and aerosols: dust, smoke, sand et. Scattering by objects which are much smaller than the wavelength of the incident radiation fall into the Rayleigh scattering regime. In this regime the scattering intensity is approximately proportional to the size of the scatterer. Scattering by objects which are roughly the same size as the wavelength of the incident radiation fall in the Mia scattering regime. This regime is also called the resonant scattering regime. In this regime, the scattering intensity varies strongly with frequency and the orientation of the scatterer to

the incident radiation. Scattering by objects which are much larger than the wavelength of the incident radiation fall into the optical scattering regime. In this regime, scattering is governed by geometric optics as the wave nature of the EM radiation is not significant.

The third source of attenuation in the atmosphere is scintillation. Scintillation occurs when EM radiation propagates through small pockets of air that are at higher or lower relative humidities than the rest of the propagation path. These pockets of varying humidity are mixed throughout the lower atmosphere by turbulence and generally cause the index of refraction of the air along the propagation path to vary with time and space. As the propagating radiation encounters one of these pockets, it is bent as though by a lens. Depending on the size of the pocket, some of the propagating wavefront is refracted while some is not. This results in phase noise and distortions in the received signal. Scintillation can seriously interfere with communications and remote sensing applications. Broad absorption resonances coupled with system standing wave and scintillation effects can make it very difficult to do terrestrial gas phase sensing at atmospheric pressure. These effects can cause ”clutter” or noise in the time domain that also obscures the signals of interest. It is interesting to note that sensing in the upper atmosphere (i.e the stratosphere) and the interstellar medium is highly successful, while terrestrial sensing at atmospheric pressures is more problematic.

However, there is an alternative way of looking at atmospheric attenuation, particularly attenuation by water vapor. Absorption events can generate transient signatures. These signatures are worth studying because they may: 1) provide an alternative method for gas phase sensing, 2) mitigate system and atmospheric problems, or 3) pop back up as a problem if some type of complex frequency modulation or shifting is employed at a GHz rate and the transients are now noise. This is the motivation for this study.

This study will explore these types of phenomena as they relate to the terrestrial propagation of THz radiation. This thesis is organized to reflect the chronology of efforts and events that made this study. It is divided into five chapters including this introduction. The

second chapter will discuss the theory behind atmospheric attenuation of THz radiation and microwave molecular spectroscopy. It covers THz absorption and scattering in some detail with an emphasis on absorption. The third chapter covers the details of the steady state spectroscopy measurements made on water vapor. Experimental measurements of the absorption of THz radiation by H_2O at 620 GHz and 325 GHz were made and analyzed. The fourth chapter covers the details of the transient spectroscopy measurements made on water vapor. Measurements were attempted on the H_2O line at 620 GHz but were unsuccessful. These failed attempts are dicussed. The frequency switching and rotary echo methods were tried. Measurements were made on the transient response of H_2O at 325 GHz using the fast sweep technique. These measurements were then analyzed. The fifth and final part of this work will summarize and discuss the theory, these experiments and their results.

The Theory of Atmospheric Attenuation

2.1 The Structure of the Atmosphere

In this work, when we refer to the atmosphere, we are referring to the neutral atmosphere. The neutral atmosphere is defined as that part of the Earth's atmosphere in which the population of ionized particles (molecular ions, atomic ions and free electrons) is negligible compared to the population of neutral molecules and atoms. Negligible means an extremely low fraction compared to what might be found in the ionosphere. The boundary between the neutral atmosphere and ionosphere is nominally found at an altitude of about 80 km. However, this is highly dependent on solar activity. The boundary can sometimes drop to as low as 50 km and rise to as high as 90 km [23].

The atmosphere is a mixture of gases. According to Meeks, Astrophysics - Part B: Radio Telescopes, Vol. 12, Methods of Experimental Physics, the principle constituents of the atmosphere by volume below altitudes of 80 km are: nitrogen (78.09%), oxygen (20.95%), argon (0.93%), and carbon dioxide (0.03%). Other trace gases account for less than 0.0003%. These include (in decending order by volume): neon, helium, methane, krypton, hydrogen, nitrous oxide, carbon monoxide, xenon, ozone, ammonia, sulphur dioxide, hydrogen sulfide, formaldehyde, nitrogen dioxide, chlorine, and iodine [3]. Of the four most common gases, only oxygen has any significant interaction with THz radiation. Water vapor, though not included in the list above is a very important constituent of the atmosphere because of its stong interaction with THz radiation. In addition, the concentra-

tion of water vapor present in the atmosphere, particularly from locale to locale, is highly variable. Below 80 km, the relative concentrations of the atmospheric gases, except for water vapor, is fairly constant. This is due to turbulent mixing by winds. Above 80 km, diffusion mechanisms start to dominate and the relative concentrations of the these gases changes significantly [3].

The amplitude, phase, and direction of propagating THz radiation can be modified due to interactions with atmospheric gases, condensed water vapor, clouds, and precipitation. The strength of these interactions are functions of temperature, pressure, and relative humidity. [3]. The general behavior of atmospheric temperature and pressure with respect to altitude is shown in Fig. 2.1 [2].

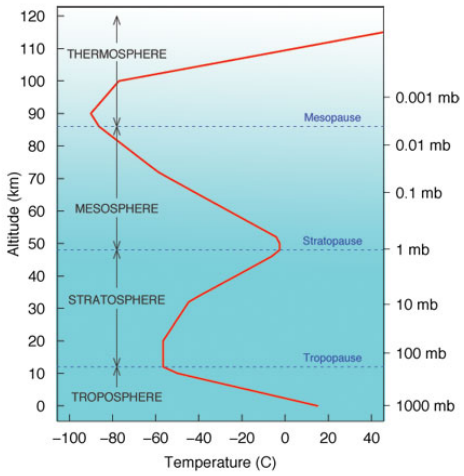

Figure 2.1: Atmospheric pressure decreases exponentially as altitude increases, while temperature rises with altitude in some layers and decreases in others. From Wofsy [2].

The atmosphere is divided into three regions or layers in which the temperature changes with altitude. The layers are: the troposphere, the stratosphere, and the mesosphere. The three regions are separated by two boundary regions where the temperature remains constant. These boundaries are called the tropopause and the stratopause. The troposphere is the layer in contact with the Earth's surface. The troposphere is the atmospheric layer in which we live and for that matter all terrestrial life on Earth exists. It is also the only layer

of the atmosphere that experiences any type of significant weather. The troposphere is characterized by temperatures that tend to decrease with increasing altitude until the tropopause is reached. Within the tropopause, the temperature is constant with altitude. At the top of the tropopause begins the stratosphere. The stratosphere is characterized by relatively calm conditions compared to the troposphere. That is why most commercial airline flights try to fly in the stratosphere. The stratosphere is also characterized by temperatures that rise with altitude. At the top of the stratosphere is another layer of constant temperature called the stratopause. The stratopause then gives way to the highest layer in the neutral atmosphere, the mesosphere. The mesosphere is characterized by temperatures that decrease with altitude.

In general, atmospheric pressure tends to decrease with altitude exponentially [3]. At the surface, atmospheric pressure will vary, sometimes significantly, from air mass to air mass. However, within the same air mass, temperature and pressure vary only small amounts [3]. The variation of atmospheric pressure across air mass boundaries, also known as fronts, is what drives winds on Earth's surface. Large scale changes in atmospheric pressure mainly affect the troposphere.

Relative humidity (RH) is a measure of the concentration of water vapor in the air compared to dry air. It is highly variable, particularly within 1 to 2 km of the Earth's surface [3]. Fig. 2.2 shows the average moisture profile with respect to altitude for a mid-latitude site in the U.S. [3].

As can be seen, RH decreases with increasing altitude from the surface through the troposphere. RH is fairly constant in the tropopause. In the stratosphere, RH increases with altitude up to around 25 km. It then decreases with altitude up to 70 km. As with pressure, RH can vary significantly from air mass to air mass across fronts.

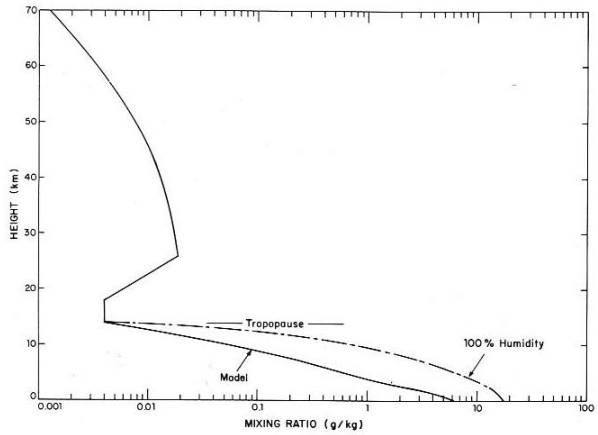

Figure 2.2: Altitude versus moisture content in the neutral atmosphere. From Meeks [3].

2.2 Absorption

2.2.1 Radiative Transfer at THz Wavelengths

The equation of radiative transfer was initially developed and published by S. Chandrasekhar in 1960. This equation gives the mathematical description of how the intensity of electromagnetic radiation is affected as it propagates through a medium. For a nonscattering, nonrefractive atmosphere in thermal equilibrium, which holds for Earth's atmosphere at MMW/sub-MMW wavelengths, the radiative transfer equation is given by [3]

$$I_\nu(s) = I_\nu(0)e^{[-\tau_\nu(0,s)]} + \int_0^s B_\nu(T)e^{[-\tau_\nu(s',s)]}k_\nu(s')ds' \tag{2.1}$$

where I_ν(s) is the intensity of the radiation of frequency ν at position s, $I_\nu(0)$ is the initial intensity, $B_\nu(T)$ is the Planck function giving the intensity of radiation at frequency ν from a black body of temperature T, τ_ν is the optical depth from some position (0 or s') to a second position (s), and k_ν(s') is the absorption coefficient at frequency ν and position s. The optical depth is given by

$$\tau_\nu(s', s) = \int_{s'}^s k_\nu(s'')ds'' \tag{2.2}$$

where s and s' are the limits of the integration path, which is the path of propagation and observation, and s'' is the integration variable. As radiation propagates through the atmosphere, it will encounter the molecules and atoms that make up the medium along its path. The medium will absorb and then re-radiate, or emit, some of the energy from the incident radiation into other directions, effectively removing it from the incident beam. The photons lost due to this absorption/emission process are replaced by what the medium is naturally emitting in the direction of incidence in the form of black body radiation. However, the intensity of the incident radiation in our experiment is much higher than the intensity of the black body radiation. Therefore we can set $B_\nu(T)$, the black body radiation term, to zero along the path and only the first term in Eq. 2.1 need be considered. In this case, the intensity of the radiation at any point s along the path of observation is a function of the initial intensity and the optical depth. If the volume absorption coefficient, $k_\nu(s')$ is constant along the path of observation, independent of s but still dependent on frequency ν, it is usually written as α_ν and the optical depth is then expressed as

$$\tau_\nu = \alpha_\nu L \tag{2.3}$$

where L is the length of the integration path from s to s'. Let us write the intensity as I, dependent on frequency but without the ν subscript, and the initial intensity as I_0. Under all of these conditions, we can write the radiative transfer equation as

$$I = I_0 e^{-\alpha_\nu L} \tag{2.4}$$

From this form, if we define the ratio of I to I_0 as T, the transmissivity, we end up with the famous Beer-Lambert Law

$$T = \frac{I}{I_0} = e^{-\alpha_\nu L} \tag{2.5}$$

2.2.2 Absorption Theory

As THz radiation propagates through Earth's atmosphere, its energy is absorbed and therefore its power attenuated. THz radiation is absorbed by molecules that make up the Earth's atmosphere. Atmospheric absorption in the THz range is dominated by water vapor, H_2O, and molecular oxygen, O_2, as stated earlier. Two types of absorption exist. There is resonant absorption, which occurs on or very close to the resonant absorption lines of these molecules. There is also nonresonant absorption. This occurs farther away from the absorption lines in the windows between the resonant frequencies. Both resonant and nonresonant absorption have significant affects on THz propagation in the atmosphere.

Fig. 2.3 shows a the region of the EM spectrum from RF to UV. It also shows the physics behind how EM radiation interacts with atoms and molecules in those regions.

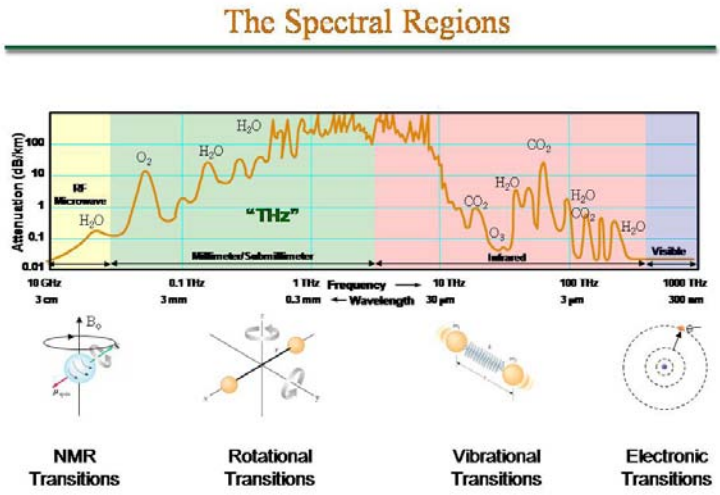

Figure 2.3: EM spectrum from RF to UV and the mechanisms of EM radiation interaction with atoms and molecules.

At THz frequencies, radiation is absorbed and emitted by gas molecules due to changes in rotational state. In order for its rotational state to be affected by electromagnetic radiation, a gas molecule must have a dipole moment and its center of charge must differ from its center of mass. If a molecule has an electric or magnetic dipole moment, the electric or

magnetic field of the EM wave will exert a torque on the molecule and cause it to either increase or decrease its rotational velocity. In solids and in liquids, rotational motion is severely inhibited due to collisions, intermolecular forces, and bonding. The absorption and emission of THz radiation associated with changes of rotational state are primarily phenomena of the gas phase.

From quantum mechanics, it is known that the rotational energy and angular momentum of a gas molecule are quantized. This means that the rotational energy and angular momentum may only take on certain fixed values. These values are described by quantum rotational numbers. When a gas molecule encounters radiation at certain special frequencies, actually photons at certain energies, the gas molecule will absorb the photon and gain rotational energy and angular momentum. The molecule will be excited from one quantum rotational state to a higher quantum rotational state. As just stated, only photons with certain energies will cause these transitions. The energies of these photons must correspond to the energy differences in the quantum rotational states of the molecule. This idea can be expressed mathematically by the simple relation

$$E_\gamma = E' - E \tag{2.6}$$

where E_γ is the energy of the photon, E' is the energy of the higher (upper) state, and E is the energy of the lower state. Further, the energy of a photon can be expressed as the frequency and wavelength of the radiation. In this spirit we can write

$$h\nu = \frac{hc}{\lambda} = E' - E \tag{2.7}$$

where ν is the frequency of the radiation, λ is its wavelength, and h is the Planck constant.

As stated earlier, it is also possible for molecules to emit THz radiation. This occurs when a molecule transitions from a higher quantum rotational state to a lower one. The energy of the emitted photon, and therefore the frequency of the emitted radiation, is equal

to the energy difference between the two quantum rotational states. Rotational transition emissions can be spontaneous or stimulated.

It must also be said that the energy difference between quantum rotational states is small compared to vibrational or electronic quantum state transitions. Rotational state transitions correspond to the absorption and emission of photons with energies of less than 0.005 eV. For comparison, a typical electronic transition, in the optical range, is 2-4 eV. Therefore, the energies involved in rotational state transitions are three orders of magnitude smaller than those in electronic transitions.

For most gas molecules there are many quantum rotational states and therefore a rich spectrum of rotational transitions can be studied. This is the basis for microwave molecular spectroscopy, which is the study of the rotational spectra of gas phase molecules. From a signal transmission standpoint, this means that there are many frequencies between 100 GHz and 1 THz which will excite transitions that absorb the propagating radiation.

2.2.3 Molecular Rotation

As mentioned above, the rotational energy and angular momentum of a gas molecule are quantized, taking on only certain values. What those values are is determined by the molecule's moment of inertia, I. In general, I consists of three components, I_A, I_B, and I_C, known as the principle moments of inertia. Each component is the moment of inertia about one of three mutually orthogonal principle axes, with the origin at the center of mass of the molecule. From the relationships between I_A, I_B, and I_C, we can place a gas molecule into one of four classes. Table 2.1 below shows how a gas molecule is classified based upon relationships between its the principle moments.

Note, we model a molecule as a rigid body as a simplification. In truth, no molecule is actually a rigid body with the bond distances and angles between the constituent atoms fixed. Rotational inertias and deformations due to impact will cause bonds to shear, stretch

Linear molecule	$I_A \ll I_B = I_C$
Symmetric rotor	$I_A = I_B \neq I_C$
Spherical rotor	$I_A = I_B = I_C$
Asymmetric rotor	$I_A \neq I_B \neq I_C$

Table 2.1: Classification of gas molecules based upon moments of inertia

and compress. These added degrees of freedom lead to significant complications in the analysis of a molecule's dynamics and are not really germane at the level of this study. Therefore, in the following discussions, we will treat them as effectively rigid except where specified otherwise.

Linear molecules can be either diatomic or polyatomic. In linear molecules, if we set $I_A \sim 0$, then the rotational motion can be described as end over end somersaulting in the plane corresponding to the B and C principle axes. In linear molecules, bond lengths can be determined from line spectra [24]. The separation of the spectroscopic lines can be directly related to the moment of inertia. If the mass of the molecule is known, then the length of bond can easily be calculated from the measured the absorption frequency. For diatomic molecules this can be done with one measurement. For polyatomic molecules, it is not so easy. Polyatomic linear molecules are subject to non-rigid behaviors such as vibrational motion in the form of bending modes and/or $l\ doubling$. This will complicate the spectra and require additional measurements with different isotopes in order to calculate bond lengths. Some examples of linear molecules include molecular oxygen (O_2), carbon monoxide (CO), sodium chloride (NaCl), carbon dioxide (CO_2), nitrous oxide (N_2O), and carbonyl sulfide (OCS) [4].

The subsequent analyses of linear, symmetric rotor, and asymmetric rotor molecules follows that given in Townes and Schawlow [4]. A simplifying approximation is made that the distance between the nuclei in a diatomic molecule is constant. The molecule is then treated as a rigid rotor. In that case, its angular momentum is an integral multiple of $\hbar$ and

$$2\pi\nu I = \hbar J \tag{2.8}$$

where $\hbar$ is the reduced Planck constant such that $\hbar = \frac{h}{2\pi}$, I is the moment of inertia, ν is the frequency of rotation, and J is the total angular momentum quantum number, a positive integer (see Table 2.1). The expected rotational frequencies are then

$$\nu = \frac{\hbar J}{2\pi I} \tag{2.9}$$

A more rigorous determination comes from solving the Schrödinger equation with no potential energies. In spherical coordinates the Schrödinger equation is [4]

$$\frac{h^2}{8\pi^2 I}\left[\frac{1}{\sin\theta}\frac{\partial}{\partial\theta}(\sin\theta\frac{\partial\psi}{\partial\theta}) + \frac{1}{\sin^2\theta}\frac{\partial^2\psi}{\partial\phi^2}\right] + E\psi = 0 \tag{2.10}$$

where E is the energy. Solution to this equation are single-valued and normalized only when [4]

$$E = \frac{h^2}{8\pi^2 I}J(J+1) = \frac{\hbar^2}{2I}J(J+1) \tag{2.11}$$

with wave function solutions:

$$\Phi_M = \frac{1}{\sqrt{2\pi}}e^{iM\phi} \tag{2.12}$$

and

$$\Theta_{MJ} = \left[\frac{(2J+1)(J-|M|)!}{2(J+|M|)!}\right]^{1/2} P_J^{|M|}(\cos\theta) \tag{2.13}$$

where $P_J^{|M|}(\cos\theta)$ is the associated Legendre polynomial and M is the magnetic quantum number. The magnetic quantum number is the projection of the angular momentum along a fixed space axis, normally the polar or z axis. M is an integer such that $|M| \leq J$ (see Table 2.2).

Thus we have the eigenvalues (energy levels) and the eigenvectors (wavefunctions)

of the quantized rigid rotor that represents a diatomic molecule such as O_2. Further, the coefficient term at the beginning of equations 3.10 and 3.11 is often written as [4]

$$B = \frac{h}{8\pi^2 I} \tag{2.14}$$

where B is in MHz and is known as a constant of rotation along the B principle axis. For O_2, B = 43,100 MHz [3]. We can substitute B into the equation for the energy of the rigid rotor to get

$$E = BJ(J+1) \tag{2.15}$$

The selection rule for dipole radiation of a diatomic molecule is given by

$$\Delta J = \pm 1 \tag{2.16}$$

so that only transitions for which J increases by one or decreases by one are allowed.

Molecular oxygen is very plentiful in the atmosphere and it has absorption lines in the MMW and sub-MMW regions. It is a diatomic molecule, but has no electric dipole moment. Therefore, none of its spectral lines are due to electric dipole transitions. However, molecular oxygen does have a permanent magnetic dipole moment due to the combined spins of two unpaired electrons. Its spectral lines in the microwave and THz regions are due to this magnetic dipole moment. The online Jet Propulsion Laboratory Molecular Spectroscopy Catalog lists data on all the known spectral lines of molecular oxygen [25]. A search of the catalog for spectral lines between 100 - 1000 GHz yields seven resonant transition frequencies. The line intensities of these seven are relatively weak compared to the absorption line intensities of other species. This is due to the fact that in general, for a given EM field strength, magnetic dipole interactions are much weaker than electric dipole interactions. However, since O_2 is so plentiful in the atmosphere it is still a significant at-

tenuator of MMW and sub-MMW radiation. Two well known spectral lines for molecular oxygen exist at 60 GHz, and at 118 GHz. These lines are due to changes in the relative orientation of the electronic spin and the axis of rotation of the molecule [3]. Lines at 368 GHz and above are due to transitions between rotational states.

Symmetric rotor molecules are those molecules for whcih two of the three moments of inertia are the same. Two types of symmetric rotor molecules are recognized: oblate and prolate. Oblate symmetric rotors tend to flatten out around the middle resulting in a disc shape. For these molecules $I_A = I_B < I_C$. Prolate symmetric rotors flatten out along the axis of rotation resulting in a football shape. For these molecules $I_A < I_B = I_C$. Some examples of symmetric rotor molecules include ammonia (NH_3), methyl chloride (CH_3Cl), and methyl fluoride [4].

Although we will not be focusing in detail on any symmetric top molecules in this study, it is still worthwhile to analyze the symmetric rotor. First, analytical solutions exist for the symmetric rotor while they do not exist for the asymmetric rotor. Second, the solutions for the symmetric rotor provide a basis in terms of which the wave functions of any molecule (i.e. asymmetric rotors) can be expanded. The energy levels and selection rules for the symmetric rotor can be determined from classical mechanics and the correspondence principle. Fig. 2.4 represents methyl chloride [4].

As can be seen in the figure, the motion of the symmetric rotor molecule is the same as a classical symmetric top. The motion is a combination of rotation around the molecular axis associated with L_z and precession around the axis coincident with the total classical angular momentum L. The precession frequency is given by

$$\nu_p = \frac{L}{2\pi I_B} \tag{2.17}$$

The energy of rotation is given by

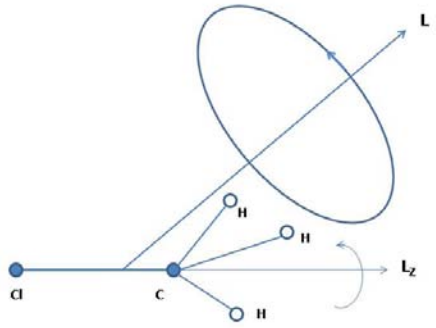

Figure 2.4: Motion of a symmetric top rotor. From Townes and Schawlow [4]

$$E = \frac{1}{2}I_x\omega_x^2 + \frac{1}{2}I_y\omega_y^2 + \frac{1}{2}I_z\omega_z^2 = \frac{L_x^2}{2I_x} + \frac{L_y^2}{2I_y} + \frac{L_z^2}{2I_z} \tag{2.18}$$

where x, y, and z coincide with the principle axes A, B, and C respectively.

Since two of the three moments of inertia are equal, let $I_x = I_y = I_B$ and let $I_z = I_C$. Also note that

$$L^2 = L_x^2 + L_y^2 + L_z^2 \tag{2.19}$$

We can substitute back into Eq. 2.18 to get

$$E = \frac{L^2}{2I_B} + L_z^2\left(\frac{1}{2I_C} - \frac{1}{2I_B}\right) \tag{2.20}$$

We quantize L^2 to $J(J+1)\hbar^2$ and L_z^2 to $K^2\hbar^2$, both J and K integers. Eq. 2.20 then becomes

$$E = \frac{J(J+1)\hbar^2}{2I_b} + \left(\frac{\hbar^2}{2I_C} - \frac{\hbar^2}{2I_B}\right) \tag{2.21}$$

Typically, rotational constants are defined for each principle axes [4]

$$A = \frac{h}{8\pi^2 I_A} \tag{2.22}$$

$$B = \frac{h}{8\pi^2 I_B} \tag{2.23}$$

$$C = \frac{h}{8\pi^2 I_C} \tag{2.24}$$

Finally, using these constants the rotational energy can be expressed as [4]

$$E = h[BJ(J+1) + (C-B)K^2] \tag{2.25}$$

This expression, Eq. 2.25, gives the allowable energy levels for a symmetric rotor. The variable K is given by [4]

$$K = J, J-1, J-2, ..., -J \tag{2.26}$$

Therefore, for a given angular momentum, J, multiple values of K are allowed. Generally, K is the projection of J along the axis of symmetry in a body fixed coordinate system as seen in Table 2.2. For each J, there are $2J+1$ possible K values. These represent degeneracies in energy.

Symmetric rotors can be classified as either oblate or prolate. For the prolate rotor, the football shape, the moment of inertia about the symmetry axis is less than that about the other principle axes, $I_z < I_B$. In equation 2.25, the coefficient of K^2 is positive, $C > B$. Therefore, for a given J energy increases with increasing K. In other words, the less a prolate top wobbles, the more rotational energy it has. For the oblate symmetric rotor, the disc shape, the moment of inertia about the symmetry axis is greater than that about the

other principle axes, $I_z > I_B$. In Eq. 2.25, the coefficient of K^2 is negative, $B > C$. Therefore, for a given J energy increases with decreasing K. In other words, the more an oblate top wobbles, the more rotational energy is has.

Symmetry demands that there can be no dipole moments perpendicular to the axis of symmetry in a symmetric top rotor. Therefore, incident radiation will not cause any torques along an axis perpendicular to the symmetry axis. This implies that K does not change due to incident radiation [4]

$$\Delta K = 0 \tag{2.27}$$

Any dipole moments must be coincident with the symmetry axis which itself precesses around the total angular momentum axis. The selection rule for symmetric top transitions is given by [4]

$$\Delta J = \pm 1 \tag{2.28}$$

Because of these selection rules, the observed transition frequencies of the symmetric top are independent of K or the moment of inertia about the symmetry axis, I_C, at least if we model the symmetric top as rigid. The observed frequencies are given by [4]

$$\nu = \frac{2h(J+1)}{8\pi^2 I_B} = 2B(J+1) \tag{2.29}$$

Table 2.2 below summarizes the quantum number used in the linear molecular and symmetric rotor analyses. Note that quantum numbers M and K are very similar. Both are projections of the total angular momentum and have the same value range relative to the total angular momentum. The difference being M is along a space fixed axis while K is along the symmetry axis which is a body fixed axis.

Spherical rotor molecules are molecules in which the moments of inertia are all equal,

N	Principle quantum number	$N > 0$
J	Total angular momentum	$J < N$
M	Projection of angular momentum along a space fixed axis	$\|M\| \leq J$
K	Projection of angular momentum along an axis of symmetry, body fixed axis	$\|K\| \leq J$

Table 2.2: Quantum numbers used with quantum rotors.

$I_z = I_B$. In Eq. 2.25, the coefficient of K^2 is zero, $C = B$. Therefore, all rotational energy is a function of the total angular momentum J only. Some examples of spherical top molecules are carbon tetrachloride (CCl_4), ammonium ion (NH_4^+), and sulfur hexafluoride (SF_6) [4].

Asymmetric rotor molecules are molecules in which none of the principle moments are equal. Most large molecules are asymmetric tops; some examples include water (H_2O) and nitrogen dioxide (NO_2) [4]. No simple interpretation of the spectra of an asymmetric top molecule will lead to the determination of molecular structure. Educated guesses are made based upon symmetry and substitution of isotopes during a series of measurements. In this work, water vapor is of prime concern due to its abundance in the atmosphere and the strength of its absorption line intensities.

Analysis of asymmetric rotors generally follows along the same line as analysis of symmetric rotors. However, it is much more complicated. In fact, these complications hold in both the classical and quantum regimes.

Asymmetric tops can be thought of as tops that have deviated from the two symmetric top extremes, prolate and oblate. Asymmetric tops exist between these two extremes and the general approach to analyzing them is to examine their behavior near these extremes.

The rotational energy of an asymmetric top is given by [4]

$$E = \frac{L_x^2}{2I_x} + \frac{L_y^2}{2I_y} + \frac{L_z^2}{2I_z} = \frac{2\pi A}{\hbar}L_x^2 + \frac{2\pi B}{\hbar}L_y^2 + \frac{2\pi C}{\hbar}L_z^2 \tag{2.30}$$

In this case $A \neq B \neq C$ and in fact it is customary to let $A > B > C$. For the prolate symmetric top $B = C$. For the oblate symmetric top $B = A$. The range of values that B

takes is between A and C and corresponds to the degree of symmetry the top exhibits. If B varies only a slight amount from C or A it is referred to as a slightly asymmetric top.

The degree of asymmetric is indicated by Ray's asymmetry parameter [4]

$$\kappa = \frac{2B - A - C}{A - C} \tag{2.31}$$

For prolate symmetric tops $\kappa = -1$. For oblate symmetric tops $\kappa = 1$. For asymmetric tops $-1 < \kappa < 1$. Ray's parameter is a measure of the asymmetry of the rotor with κ = 0 being the most asymmetrical. Two additional parameters that are used in slightly asymmetric tops are [4]

$$b_p = \frac{\kappa + 1}{\kappa - 3} \tag{2.32}$$

for asymmetric prolate tops and

$$b_o = \frac{\kappa - 1}{\kappa + 3} \tag{2.33}$$

for asymmetric oblate tops. Parameter b_p starts at 0 for a prolate symmetric top and decreases in value as the top becomes more asymmetric. Likewise, parameter b_o starts at 0 for an oblate symmetric top and decreases in value as the top becomes more asymmetric.

For symmetric tops, the total angular momentum J, and its projection along a body fixed axis K, are constants of motion and therefore are good quantum numbers. This means they can be used to specify the rotational state of the top. However, there is no axis of symmetry in an asymmetric rotor nor is the component of the angular momentum along any arbitrary direction in the asymmetric rotor constant. Therefore, K is not a good quantum number and cannot be used to specify the rotational state of the top. In fact, no set of convenient quantum numbers exists that can specify the rotational state and provide any good intuitive physical meaning. Furthermore, the energy levels of the asymmetric rotor differ

from those of the symmetric rotor. For the asymmetric rotor the energy levels corresponding to $-K$ and $+K$, which are always degenerate in the symmetric rotor, are split. Where as the symmetric rotor has $(J+1)$ energy levels for each value of J, the asymmetric rotor has $(2J+1)$ distinct energy levels for each J. The splitting of the these K energy levels increases with increasing asymmetry until there is no longer any correspondence between two levels of the asymmetric rotor and the two degenerate levels of the symmetric rotor. Nevertheless, energy levels of asymmetric rotors are specified with J, and a modified version of K. K becomes K_{-1}, the value for the limiting prolate, and K_1, the value for the limiting oblate.

Fig. 2.5 [5] shows the convention. The notation is known as the King-Haier-Cross notation, and is written $J_{K_{-1}K_1}$ [5]. The subscripts -1 and 1 are the limiting values of the asymmetry parameter κ. By connecting the K levels for a given J of the limiting prolate symmetric rotor with those of the limiting oblate symmetric rotor, in an ordered sequence going from highest to highest, next highest to next highest and so on, one may at least gain a qualitative feel for the energy levels of an asymmetry rotor. Note from Fig. 2.5 that there is no crossing of energy sublevels for a given J although those of different J may cross. Also, the straight line representation of the variation of energy levels with K is only approximate.

As an example of this notation, consider the 325 GHz absorption transition of water vapor. We will be studying this line in more detail later in this thesis. This transition can be written as $5_{1,5} \leftarrow 4_{2,2}$. This indicates a transition from state $4_{2,2}$ to state $5_{1,5}$. The state $4_{2,2}$ means $J = 4$, and an energy level which in the limiting case connects $K = 2$ on the left hand side of the figure to $K = 2$ on the right hand side of the figure. Likewise the state $5_{1,5}$ means $J = 5$, and a level which in the limiting case connects $K = 1$ on the left hand side of the figure to $K = 5$ on the right hand side of the figure. The fact that 5 is greater than 4 means that $J \rightarrow J + 1$. Angular momentum and rotation energy increase as would be expected from the absorption of radiation.

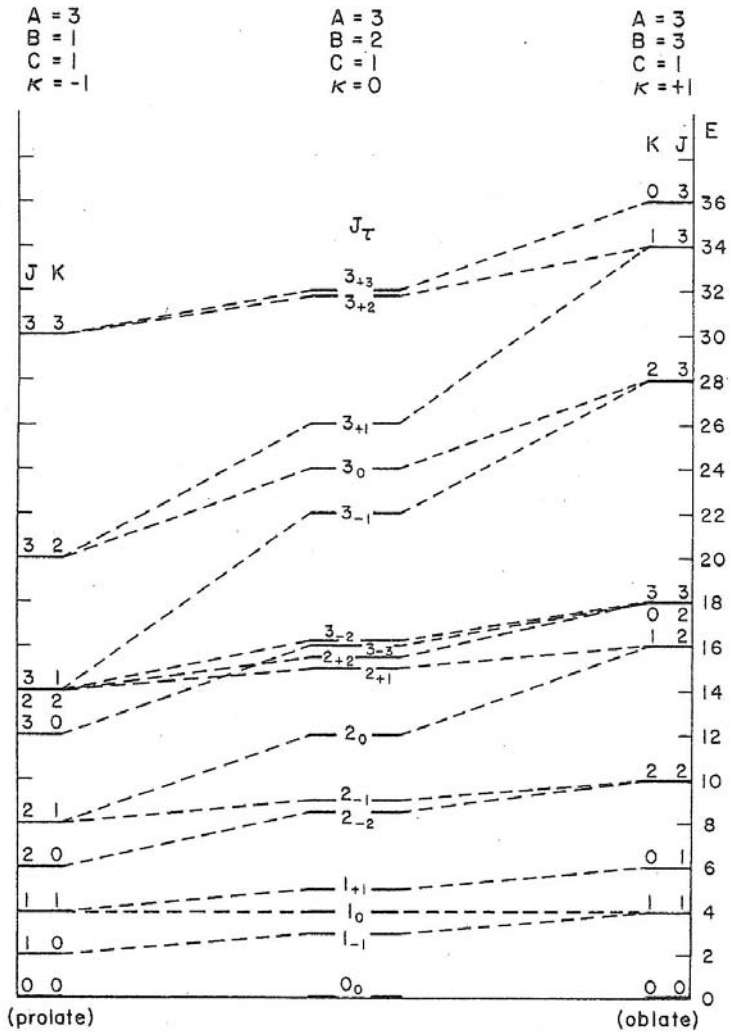

Figure 2.5: Relation of the asymmetric rotor energy levels to those of the limiting prolate and oblate symmetric rotor. From Gordy and Cook [5].

For a slightly asymmetric prolate top, the energy may be written as [4]

$$E = h\left[\frac{B+C}{2}J(J+1) + \left(A - \frac{B+C}{2}\right)E_p\right] \tag{2.34}$$

where

$$E_p = K^2 + c_1 b_p + c_2 b_p^2 + c_3 b_p^3 + ... \tag{2.35}$$

where b_p is the asymmetry parameter for a prolate top given in Eq. 2.32 and the coefficients $c_1, c_2, c_3, ...$ can be retrieved from sources such as Townes & Schawlow [4].

For a slightly asymmetric oblate top, the energy may be written as [4]

$$E = h\left[\frac{A+B}{2}J(J+1) + \left(C - \frac{A+B}{2}\right)E_o\right] \tag{2.36}$$

where

$$E_o = K^2 + c_1 b_o + c_2 b_o^2 + c_3 b_o^3 + ... \tag{2.37}$$

where b_o is the asymmetry parameter for a oblate top given in Eq. 2.33 and the coefficients $c_1, c_2, c_3, ...$ (not the same coefficients as for the prolate case) can be retrieved from sources such as Townes & Schawlow [4].

For the case where the molecule is very asymmetric, $\kappa \simeq 0$, then the asymmetry parameter b is large, and expansions such as Eq. 2.35 and Eq. 2.37 are not appropriate. In that case, energy is expressed as [4]

$$E = \frac{h}{2}[(A+C)J(J+1) + (A-C)E_{K_{-1}K_{+1}}] \tag{2.38}$$

where $E_{K_{-1}K_{+1}}$ replaces E_p and E_o in Eq. 2.34 and Eq. 2.36. $E_{K_{-1}K_{+1}}$ is a complicated function dependent on the amount of asymmetry via the Ray symmetry parameter κ. It

has been computed and tabulated and can be found in various tables and appendices (see Townes & Schawlow Table 4-1 [4]).

The selection rules for asymmetric rotors are very complicated. There are primarily three causes of the complication. First, asymmetric rotors have many more energy levels than any of the other three classes of molecules. Second, the dipole moment in an asymmetric rotor can lie in any arbitrary position with respect to a principle axis. Third, symmetry and parity requirements must be followed if a transition is to be allowed. The selection rule for changes in J for the asymmetric rotor is

$$\Delta J = 0, \pm 1 \tag{2.39}$$

The allowed symmetry and transition rules (selection rules) for K_{-1} and K_1 in asymmetric rotors are shown in Table 2.3 and Table 2.4 [5].

Dipole Component	**Permitted Transitions**
$\mu_a \neq 0$ (along axis of least moment of inertia)	$ee \longleftrightarrow eo$ $oe \longleftrightarrow oo$
$\mu_b \neq 0$ (along axis of intermediate moment of inertia)	$ee \longleftrightarrow oo$ $oe \longleftrightarrow eo$
$\mu_c \neq 0$ (along axis of greatest moment of inertia)	$ee \longleftrightarrow oe$ $eo \longleftrightarrow oo$

Table 2.3: Asymmetric top transition selection rules as a function of the parity of K. From Gordy and Cook [5]

Dipole Component	ΔK_{-1}	ΔK_1
$\mu_a \neq 0$ (along axis of least moment of inertia)	$0, \pm 2, ...$	$\pm 1, \pm 3, ...$
$\mu_b \neq 0$ (along axis of intermediate moment of inertia)	$1, \pm 3, ...$	$\pm 1, \pm 3, ...$
$\mu_c \neq 0$ (along axis of greatest moment of inertia)	$1, \pm 3, ...$	$\pm 0, \pm 2, ...$

Table 2.4: Asymmetric top transition selection rules as a function of ΔK. From Gordy and Cook [5]

Table 2.3, μ_a, μ_b, and μ_c are the dipole components along principle axes A, B, and C respectively. The ee, eo, oe, and oo notation refers to even-even, even-odd, odd-even, and odd-odd, the evenness or oddness of the K_{-1} and K_1 quasi-quantum numbers respectively.

In Table 2.4 shows the same information as Table 2.3 but in terms of the allowable changes to K_{-1} and K_1.

If a dipole moment lies solely along a principle axis, only the transitions corresponding to that axis' row in the above figures are allowed. If a dipole moment has components along more than one principle axis, all transitions in the rows corresponding to those axes are allowed.

The key points from all of these analyses and all these equations is that the rotational energies for linear molecules, symmetric rotor molecules (including spherical top molecules), and asymmetric rotor molecules, Eq. 2.15, Eq. 2.25, and Eq. 2.38 respectively, are: 1) quantized, 2) functions of angular momentum, and 3) functions of the rotational constants - each of which is a function of the moment of inertia about one of three mutually orthogonal axes. This result is true classically and due to the correspondence principle true quantum mechanically.

2.2.4 Absorption Coupling - The Absorption Coefficient and Intensity

A molecule interacts with THz radiation only if it has an electric or magnetic dipole moment, μ. It is the dipole moment that acts as the coupling mechanism between the molecule and the time varying EM fields of the radiation. Most dipoles are electric in nature. This occurs whenever there is a spatial separation of the negative and positive charges in the molecule. An example of a molecule with an electric dipole moment is water vapor, which will be examined in detail in this work. Although the overall charge of water is neutral, the charges in the water molecule are slightly separated from each other due to the structure of the molecule. This charge separation exists even in the absence of an external electric field. This means that the water molecule has a permanent electric dipole moment and is called

a polar molecule. In the water molecule, there is a net negative charge on the oxygen atom and a net positive charge on the hydrogen atoms. This is sketched in the Fig. 2.6 below.

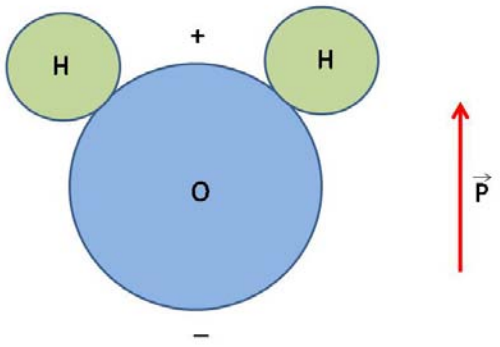

Figure 2.6: Charge distribution and electric dipole moment for the water molecule H_2O.

As can be seen, the oxygen and hydrogen atoms form at 120°angles from each other. This causes a charge distribution in which there is more negative charge on one side and more positive charge on the other. The net result is an electric dipole moment in a direction from the negatively charged oxygen toward the positively charged hydrogen.

The absorption coefficient which describes the strength and intensity of the radiation coupling is given by the expression [4]

$$\alpha = \frac{8\pi^2 N f |\mu_{ij}|^2 \nu^2}{3ckT} \left[\frac{\Delta\nu}{(\nu - \nu_0)^2 + (\Delta\nu)^2} \right] \tag{2.40}$$

where

N = the number of molecules per cc

f = fraction of these molecules in the lower of the two states involved in the transition

$|\mu_{ij}|$ = the dipole moment matrix element for the transition

ν = frequency

ν_0 = resonant frequency or the center of the absorption line

$\Delta\nu$ = half width at half maximum (HWHM)

c = velocity of light

k = Boltzmann constant

T = absolute temperature

Peak absorption occurs at or very near $\nu = \nu_0$ and is given by [4]

$$\alpha_{max} = \frac{8\pi^2 N f |\mu_{ij}|^2 \nu_0^2}{3ckT\Delta\nu} \tag{2.41}$$

The absorption coefficient gives the absorption per unit length. Commonly seen units include dB/km and cm^{-1}. Essentially, the absorption coefficient tells what fraction of the power is absorbed per unit length. This is the same quantity that is used in the exponent of the Beer-Lamber law, Eq. 2.5.

As can be seen in Eq. 2.40 and Eq. 2.41, the absorption coefficient is a function of many parameters. Some key points about these relationships are as follows. First, the absorption coefficient is proportional to the square of the dipole matrix element for the transition. This squared relationship is the key driver behind the absorption intensity. Doubling the dipole moment will quadruple the strength of the coupling interaction with radiation. Second, the absorption coefficient is proportional to N, the molecular density per unit volume of the target molecule. This is essentially pressure. It indicates that higher pressure means more absorption. Third, the absorption coefficient is inversely proportional to temperature. Therefore, the intensity of the absorption tends to diminish with higher temperatures. However, there is an underlying relationship between pressure, temperature, and volume given by the universal gas law

$$PV = nRT \tag{2.42}$$

where P is pressure, V is volume, n is the number moles of gas present, R is the universal gas constant (R = 8.314 J/mol·K, the same for all gases), and T is absolute temperature. Since n and R are constants, and since V is fixed in a given absorption cell, we can say

$$\frac{P}{T} = \text{a constant} \tag{2.43}$$

Therefore the affects of P and T in Eq. 2.40 and Eq. 2.41 will tend to cancel. From a quantum perspective, as the temperature goes up α goes down because more energy levels are populated at higher temperatures. Therefore, the differences in the populations are decreased. This means the primary driver of absorption is the strength of the radiation coupling as given by the dipole moment matrix element μ_{ij}.

2.2.5 Absorption Line Shapes and Widths

In nature, spectral lines, whether absorption or emission, are not strictly lines. They do not exist at only one frequency/wavelength/energy (the energy, frequency, and wavelength are interchangeable terms as related by the Einstein relations Eq. 2.7). They are not δ functions. They are broadened to have a finite width about a center frequency known as the resonant frequency of absorption/emission. This broadening occurs either naturally or due to some perturbation.

The width of a spectral line is quantified by the Full Width at Half Maximum (FWHM) or the Half Width at Half Maximum (HWHM). Both of these measurements are done in the frequency domain or steady state (note: in this work, frequency domain and steady state are synonymous). The FWHF is measured by taking the width of the line at a point equal to 1/2 of the peak amplitude value. Dividing this width by two yields the HWHF. Both of these parameters will be used in this work.

There are five sources of spectral line broadening [4]:

1. Natural line broadening

2. Doppler broadening

3. Pressure (collision) broadening

4. Saturation broadening

5. Wall broadening (as occurs in gas cells or other vessels holding gas, does not occur in the atmosphere)

Natural line broadening arises from the Heisenberg uncertainty principle for time and energy. This is given by

$$\Delta t \cdot \Delta E \geq \hbar \tag{2.44}$$

It has to do with the fact that there is a limit on the natural lifetime of energy states and that an energy state will spontaneously decay (emit) to a lower state. This is true even when the molecule is completely isolated from external perturbations by other particles or radiation. The product of the uncertainty in the natural lifetime of the energy state and the uncertainty in the energy spread must be greater than or equal to a constant, namely the Planck constant. Another way to view this is that, from a quantum mechanical point of view, the natural line broadening is the result with no perturbations. It is the 'natural width' when the molecule is completely isolated from everything else in the universe.

The HWHM for natural line broadening is given by [4]

$$\Delta\nu = \frac{32\pi^3\nu^3}{3hc^3}|\mu|^2 \tag{2.45}$$

As can be seen, the natural line width is a function of resonant frequency and the dipole moment. At THz frequencies it is on the order of 10-100 Hz and therefore insignificant compared to other broadening mechanisms.

Doppler Broadening is due to the motion of the molecule relative to the direction of propagation of the radiation. If the molecule has a component of motion parallel to the

radiation propagation direction, Doppler broadening will occur. If ν_0 is the the resonant absorption frequency of the molecule at rest, and if the molecule has a component of relative motion, v, parallel to the incident radiation, then the frequency of the radiation at which the molecule will absorb will be

$$\nu = \nu_0 \left(1 \pm \frac{v}{c} \right) \tag{2.46}$$

where the + sign corresponds to motion in the same direction as the propagating radiation and the - sign corresponds to motion in the opposite direction as the propagating radiation. The change in frequency, $\nu_0(v/c)$ is called the Doppler shift of the frequency. The Doppler effect, as it is called, causes a change in the frequency of absorption. It causes the absorption frequency to decrease by the Doppler shift (in the lab frame) if the molecule is moving toward the radiation source; conversely the absorption frequency will increase by the Doppler shift (in the lab frame) if the molecule is moving away from the radiation source. Molecular velocity components perpendicular to the radiation propagation direction cause no Doppler shift.

The probability that a molecule in a gas at temperature T will have a velocity v is $e^{\frac{-mv^2}{2kT}}$ where k is the Boltzmann constant and m is the molecular mass. The line shape function or intensity is then given by [5]

$$I = I_0 e^{-\frac{mv^2}{2kT}\left(\frac{\nu-\nu_0}{nu_0}\right)^2} \tag{2.47}$$

where I_0 is the intensity without the Doppler shift. The Doppler broadened line is therefore symmetric with HWHM of [4]:

$$\Delta\nu = \frac{\nu}{c}\sqrt{\frac{2kT}{m}\ln 2} = \frac{\nu}{c}\sqrt{2kN_0 \ln 2}\sqrt{\frac{T}{M}} \simeq 3.581 \text{ x } 10^{-7}\sqrt{\frac{T}{M}}\nu \tag{2.48}$$

where M is the molecular weight in g/mol and N_0 is Avogadro's number. For a given molecular species, with M constant, Doppler broadening is strictly a function of temperature at a given resonance. Note also the the ν^2 (frequency squared) dependence in the exponent makes the line shape function a Gaussian shape for the Doppler broadened line. This fact will be of great consequence latter in the Experimental chapter of this thesis when we see how line shape data is fitted to a defined curve.

Fig. 2.7 [5] below shows the normalized shape of Doppler broadened lines for three ratios of p/p_c, where p is pressure and p_c is the pressure at which collision broadening begins to become significant. The pressure $p = p_c$ is where collision broadening starts to dominate Doppler broadening. The normalization is α_ν/α_{max} where α is the absorption coefficient.

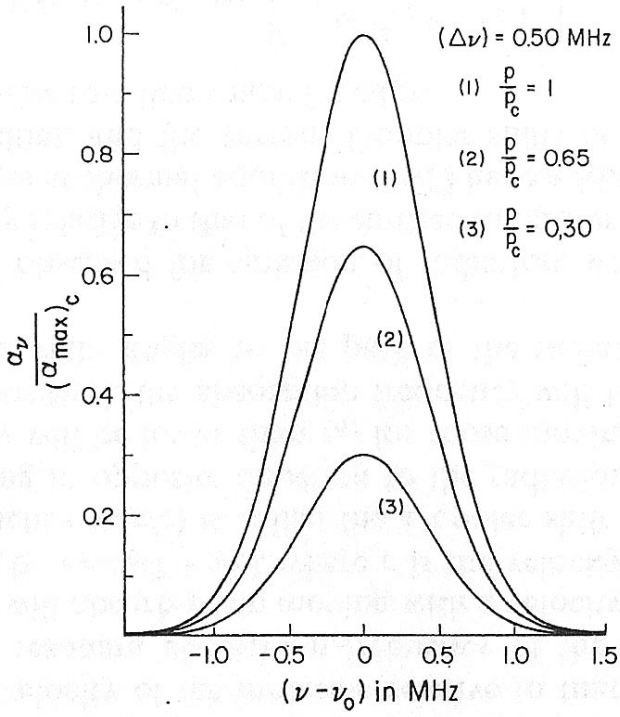

Figure 2.7: Shape of Doppler broadened lines. From Gordy and Cook [5].

Pressure broadening, also called collision broadening, is the most important broadening mechanism in the THz region. By far, it dominates the other mechanisms in the Earth's

atmosphere. Pressure broadening arises from binary collisions between molecules. Some assumptions are made in the theoretical development of pressure broadening. First, it is assumed that the collision is instantaneous. This means that the collision time (the amount of time the molecules spend interacting with each other), τ, is negligible compared to the mean time between collisions, Δt (typically $\tau \lesssim 1$ ps and $\Delta t \gtrsim 1$ ns). Second, it is assumed that a collision is strong so that after the collision the molecule has no memory of what its state or orientation was before the collision. Finally, third, it assumes that after collision, the molecule will be in a non-polarized (i.e. random) state.

However, all collisions do not induce transitions. Further, transitions may be induced by long range interactions which are not collisions in the classical sense. For instance, a molecule may interact with the dipole field of another molecule upon approach. The dipole field of the second molecule can cause a perturbation in the first molecule without any actual "collision" between the two molecules. Therefore, pressure broadening also depends on the properties of the molecules as well as the velocity distributions and mean time between collisions. The pressure broadened line shape at low pressures (pressures at which $\Delta\nu \ll \nu_0$) is given by [5]

$$I = \frac{1}{\pi}\left[\frac{\Delta\nu}{(\nu_0 - \nu)^2 + (\Delta\nu)^2}\right] \tag{2.49}$$

where

$\Delta\nu = \frac{1}{2\pi\tau}$

τ = mean time between collisions

ν_0 = resonant frequency

This is a Lorentzian shape and in fact is the final term in Eq. 2.40. Fig. 2.8 [5] below shows the normalized Lozentzian shape of pressure broadened lines for three pressures of 1 mm Hg, 0.5 mm Hg, and 0.1 mm Hg (1 mm Hg = 1 mTorr). The normalization is α_ν/α_{max}

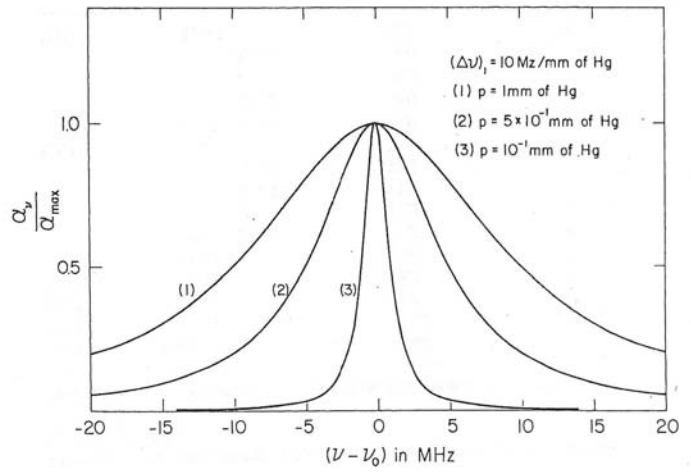

Figure 2.8: Shape of pressure broadened lines in the pressure range where line width is directly proportional to pressure. Lorentzian line shape. From Gordy and Cook [5].

where α is the absorption coefficient, same as in Fig. 2.7.

The absorption coefficient is then given by Eq. 2.40 and repeated here for convenience: [4]

$$\alpha = \frac{8\pi^2 N f |\mu_{ij}|^2 \nu^2 \Delta\nu}{3ckT[(\nu - \nu_0)^2 + (\Delta\nu)^2]} \tag{2.50}$$

where

N = the number of molecules per cc

f = fraction of these molecules in the lower of the two states involved in the transition

$|\mu_{ij}|$ = the dipole moment matrix element for the transition

ν = frequency

ν_0 = resonant frequency or the center of the absorption line

$\Delta\nu$ = half width at half maximum (HWHM)

c = velocity of light

k = Boltzmann constant

T = absolute temperature

The key points about the Lorentz theory of collision are the assumptions of instantaneous collisions, strong collisions, and of non-polarized distributions after collision.

The Lorentzian assumption noted above is true when $\Delta\nu \ll \nu_0$. This means that the Lorentzian line shape is perfectly valid at very low pressure and in the optical regions as well. However at higher pressures, $p \geq 10$ mTorr, in the THz region, deviations between calculated Lorentzian lines shapes and measured line shapes become apparent. The non-polarized distribution assumption breaks down. For these higher pressures, the Van Vleck-Weisskopf line shape function is a better fit. The Van Vleck-Weisskopf (VVW) line shape was developed in a landmark 1945 paper by J. H. Van Vleck of Harvard University and V. F. Weisskopf of Rochester University. The VVW line shape is given by [5]

$$I = \frac{1}{\pi}\left[\frac{\Delta\nu}{(\nu_0 - \nu)^2 + (\Delta\nu)^2} + \frac{\Delta\nu}{(\nu_0 + \nu)^2 + (\Delta\nu)^2}\right] \tag{2.51}$$

and the absorption coefficient with the VVW line shape is then

$$\alpha = \frac{8\pi^2 N f |\mu_{ij}|^2 \nu^2}{3ckT}\left[\frac{\Delta\nu}{(\nu - \nu_0)^2 + (\Delta\nu)^2} + \frac{\Delta\nu}{(\nu_0 + \nu)^2 + (\Delta\nu)^2}\right] \tag{2.52}$$

where the parameters are the same as those listed above. The VVW is shown in the figure below [5]

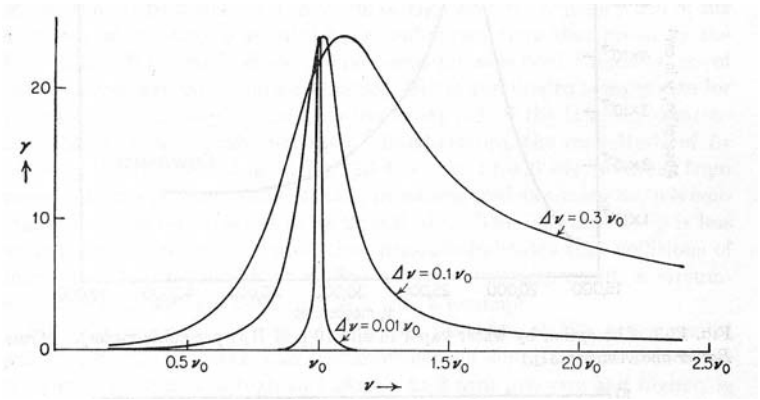

Figure 2.9: VVW shape for pressure broadened lines. From Gordy and Cook [5].

In looking at the equations for the Lorentzian line shape, Eq. 2.49, and VVW line shape, Eq. 2.51, one notices that they are almost the same. The VVW function has an additional term $\frac{\Delta\nu}{(\nu_0+\nu)^2+(\Delta\nu)^2}$. At lower pressures and in the optical regime, $\Delta\nu \ll \nu_0$, this term tends to vanish and the VVW line shape tends to go to the Lorentzian line shape.

The VVW line shape is derived with almost the same assumptions as the Lorentzian but with one major difference. It does not assume random molecular orientations after collisions but rather assumes a Boltzmann distribution about a value characteristic of the instantaneous EM field at time t_0, the time of collision. Further, the Lorentz model only takes into account resonant absorption. There is, however, non-resonant absorption as described by the Debye model [26]. The Lorentz model predicts no absorption at all if the resonant frequency is zero. VVW posited that this was incorrect and that the true result is given by the Debye formula for static polarization [27]. The main effort of VVW, in their original 1945 paper, was to develop an unifying theory of pressure broadening absorption that combined the resonant absorption model of Lorentz with the non-resonant absorption model of Debye. As part of their original paper, VVW derived the absorption coefficient using the Debye model. The Debye model method yielded [27]

$$\alpha = \frac{\omega}{c}\frac{4\pi N\mu^2}{3kT}\frac{\omega\tau}{1+\omega^2\tau^2} \tag{2.53}$$

which gives absorption per unit length. In this equation ω is the radiation frequency, N is the number of molecules/cc, μ is the dipole moment, τ is the mean time interval between collisions, k is the Boltzmann constant, T is temperature, and c is the speed of light.

In Eq. 2.49 when ν_0 = 0, the result is zero. VVW maintained that the results should be Eq. 2.53. To correct this, VVW modified the Lorentz model by changing the initial conditions of the equation of motion from $x(0) = 0$ and $\dot{x}(0) = 0$ to a Boltzmann distribution for H [27]

$$H(t) = \frac{p^2}{2m} + \frac{1}{2}m(\omega_0 x)^2 - ex\mathcal{E}\cos\omega t, (p = \dot{x}) \tag{2.54}$$

From this they arrived at Eq. 2.51.

VVW discussed some caveats to their model in their original paper. One assumption in particular seemed to give them reservations. In their theoretical development, VVW assumed that only a single relaxation time, τ, existed. In other words, on average, all molecules had the same mean collision times. If this were not true, then a dispersion of relaxation times would occur and τ would not be a constant but a function of either the molecule or the radiation or both. Further, VVW believed that such a dispersion of relaxation times would cause the absorption of the wings of the line to be more intense than predicted by Eq. 2.52 [27]. This concern proved to be very legitimate. It turns out that the VVW model does not agree with measure data in the wings and that in fact VVW underestimates the intensity of the absorption in the wings. VVW did not resolve this issue and the literature does not seem to have any follow up papers by VVW addressing this.

A third line shape was developed by E. P. Gross of MIT in 1955 [28]. This model yielded what later became known as the kinetic line shape. In VVW, a Boltzmann distribution was assumed after an instantaneous impact. The Boltzmann distribution is about a value appropriate for the applied field at the time of collision. This allowed for the calculation of both dynamic and static polarizations. The static polarization being the Debye result. Gross argued that as ω_0 approaches zero, one does not obtain the polarization of a free electron gas as postulated by VVW. He maintains that the Debye result is unnecessary for a resonant frequency of zero because the Debye relaxation time is not the same as the time between collision. Further, the VVW model implies very large velocities during collisions. Gross argued that this was incorrect since $\tau \ll \frac{1}{\nu}$ and E $\simeq$ kT. Further, he points out that in order to achieve its Boltzmann distribution value after collision, a molecule must jump a finite amount instantaneously thus requiring an infinite velocity. Gross assumed instantaneous collision, like VVW, but unlike VVW he assumed that the positions of the

molecules were unchanged after the collision and that they could be modeled as oscillators. These oscillators have a Maxwellian distribution of velocities after impact. These assumptions result in the line shape of a friction damped oscillator (radiating oscillator moving under the influence of a viscous resistance). Note that for collision frequencies much smaller than the resonance frequency, $\nu_c \ll \nu_0$, the kinetic line shape approaches the VVW line shape. However, for $\nu_c \simeq \nu_0$, the kinetic line shape is less distorted and agrees better with measured line shapes at pressure approaching 1 atm. The kinetic line shape is given by [3]

$$I = \frac{1}{\pi} \frac{4\nu\nu_0\Delta\nu}{(\nu^2 - \nu_0^2)^2 + 4\nu^2(\Delta\nu)^2} \tag{2.55}$$

and the absorption coefficient is given by

$$\alpha = \frac{8\pi^2 N f |\mu_{ij}|^2 \nu^2}{3ckT} \left[\frac{4\nu\nu_0\Delta\nu}{(\nu^2 - \nu_0^2)^2 + 4\nu^2(\Delta\nu)^2} \right] \tag{2.56}$$

2.2.6 Anomalous Absorption in the Far Wings and Continua - Why the Discrepancies?

We have three semi-classical models for line shape in the THz regime: Lorentz, VVW, and kinetic. The later two were developed in succession with the intent of improving on the previous works. Hard as it may be to believe though, none accurately predict absorption in the THz region. All of these line shapes underestimate the far wing behavior of absorption at high pressures (P $\simeq$ 1 atm). This phenomena is known as anomalous absorption. Perhaps the discrepancy is understandable for the Lorentzian line shape. It was originally developed by H. A. Lorentz whose interest was in the optical regime where it was quite adequate [27]. However, both the VVW and kinetic line shape models were developed with the microwave, MMW, and sub-MMW regions in mind and both fail to explain anomalous absorption.

Interestingly enough, the VVW and kinetic line shapes are used ubiquitously by workers in the molecular spectroscopy field and have been for years. This is done knowing of the uncertainty in the far wings. Several years after the Gross paper, the Gaut/Reifenstein (G/R) correction factor was calculated empirically as a fudge factor for the kinetic line shape [6]. Derivation of the G/R correction term is fairly complicated but the result is fairly simple [6]

$$\Delta\alpha_\nu = 4.69 \text{ x } 10^{-4}\left(\frac{300}{T}\right)^{3.1}\left(\frac{P}{1000}\right)\nu^2 \tag{2.57}$$

in dB/km. When the G/R correction factor is added to the kinetic line shape, the resulting line shape is in very close agreement with measured line shape. Note, at the time of the literature's printing (1979), the G/R correction factor adjustment was tested and known to be valid only at T = 300 K and P = 1000 mbar. The following figure shows a plot of the measured line shape, VVW line shape, unadjusted kinetic line shape, and the kinetic line shape adjusted with the G/R correction factor [6].

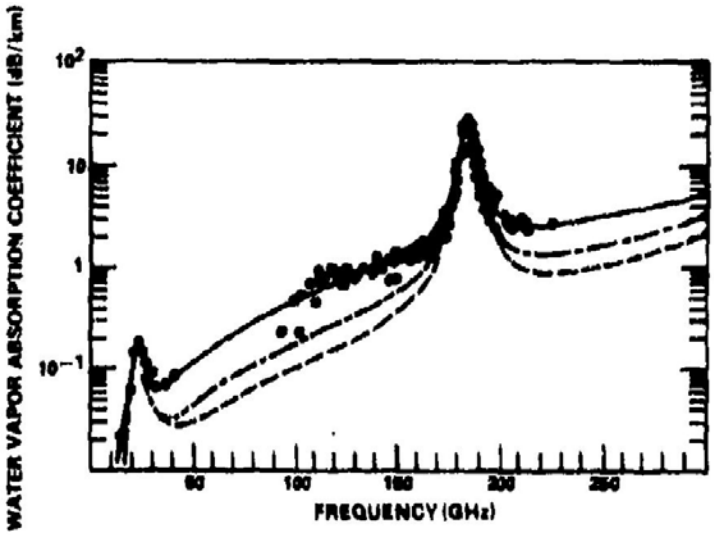

Figure 2.10: Comparison of calculated and measured H_2O absorption; VVW (long dashed line), kinetic(short/long dashed line), kinetic with correction(solid line), and measured(dots). From Kulpa and Brown [6].

Shown next is the discrepancy between the measured line shape and G/R correction versus frequency [6].

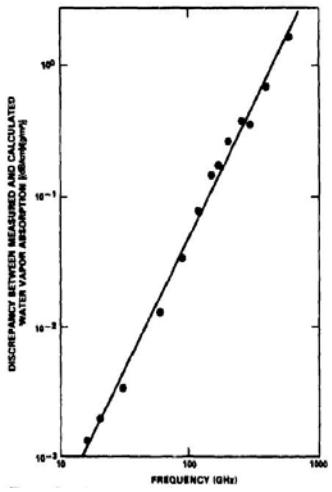

Figure 2.11: Measured anomalous absorption (dots) and G/R correction factor (straight line) versus frequency. From Kulpa and Brown [6].

As can be seen, the G/R correction factor tracks anomalous absorption quite well from the microwave into the THz regions (10 - 1000 GHz).

Having a fudge factor is not the same as having an explanation of why it works and why it is needed. At this point, the origin of excess (anomalous) absorption is not understood very well. The most promising theory is that the impact assumption made in the Lorentz, VVW, and kinetic theories is not completely correct. These models all assume that the dipole moments of the colliding molecules are constant over the entire duration of the collision. In other words, these models all assume instantaneous collisions between rigid molecules. Contrary to this, it is possible that the dipoles are changing over the t $\leq$ 10^{-12} seconds due to collision deformation. This phenomena is called Collision Induced Absorption (CIA). There is evidence that collision induced absorption leads to transient dipole moments which in turn cause broad, non-resonant absorption in the far wings of an absorption line.

It has been shown by Ben-Reuven [29] that absorption is proportional to ν^2 times the

Fourier transform of the autocorrelation function of the dipole moments. Therefore, Fig. 2.11 implies that this transform is constant up to frequencies of 10^{12} Hz. Collision induced dipole moments may exist for times shorter than typical collision times (1 picosecond).

If collision induced absorption is the origin of anomalous absorption, then studying the transient behavior of molecular rotational transitions should eventually yield more insight into the problem. It is in that spirit that transient spectroscopic methods were used in this study and are discussed later in this work.

2.3 Scattering

Scattering of THz radiation by atmospheric constituents is the second major cause of attenuation in the atmosphere. From a microscopic level, scattering occurs when photons, "collide" with scatterers. Scatterers can be atoms, molecules, or other larger particles in the atmosphere. The word collide is in parenthesis to emphasize the point that a collision between a photon and a scatterer, say a molecule, is not a collision in the classical sense. A photon is not a solid. It is a quanta of EM energy. Its position and momentum are described by quantum wave functions. Similarly, the position and momentum of the molecular are described by quantum wave functions. Therefore, the photon does not actually come into contact with the molecule. However, the two can get close enough in space so that their quantum wave functions overlap. When this occurs, the photon interacts with the molecule and is either absorbed or repulsed. If the energy of the photon matches a resonant energy of the molecule, the photon will be absorbed. Absorption has already been discussed. If the energy of the photon does not match the resonant energy of the molecule, the photon will be scattered. The details of this process are described using quantum electrodynamics and are beyond the scope of this study. Feynman provides an accessible introduction to this topic [30].

Scattering collisions can be inelastic or elastic. In both cases the momentum and the

energy of the photon-molecule system is conserved. Momentum is always transfered between the photon and the molecule in inelastic and elastic collisions. However, energy is only transfered in inelastic collisions. Compton scattering of X-rays is an example of inelastic collision scattering. In this work, we will only be concerned with THz radiation. Photons with energies in the THz range only have elastic collisions with molecules. Therefore, there is no energy transfer between the photon and the molecule in a THz scattering event (the energy of the photon and the frequency of the radiation is unchanged by the collision).

Photons travel at the speed of light but have no rest mass. All of a photon's mass is relativistic (due to its energy). Therefore, one THz photon has a very small fraction of the mass of a molecule and only a small fraction of the momentum of a molecule. The effect of a scattering event on the momentum of a molecule is negligible. The effect of the scattering event on the momentum of a photon is appreciable. Its trajectory is altered. At the macroscopic level, the change of the trajectories of individual photons manifests itself as a divergence or spreading out of the electromagnetic wave like the ripples in a pond after a stone is dropped in. This results in the power of the propagating signal being spread out instead of being concentrated on a target. The intensity of the propagating radiation that reaches the target is diminished by scattering. The power received is less than what it would have been without the scattering event. In a word, the propagating radiation is attenuated.

There are three types of elastic electromagnetic scattering: Rayleigh scattering, Mie (or resonant) scattering, and optical scattering. Which of these occurs depends on the ratio of the size of the scatterer to the wavelength of the radiation. The size of the scatterer is defined by its Radar Cross Section (RCS), σ. The RCS of a scatterer is the area of scatterer normal to the direction of propagation of the radiation. Fig. 2.12 shows the scattering results for different ratios of scatterer size to incident radiation wavelength [7].

Rayleigh scattering occurs when the wavelength of the radiation is much larger than the physical size of the scatterer ($\lambda >> \sigma$). A typical threshold is about $\sigma/\lambda \approx 1/10$ [8]. In

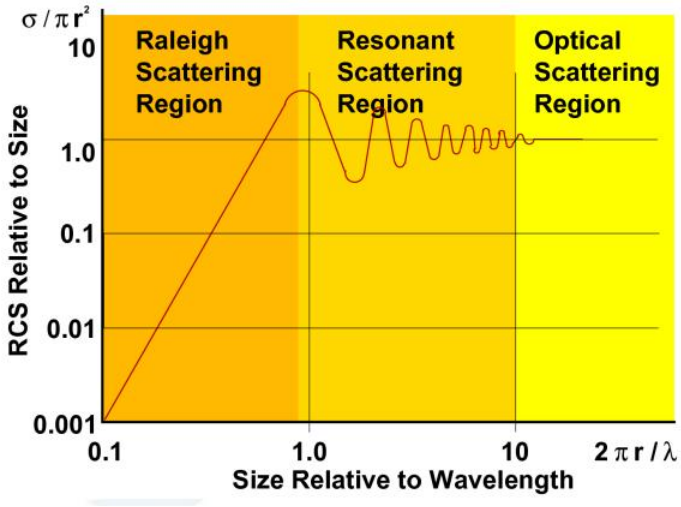

Figure 2.12: The type of scattering depends on the size of the scatterer and the wavelength of the radiation. From Kopp [7].

the Rayleigh regime, the intensity of the scattering is roughly proportional to the physical size of the scatterer. As the wavelength is reduced, for a given scatterer RCS, the resonant or Mie scattering regime is entered. In this regime, the wavelength of the radiation is comparable to the size of the scatterer. The Mie regime is characterized by the strong fluctuation of the scattering intensity with wavelength and aspect (angle of incidence). For this reason, it is also called the resonant regime. Further reduction in wavelength brings one to the optical scattering region. In this region, the intensity of the scattering is independent of the size of the scatterer and the rules of geometric optics apply.

For THz radiation, wavelengths are on the order of 1 mm. Table 2.5 shows what scattering regime would be expected for various scatterers in the atmosphere [31].

Object	Size	Relative Size (σ/λ)	Regime
Atom	1 Å	1×10^{-7}	Rayleigh
Molecule	2.78 Å	2.78×10^{-7}	Rayleigh
Fog Droplet	50 μm	0.05	Rayleigh
Small Raindrop	0.5 mm	0.5	Mie
Large Raindrop	4.0 mm	4.0	Mie
Hailstone	20 mm	20	Optical

Table 2.5: THz scattering regime for various atmospheric scatterers.

Table 2.5 says that for THz radiation incident on small particles, up to the size of fog droplets, Rayleigh scattering dominates. For all but the largest hydrometeors, Mie scattering dominates. However, this does not tell how much scattering will occur. For instance, a heavy downpour will scatter much more THz radiation than a light drizzle, even though both are in the Mie regime. This can be inferred from Fig. 1.2. Note the 10 db/km increase in attenuation of THz radiation when the rainfall rate increases from 2 mm/hr to 25 mm/hr. This is due to the increase in the number of scatterers when the rainfall rate is increased. The attenuation is a function not only of the type of scattering but the number of scatterers.

Fig. 2.13 shows how the direction of the propagating THz radiation is altered by Rayleigh and Mie scattering [8].

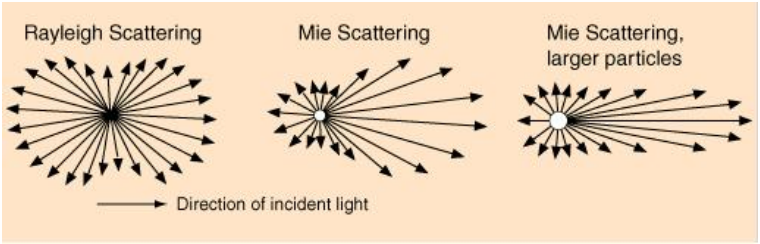

Figure 2.13: Scattering directions for Rayleigh and Mie scattering. From Nave [8].

As can be seen, scattering produces a pattern not unlike that produced by an antenna. For Rayleigh scattering the pattern is like that of a dipole antenna. Most of the energy of the scattered wave propagates off at angles between $\pm 90^\circ$ from the incident radiation. The intensity of the scattering is given by [8]:

$$I = I_0 \frac{8\pi N \alpha^2}{\lambda^4 R^2} (1 + \cos^2 \theta) \tag{2.58}$$

where I_0 is the intensity of the incident radiation, N is the number of scatterers, α is the polarizability, and R is the distance from the scatterer to the observer. Note that the intensity of the scattered radiation is inversely proportional to 4th power of the the wavelength

and is mostly collinear with the incident radiation. Rayleigh scattering favors shorter wavelengths. This is why the sky overhead is blue (Rayleigh scattering of EM radiation at optical wavelengths). It also means that the intensity of Rayleigh scattered THz radiation is weak. It is almost negligible in all but collinear directions.

Mie scattering is more directional than Rayleigh scattering. Mie scattering has a dominate forward scattering component. The forward lobe of the Mie pattern becomes sharper and more intense for larger particles. Mie scattering is the dominate type of scattering for THz radiation. Mie scattering is the result of the Mie solution to Maxwell's equations for radiation incident on a sphere of diameter $d \sim \lambda$. In this formulation, the incident radiation and the scattering field are expanded into radiating spherical vector wave functions. When the boundary conditions are applied on the spherical surface, the expansion coefficients of the scattered field can be calculated and an analytical solution derived. Unfortunately, closed form solutions to Mie scattering problems are only available for the simplest scattering shapes (spheres and ellipsoids). More complicated shapes require numerical analysis. Good discussions of the Mie scattering solution may be found in either Straton [32] or Jackson [33].

Steady State (Frequency Domain) Experiments

3.1 Previous Studies

Over the past 65 years, many investigators have studied the absorption of electromagnetic radiation by water vapor from both theoretical and experimental standpoints [34] [35] [36] [37] [38]. These studies started out by looking at the 22 GHz absorption line of water vapor as this line was within reach of the technology available in those earlier days. As time and technology progressed, investigations of higher energy transition lines were undertaken. At present, most if not all of the absorption lines of water vapor have been studied experimentally using standard and novel frequency domain techniques. NASA's Jet Propulsion Laboratory (JPL), at the California Institute of Technology, has compiled a large database which contains information on the rotational and lowest lying vibrational transition lines for many molecular and atomic gas species including water vapor [25].

3.2 This Study

Several experiments were done to study the absorption line shapes of H_2O at two frequencies and various pressures. The absorption lines measured are given in Table 3.1 below [25].

At atmospheric pressure, both of these lines reside in the far wings of the very strong absorption line at 556.9 GHz.

Frequency(MHz)	Transition(J_{K_{-1},K_1})	Transition Strength (Log I)
325152.919	$5_{1,5} \leftarrow 4_{2,2}$	-3.566
620700.807	$5_{3,2} \leftarrow 4_{4,1}$	-2.761

Table 3.1: H_2O absorption lines studied.

Note, the Transition Strength is the base 10 logarithm of the integrated intensity in units of nm^2 MHz at 300 K.

The 620 GHz line was studied first due to its stronger intensity. The line was initially studied using frequency domain absorption spectroscopy. In this method the molecules, contained in a microwave gas cell at low pressure, were swept with MMW radiation across a broad frequency range centered on the resonant absorption frequency. The absorption lines were measured with a MMW detector and oscilloscope. This procedure was repeated over a range of pressures. A curve was fitted to data for each absorption line. The FWHM at each pressure was calculated from the corresponding fitted curve. This resulted in a set of FWHM values for this absorption frequency. The FWHM values were then plotted against pressure. A weighted average straight line was fitted to this plot as the FWHM vs. pressure relation was linear, as was expected. The slope of the fitted line, called the pressure broadening parameter, γ, was calculated and compared against published results. The calculated value of γ agreed closely with the published value as will be seen below. This initial experiment proved that the equipment function, experimental methods, and the curve fitting calculations were correct.

3.3 Equipment and set up

A diagram for the general equipment set up is given in Fig. 3.1. Also included are some photographs of the setup and some close up photographs of the VDI transmitter, VDI re-

ceiver, and the gas manifold (Fig. 3.2 - 3.6). Some alterations did occur during different experiments. These alterations will be described in detail when a specific experiment is discussed.

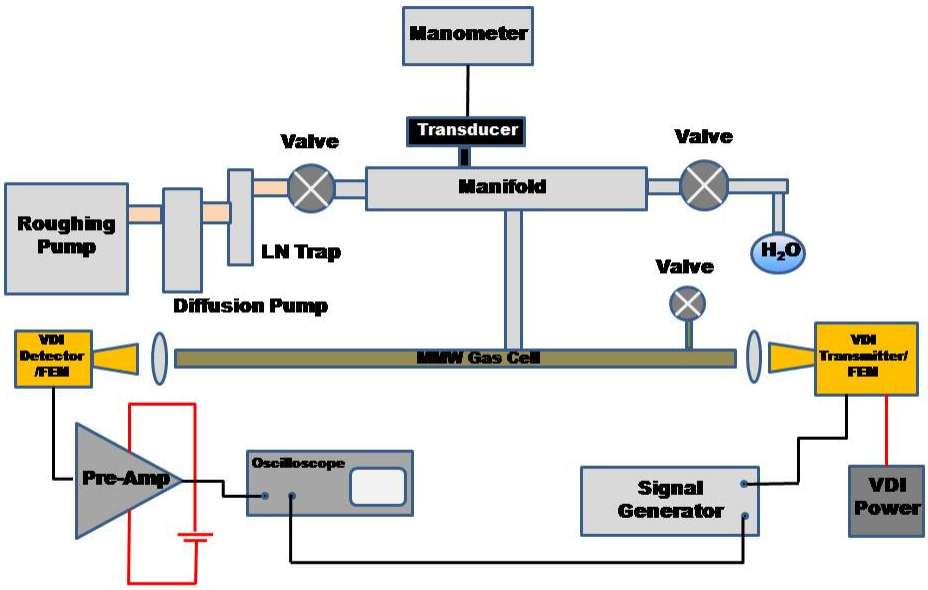

Figure 3.1: Block diagram of the basic experimental setup.

The MMW radiation was generated by an Agilent signal generator (synthesizer), model E8254A. The E8254A is capable of generating a range of signals with varying frequencies, amplitudes, and modulation schemes. For this experiment, frequency modulation (FM) was used. Other specific settings used on the signal generator will be discussed with the specific experiments. A Radio Frequency (RF) FM signal was sent from the signal generator to the Virgina Diodes Incorporated (VDI) transmitter/frequency extension module (FEM). The VDI transmitter module used 48x and 24x multiplier chains to up-convert the incoming signals from microwave to THz. These multiplier chains had output ranges of

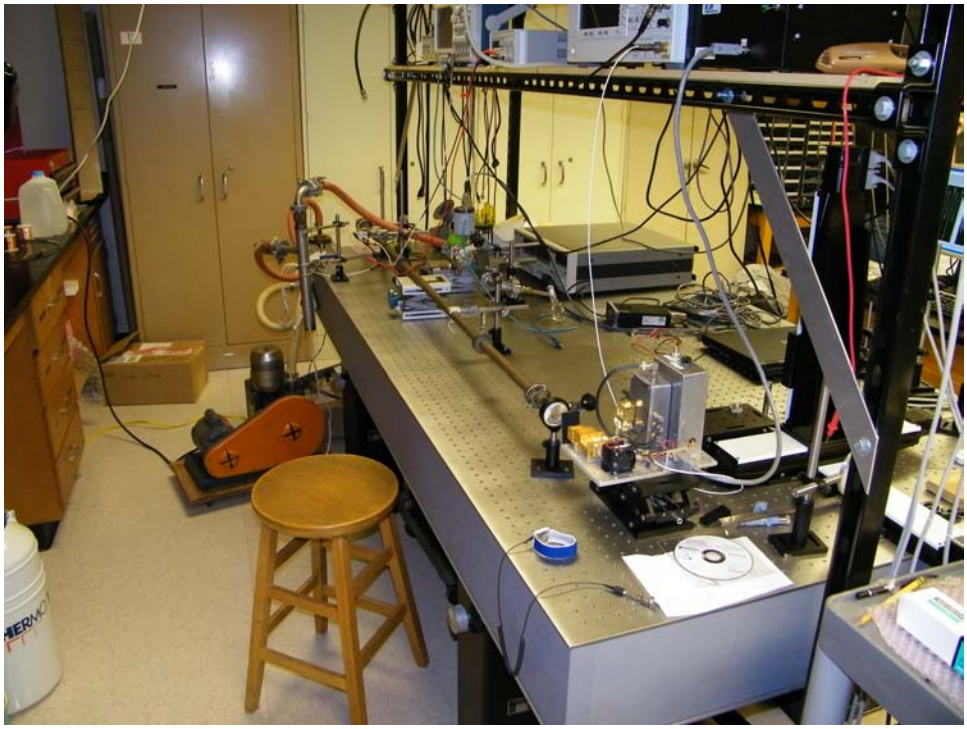

Figure 3.2: Experimental setup as viewed from the right. Note the gas cell, optics, and VDI transmitter in foreground

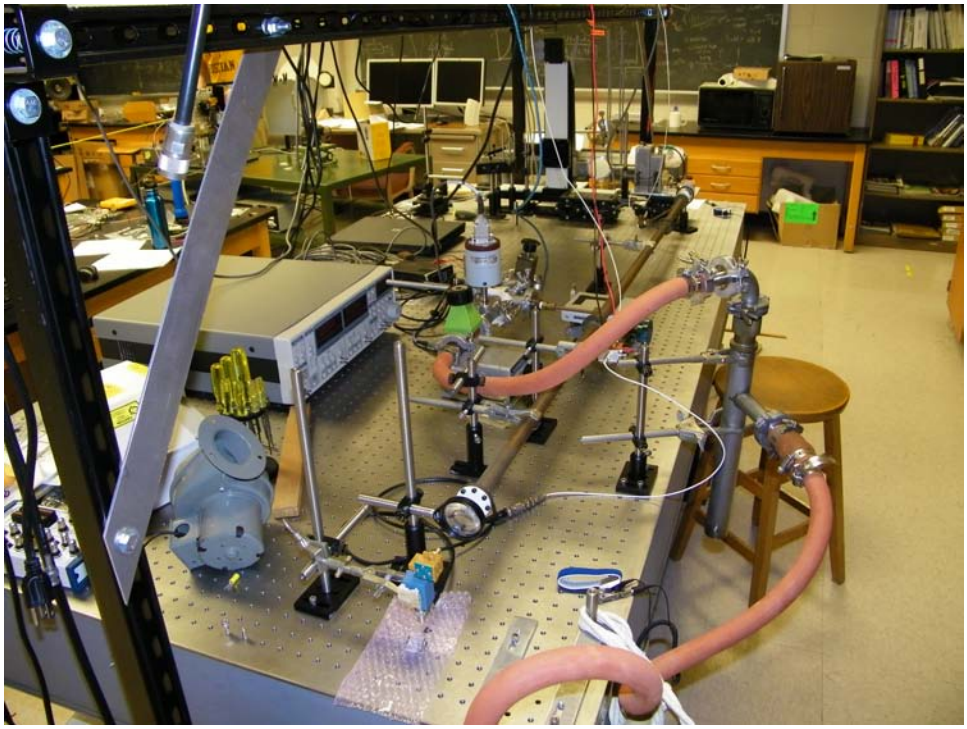

Figure 3.3: Experimental setup as viewed from the left. Note the gas cell, optics, VDI receiver, gas manifold, pressure transducer, gas hoses, and LN trap in foreground

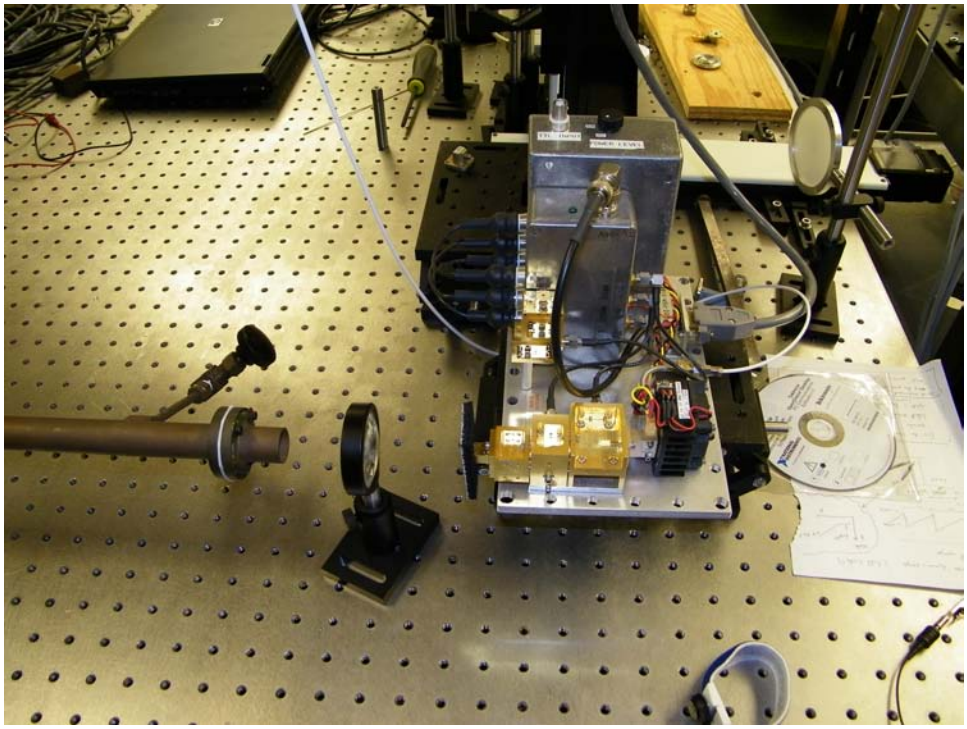

Figure 3.4: Close up of the VDI transmitter, optics, and gas cell input.

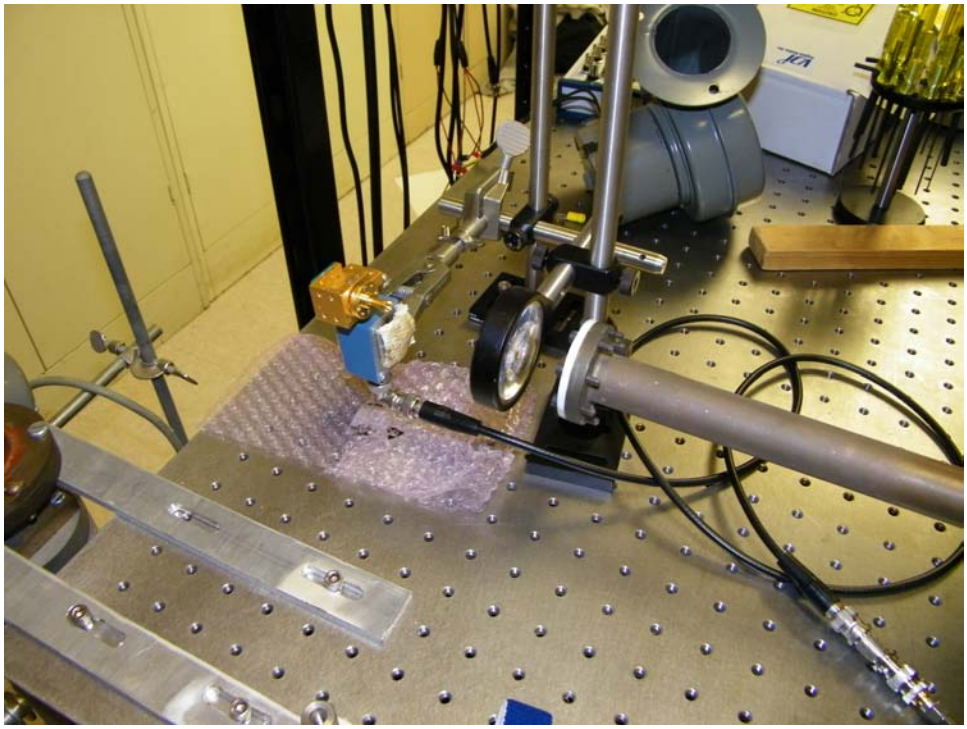

Figure 3.5: Close up of the VDI receiver/detector, optics, and gas cell output.

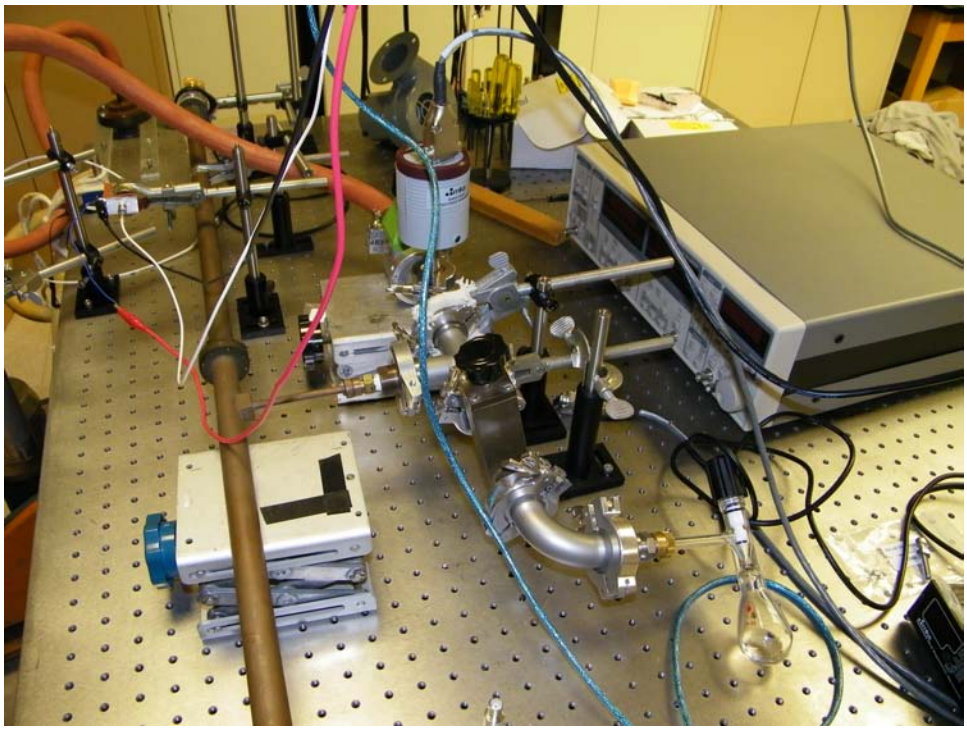

Figure 3.6: Close up of the gas manifold and control valves. Also shown is the manometer's pressure transducer on top of the manifold.

580 - 655 GHz and 290 - 330 GHz respectively. Once at THz frequencies, the signals were launched into space from a transmitting horn antenna. The propagating beam was focused into the gas cell input aperture by a 2" diameter concave lens (Thor Labs). The gas cell used was essentially a brass tube, 168 cm in length and 2.0 cm in diameter. It was hermetically sealed at both ends with Teflon windows. Teflon is transmissive to THz radiation and seals the gas inside the cell. The radiation beam emerged into free space through the gas cell output aperture where it was focused by another 2" diameter concave lens (Thor Labs) into the receiving horn antenna. From there the beam was incident on a VDI diode detector. Two detectors were used. For 620 GHz, a VDI model WR1.5ZBD was used. This is a Zero Bias Detector with a rated usable detection range of 500 - 750 GHz. Its peak sensitivity is at 600 GHz. Sensitivity falls off for frequencies above 600 GHz. At 620 GHz its sensitivity is about 1500 V/W. For the 325 GHz measurements, a VDI model WR3.4SHM was used. This is a Sub Harmonic Mixer with a rated usable detection range of 220 - 325 GHz.

Its minimum mixer noise temperature is at approximately 240 GHz increasing for larger frequencies. The mixer noise temperature at 325 GHz is not specified but its noise temperature at 270 GHz is about 1500 K. Note, the SHM has a higher bandwidth than the ZBD. The output of the detector was sent to a Stanford Research Systems (SRS) Model SR5600 low noise preamplifier. During these experiments, the preamplifier was powered from its own integrated battery circuit so no 60 Hz noise source was coupled. The output of the preamplifier was sent to a Tektronix DPO3014 digital phosphorous oscilloscope where it was recorded. In addition, a Low Frequency modulating signal (FM ramp or triangle wave used to modulate or sweep the frequency) was sent from the signal generator directly to the oscilloscope as a trigger and recorded as needed. The oscilloscope was set to acquire data in Average Mode with 512 samples per average. Other specific settings will be addressed below.

The gas handling apparatus in this experiment consisted of a 168 cm long x 2.0 cm diameter gas cell, a gas manifold, a glass flask to hold the water supply, two hand valves, a diffusion pump, a roughing pump, and an MKS Baratron Capacitance Manometer Model 626A02TDE (0 - 2 Torr $\pm$ 0.25 $\%$). The manometer was powered by an MKS PDR 2000 which is a combination power supply, readout, and cabling system. The glass flask was filled with water and the system sealed. The cell and manifold were then pumped down to below the vapor pressure of H_2O, approximately 20 mTorr at room temperature. The valve between the flask and the gas manifold was then momentarily opened. This caused the water vapor molecules in the flask to escape into the gas manifold and the interconnected gas cell. This water vapor was then used in the experiment. The roughing pump was used to bring the pressure inside the gas manifold and cell down into the milli-Torr (mTorr) range. The diffusion pump was then engaged to further reduce the pressure down into the single mTorr pressure range or lower as needed.

3.4 Frequency Domain Study of the 620 GHz Line

The first experiment was the study of self broadening on the 620 GHz absorption line using MMW absorption spectroscopy. This is a steady state or frequency domain technique. In this experiment, the signal generator was set up to sweep, via a ramp function, through a range of frequencies centered around the resonant frequency of 620.701 GHz. Since the signal generator RF output frequencies were multiplied 48x by the VDI Transmitter, the center frequency on the signal generator was set to 12931.26681 MHz. The modulation was FM via a positive ramp function. The modulation rate was set to 3 kHz. The modulation depth was set to 1 MHz which corresponded to $\pm$ 48 MHz on the VDI output. The amplitude of the Agilent synthesizer was set to 10 dBm (decibels - milliwatt). The internal reference used by the LF output was set to 1 Vpp. The oscilloscope vertical settings were: 200 mV/div, DC coupled, and 0 V offset. The horizontal setting was 10 μs/div. The acquisition settings were 10k points per sweep and average acquisition mode using 512 sweeps. The tables below summarize the synthesizer and oscilloscope setups.

Modulation	FM
Modulating Waveform	Positive Ramp
Frequency(MHz)	12931.26681
FM Deviation(MHz)	1.000
FM Rate(kHz)	3.000
Amplitude(dBm)	10.0
FEM Transmitter Output(mW)	0.700

Table 3.2: Signal generator setup for 620 GHz absorption line spectroscopy

Vertical Scale	200 mV/div
Horizontal Scale	10 μs/div
Channel 1	Signal Generator LF output
Channel 2	Preamplifier output
Trigger	CH 1
Coupling	DC

Table 3.3: Oscilloscope setup for 620 GHz absorption line spectroscopy

The absorption lines were initially measured at the VDI detector for pressures of 10, 20, 30, and 40 mTorr. A typical example of the input sweep and the absorption line output can be seen in the figure below.

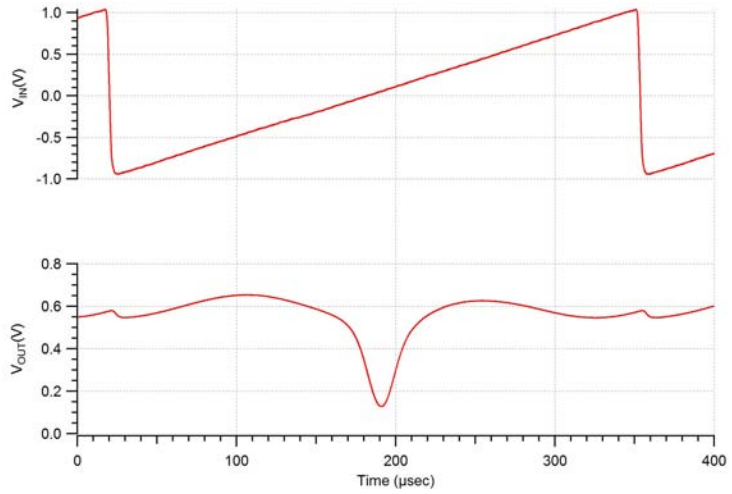

Figure 3.7: Input and output signals as seen on the oscilloscope. Note: CH1 is the input sweep, CH2 is the preamp output. Oscilloscope time base at 40 μsec/div.

After the data was taken, a curve was fitted to each absorption line. Igor Pro version 6.12A by Wavemetrics Corporation was used to fit and analyze the data. The curves were fitted to a Voigt profile. A Voigt profile is a lineshape that results from the convolution of a Gaussian lineshape with a Lorentzian lineshape. Voigt lineshapes are described by a ”shape” parameter. The value the shape can range from zero to infinity corresponding to a profile that is more Gaussian or more Lorentzian respectively. During the curve fitting process, the lineshape data had to be rescaled to reflect the fact that the ordinate (x-coordinate) was actually frequency not time. The frequency calibration procedure used in this analysis and subsequent analysis of the 325 GHz line is as follows. The time scale needed to be changed into a frequency scale. The FM sweep rate setting on the signal generator was 3.000 kHz. This corresponded to a sweep period of 333.3 μs. The FM depth on the signal generator was $\pm$1.000 MHz, or 2.000 MHz total. This corresponds to a $\pm$48.0 MHz or 96.0 MHz at the VDI transmitter output. Therefore, a 10 μs/div time scale on the oscilloscope

was really a 2.88 MHz/div frequency scale since

$$\frac{333.3\mu s}{10.0\mu\text{s/div}} = \frac{96.0\text{ MHz}}{2.88\text{ MHz/div}} \tag{3.1}$$

The overall range on the oscilloscope capture window was 28.8 MHz. Therefore, the lineshape data was scaled to the range 0 to 28.8 MHz.

Several initial experiments were performed over the 1-200 mTorr regions by fitting the spectral line shapes to a Voigt or a Lorentzian profile at higher pressures. As the curves were fitted to the lineshape at each pressure, the FWHM of each fitted curve was calculated. These were tabulated and then plotted against the pressures. A straight line was fitted to this data. From the line the pressure broadening parameter was calculated. Results of these experiments varied considerably and were in significant disagreement with the published value, typically lower by 10-40%.

Baseline effects were suspected as causing these initial deviations. The baseline is the underlying signal on which the absorption line is sitting on. The baseline can be straight and flat, in which case it presents no problems to the curve fitting software. On the other hand, a baseline can be non-linear due to standing-waves or etalon effects. These make it difficult for the curve fitting software to pick out what signal effects are due to the absorption line and what are due to the baseline. In order to test this suspicion, data was retaken again but this time the apparatus was adjusted to reduce or eliminate the baseline. This was done by adjusting the optics. The lenses could be moved closer to or further from the transmitting and receiving antennas. The orientation of the lenses or antennas could be changed by shifting their angles. The effects on the baseline could be seen on the oscilloscope in situ. Through trial and error using these techniques, the optical train was modified and adjusted so as to minimize, but not totally eliminate, the baseline effects. The data was then retaken from 20 - 200 mTorr in increments of 20 mTorr. The fit analysis resulted in a γ of 23.1 MHz/Torr, 26.9% off from the published value. Study of the results showed that the FWHM versus pressure curve showed a linear relationship from 20 - 140 mTorr. But,

a discontinuity occured between the 140 mTorr and 160 mTorr data points. Initially, we let the Igor Pro software do the fits using its default fit parameters. Among these parameters is the Gaussian line width. In the Igor Pro software, the Gaussian width can be a constant or a variable during the fit. The default is for it to be a variable. After careful study, we came to beleive that the discontinuity seen in the fitted FWHM curve could be a result of the fitting software varying the Gaussian contribution during the fit.

The next step was to refit the lineshape data, this time holding the width parameter constant. This held the Gaussian contribution to the lineshape constant. The physics of this says that the Gaussian contribution, which arises from Doppler broadening, should not change with pressure at these higher pressures, only with temperature and center frequency, see Eq. 2.48. Since $T \simeq 300$ K throughout all of these experiments, a constant Gaussian contribution seemed to be a reasonable assumption. Using Eq. 2.48, the Doppler broadening FWHM was calculated to be

$$\Delta\nu_{FWHM} = (2)3.581 \text{ x } 10^{-7}\sqrt{\frac{297}{18.003}}(620.700 \text{ x } 10^{9}) \text{ Hz } = 1.81 \text{ MHz} \tag{3.2}$$

The Gaussian width was fixed at 1.81 MHz by setting and holding the line shape parameter to 0.920 in the Igor - Multipeak Fitting 2 Package that is part of the Igor Pro software.

The data was then refitted again. The result was a γ of 52.1 MHz/Torr, off from the published value by 65%. Obviously, something was being missed! The values for γ were still far too large.

At this point, the uncertainty of the pressure reading was checked and verified to be $\pm$ 0.25%. The contribution from saturation broadening was also suspected. To investigate saturation broadening, we first looked to the Beer-Lambert formula. From Beer-Lambert we know that each layer of material of equal thickness absorbs an equal fraction of the radiation which passes through it. This results in an exponential decrease in intensity given

by Eq. 2.5. In the THz region, Beer-Lambert can break down due to saturation effects. The intensity of the radiation can be so great that the absorbing molecules cannot get rid of the absorbed energy fast enough. This causes the absorption coefficient α_ν to become independent of I in Eq. 2.5. In fact, a new relationship can be derived [4]

$$\alpha I \approx \frac{n_0}{2t}\frac{h\nu}{kT} \tag{3.3}$$

where n_0 is the number of molecules per unit volume in the ground state, h is the Planck constant, ν is frequency, $1/t$ is the probability per second of a quantum rotational state transition, k is the Boltzmann constant, and T is absolute temperature. Saturation broadening is usually unobservable at high pressures when FWHMs are much greater than 1 MHz. It becomes observable when [4]

$$\frac{16\pi^2|\mu|^2\nu I(2\pi\tau)t}{3ch} \approx 1 \tag{3.4}$$

In order to account for saturation broadening, we rewrite Beer-Lambert as

$$\alpha = -\frac{1}{x}\ln\left(\frac{I_0}{I}\right) \tag{3.5}$$

Since the absorption was not small, the natural log in Eq. 3.5 could not just be expanded. It was necessary to solve the equation outright. To do this we had to know I_0, which was the absolute baseline associated with the power incident on the DC coupled detector. The data was retaken one last time. Measurements were made at 20, 40, 60, 80, 100, 120, 140, 160, 180, and 200 mTorr. Before the lineshapes were fitted, the baselines were isolated and eliminated from each measurement. This was done in Igor Pro as follows: first - a mask was created for each lineshape, second - the lineshape about the resonant frequency was masked out, third - a new baseline curve was fitted across the masked out resonance, and fourth - the original lineshape was divided by the new baseline. This result was the $\frac{I_0}{I}$ ratio

in the Eq. 3.5. To get the absorption, the $\frac{I_0}{I}$ ratio's natural log was taken and the result multiplied by -1 per Eq. 3.5 (x = 1 for unit length). When this was done, the result was fitted to the Voigt profile holding the Gaussian contribution constant as discussed earlier. Thus, Doppler, pressure, and saturation broadening were all now accounted for.

While fitting the data, it was noticed that the baseline was shifting for pressures up to 60 mTorr, but fairly constant for pressures of 80 mTorr and above. This meant that individual baselines were needed for 20, 40, 60, and 80 mTorr. But, all lines measured at pressures of 80 mTorr and above could use the same baseline without significantly affecting the fit results (FWHM). This is what was done in the calculations. The 80 mTorr baseline was used for all pressures $P \geq$ 80 mTorr. An example of the Igor Pro output is shown in Fig. 3.8 for 80 mTorr. Here we see the original curve (lower red, difficult to see below the fitted curve), the fitted curve (lower blue), the baseline (lower green), and the residual difference between the original and the fitted curve (upper red). The top section shows the text output of the fit. Note the fixed Gaussian width (uncertainty = 0), the Lorentzian width, and the FWHM.

The pressure, Lorentzian FWHM, and uncertainties for 620 GHz are given in Table 3.4. Fig. 3.9 shows the FWHM versus pressure curve, the straight line fit, the residual, and the coefficients for the fitted straight line in the format $y = mx + b$. The coefficient m is the slope of the fitted curve which equals the pressure broadening parameter γ, and b is the y-intercept. From Fig. 3.9, the final value for γ was determined to be

$$\gamma = 30.71(1) \text{ MHz/Torr } = 0.7785(3) \text{ cm}^{-1} \text{ atm}^{-1} \tag{3.6}$$

The published value for γ_{FWHM} at 620 GHz is 0.800(3) $\text{cm}^{-1}\text{atm}^{-1}$ by Podobedov et al [39]. A diligent search of the two major molecular spectroscopy journals, the Journal of Molecular Spectroscopy and the Journal of Quantitative Spectroscopy and Radiative

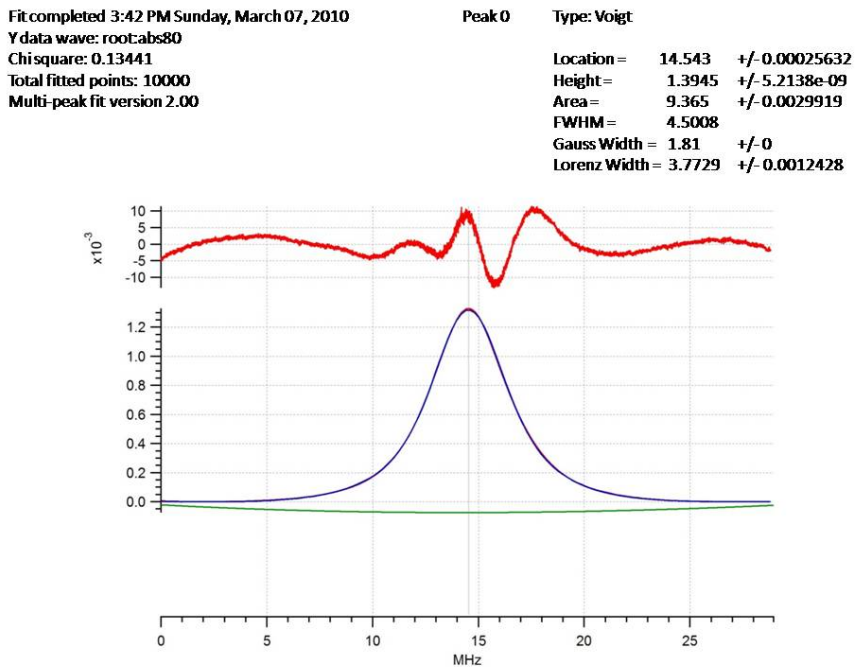

Figure 3.8: Above - curve fitting parameters and results. Below - recorded and fitted absorption line curves, and the residual curve for 620 GHz, 80 mTorr (scale in MHz). Note, vertical scaling on the residual curve is $\approx$ 1/50 of the fitted line.

Pressure (mTorr)	FWHM (MHz)	Uncertainty ($\pm$ MHz)
20	1.8430	0.0021
40	2.5048	0.0027
60	3.0588	0.0031
80	3.7729	0.0012
100	4.3961	0.0013
120	4.9822	0.0015
140	5.6188	0.0017
160	6.1818	0.0020
180	6.8357	0.0022
200	7.3378	0.0025

Table 3.4: Pressure, FWHM, and uncertainty for the 620 GHz fitted curves.

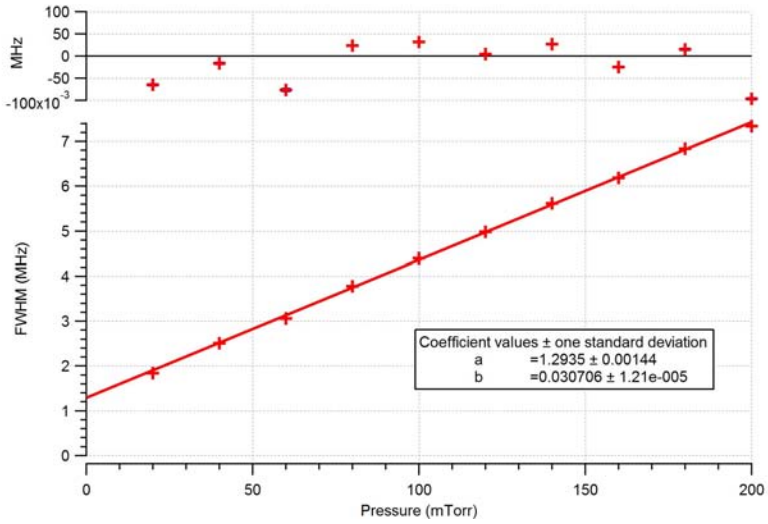

Figure 3.9: FWHM versus pressure for 620 GHz. γ is the calculated slope of the fitted line. The fitted line uses a weighted average fit.

Transfer, was conducted. No published value for γ_{FWHM} for H_2O at 620 GHz newer than Podobedov's was found. Further, a search for papers citing Podobedov's result was conducted. Again, no newer published value for γ was found. Based on this, we believe Podobedov's value to be the most current. Note that 0.800(3) $cm^{-1}atm^{-1}$ in Podobedov's work corresponds to 31.61(12) MHz/Torr. Our value is within 2.69% of this value. There is no overlap between our broadening parameter and that of Pedobedov out to three standard deviations.

Note, the W shape of the residual in Fig. 3.8. This phenomena occurred at every pressure. Also, note the fitted line for FWHM versus pressure has a nonzero y-intercept (1.294 MHz) in Fig. 3.9. This is somewhat unexpected. The first explanation for the non-zero y-intercept was that this could be wall broadening. Wall broadening is further broadening of the lineshape that is caused by the gas molecules in the cell hitting the inner walls of the cell. Wall broadening is usually only seen at low pressures. It becomes an issue when the mean free path between molecular collisions becomes comparable to the shortest dimensions of the cell. A formula for HWHM wall broadening, in kHz, is given by [5]:

$$\Delta\nu = 10\left(\frac{1}{a} + \frac{1}{b} + \frac{1}{c}\right)\sqrt{\frac{T}{M}} \tag{3.7}$$

a and b are the height and width of the cell in cm, c is the length in cm, T is absolute temperature, and M is molecular weight in amu. For most cells a and b are much less than c, so c can be ignored without much loss of accuracy. In other words, only the cell's cross sectional area is important in most calculations. In our gas cell, the cross sectional area was

$$\pi r^2 = \pi(1.0)^2 = \pi \text{ cm}^2 \tag{3.8}$$

So we can let $a = b = \pi$ in Eq. 3.7. The molecular mass M of water vapor is 18.00 amu. At room temperature then, the expected wall broadening FWHM is $\Delta\nu$ = 52 kHz. This is well below the 1.294 MHz seen.

We later came across a journal article by Priem et al [40]. According to Priem, the assumption of the Voigt lineshape is the likely cause of both the W shaped lineshape residuals and the non-zero y-intercept. These phenomena have been seen before and are shown to improve when using a Speed Dependent Galatry Profile which takes into account the speed dependence of relaxation and the molecular confinement [40]. Therefore, the assumption of the Voigt lineshape is the likely cause of both the lineshape residuals and the y-intercept being non-zero.

In summary then, our first experiment looked at the collision broadening of the 620 GHz absorption line for H_2O using frequency domain MMW spectroscopy techniques. Data was collected at pressures varying from 20 - 200 mTorr. The line data for each pressure was fitted with a Voigt curve. During the fits, the baseline (saturation broadening) contribution was eliminated and the Gaussian (Doppler) contribution was held constant. The net results were fitted lineshapes that took into account pressure, Doppler, and saturation broadening effects. The natural line broadening and wall broadening effects were calculated to be negligible. The FWHM value for each fitted curve was calculated. These

FWHM values were plotted against pressure. A weighted average straight line was fitted to the FWHM values. The slope of this line, known as the collision broadening parameter, was calculated and compared to published values. The difference between our experimentally measured value and the published value was 2.69%. This first experiment was an excercise to develop and test experimental and analysis methods. From that standpoint, it was very successfull.

3.5 Frequency Domain Study of the 325 GHz Line

The next part of this work focused on the study of the water vapor absorption line at 325 GHz. The system was modified by replacing the multiplier chain on the VDI transmitter and the detector on the VDI receiver. The multiplier chain was changed from 48x to 24x. This changed the output range from 580 - 655 GHz to 290 - 330 GHz. For the 325 GHz measurements, the detector was changed to a VDI model WR3.4SHM. The WR3.4SHM is a Sub Harmonic Mixer with a rated usable detection range of 220 - 325 GHz. Its minimum mixer noise temperature is at approximately 240 GHz increasing for larger frequencies. Overall, the SHM provided a better response than the ZBD used at 620 GHz. The rest of the system configuration was the same as that for the 620 GHz line as shown in Fig. 3.1.

The settings on the signal generator and oscilloscope are given in tables 3.5 and 3.6.

Modulation	FM
Modulating Waveform	Positive Ramp
Frequency(MHz)	13548.03829167
FM Deviation(MHz)	1.000
FM Rate(kHz)	1.000
Amplitude(dBm)	10.0
FEM Transmitter Output(mW)	2.9

Table 3.5: Signal generator setup for 325 GHz absorption spectroscopy

Note that the peak of the 325 GHz line is less intense then the 620 GHz line. In fact,

Vertical Scale	200 mV/div
Horizontal Scale	40 μs/div
Channel 1	Signal Generator LF output
Channel 2	Preamplifier output
Trigger	CH 1
Coupling	AC

Table 3.6: Oscilloscope setup for 325 GHz absorption line spectroscopy

it is weaker by a factor of about six. However, the output power of the FEM transmitter is four times larger for the 24x multiplier chain than for the 48x multiplier chain. This, and the fact that both the SHM and the ZBD are both more sensitive at 325 GHz than at 620 GHZ gave us confidence that we would be able to measure and work with this transition line.

The methods used for collecting and analyzing the data and fitting the absorption line curves were the same as that used in the 620 GHz absorption line analysis. Igor Pro was used for the curve fitting. During the curve fitting process, the lineshape data again had to be rescaled to reflect the fact that the ordinate (x-coordinate) was actually frequency not time. The frequency calibration method used was the same as that used for the 620 GHz analysis. The lineshape data was rescaled to the range 0 to 19.2 MHz. Again Voigt profiles were used in the fits. The baselines were removed in the same manner as in the 620 GHz analysis. The Doppler (Gaussian) contributions were held constant at 0.946 MHz per Eq. 3.2, which corresponded to a fitting width parameter of 1.76 in the Igor - Multipeak Fitting 2 Package. The data was taken with the oscilloscope AC coupled. This is due to the fact that with DC coupling, the absorption dip was so small that in order to see it, the magnification had to be set so high as to move the DC baseline off the oscilloscope screen. Because of the AC offset, the raw data was offset by +200 mV in Igor Pro before fitting to ensure all the data points were above zero. This step was necessary for the masking and fitting of the baseline. It also required us to modify the fitting procedure later on.

For 325 GHz, we only wanted to verify the frequency domain data with the published values. Therefore, data was not taken over as large a range of pressures as was done in the

620 GHz study. The pressures at which the 325 GHz absorption line was measured were: 1, 10, 20, and 40 mTorr. The fitted curves for all of these pressures are shown in Fig. 3.10. Note the affect of pressure on the curves. The fit results for 20 mTorr are shown in Fig. 3.11.

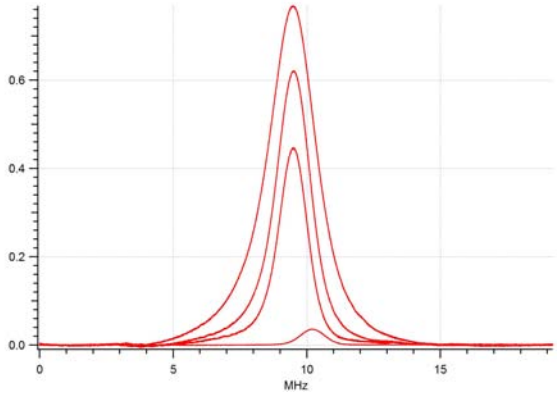

Figure 3.10: Fitted curves for the 325 GHz absorption line of water vapor at 1, 10, 20, and 40 mTorr. The intensity and width of the curves increases with pressure.

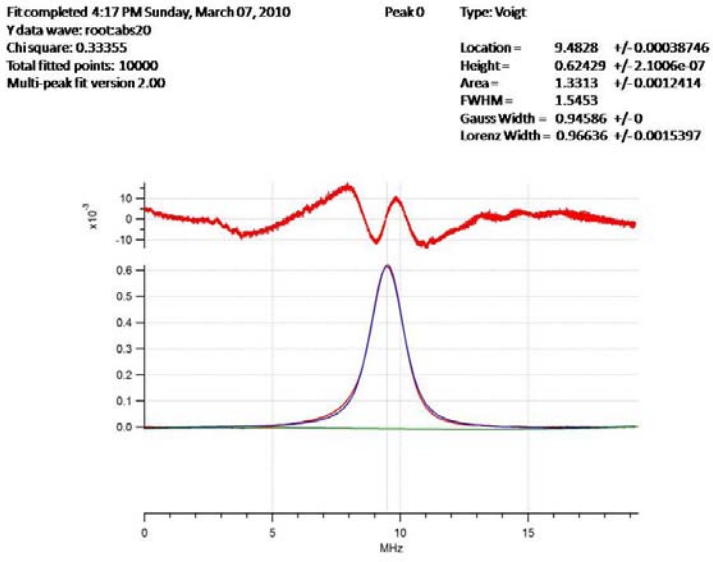

Figure 3.11: Above - curve fitting parameters and results. Below - recorded and fitted absorption line curves at 325 GHz, 20 mTorr.

The pressure, Lorentzian FWHM, and uncertainties for 325 GHz are given in Table 3.7. The calculated FWHM values for all pressures were plotted against pressure. A

weighted average straight line fit was done. The residuals were plotted and the slope of the fitted curve, the pressure broadening parameter γ, was calculated. See Fig. 3.12.

Pressure (mTorr)	FWHM (MHz)	Uncertainty ($\pm$ MHz)
1	0.2036	0.0011
10	0.5760	0.0014
20	0.9664	0.0015
40	1.7422	0.0018

Table 3.7: Pressure, FWHM, and uncertainty for the 325 GHz fitted curves. Original data.

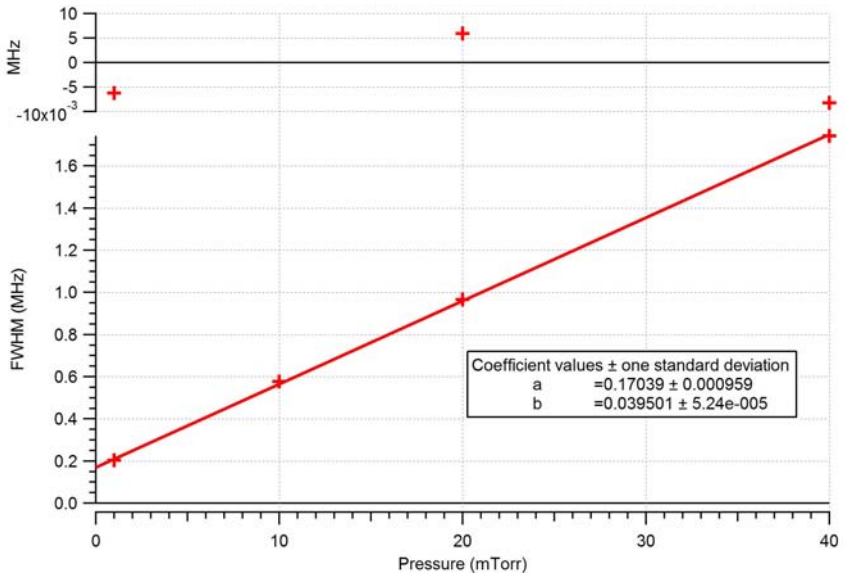

Figure 3.12: FWHM versus pressure for 325 GHz. γ is the calculated slope of the fitted line. The fitted line uses a weighted average fit. Original data.

From Fig. 3.12, γ = 39.50(5) MHz/Torr for FWHM. The HWHM value published by Koshelev et al. in 2007 is 18.51(3) MHz/Torr [41]. This corresponds to a FWHM γ of 37.02(6) MHz/Torr. A diligent search of the two major molecular spectroscopy journals, the Journal of Molecular Spectroscopy and the Journal of Quantitative Spectroscopy and Radiative Transfer, was conducted. No published value for γ for H_2O at 325 GHz newer than Koshelev's was found. Further, a search for papers citing Koshelev's result was conducted. Again, no newer published value for γ was found. Based on this, we believe

Koshelev's value to be the most current. Our value was 6.70% greater than Koshelev's value.

A second round of data was taken at the 325 GHz line on a different day. In this second experiment, line widths were measured at 10, 100, and 150 mTorr. This data was then fitted using Voigt curves like the earlier data resulting in FWHM values. The pressure broadening parameter was then calculated from the FWHM values. The pressure broadening parameter calculated from the second day data did not match the earlier pressure broadening parameter nor did it match the published value. In fact it was off by quite a bit from the published value. We later refit the second day data by modifying the fitting procedures. Instead of using the 100 and 150 mTorr absorption curves to calculate FWHM, the transmitted curves (the 10 mTorr absorption curve was still used) were used. This resulted in a pressure broadening parameter that was in much better agreement with the published value. The second day data refit with the modified fitting procedure is shown in Table. 3.8. A plot and calculation of the pressure broadening parameter is shown in Fig. 3.13. From Fig. 3.13, γ = 36.85(1) MHz/Torr for FWHM. This value is 4.59% less than Koshelev's value.

Pressure (mTorr)	FWHM (MHz)	Uncertainty ($\pm$ MHz)
10	0.3864	0.0009
100	3.5398	0.0009
150	5.6807	0.0013

Table 3.8: Pressure, FWHM, and uncertainty for the 325 GHz fitted curves, 100 and 150 mTorr FWHM values calculated from the transmitted line width.

The reason for the use of the transmitted line width rather than the absorption line width has to do with the AC coupling of the measured signal. To get the absorption line we took the natural log of the transmitted line. This final step of the fitting process is only necessary for saturation or near saturation conditions as was the case with the 620 GHz data. The 620 GHz line is very strong with significant absorption. When measuring the

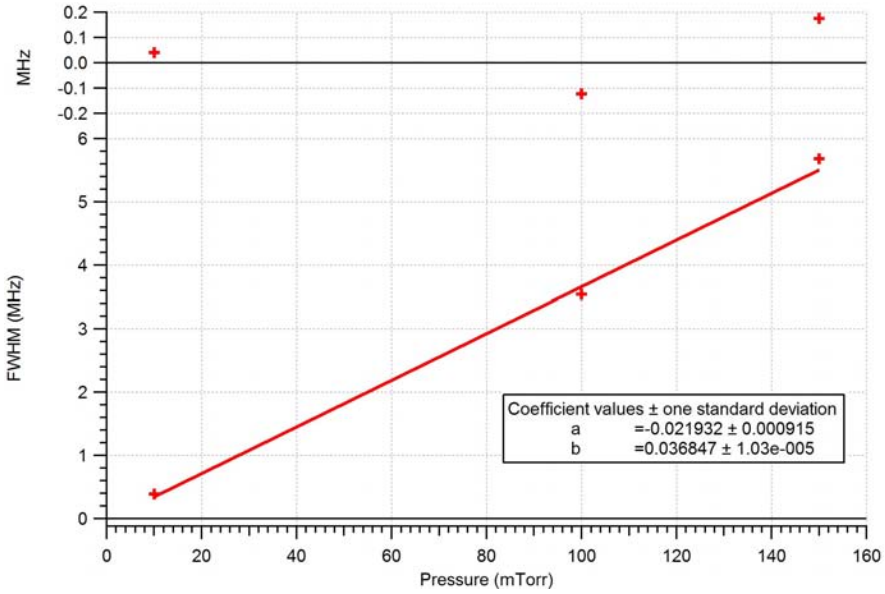

Figure 3.13: FWHM versus pressure for 325 GHz, 100 and 150 mTorr FWHM values calculated from the transmitted line width. γ is the calculated slope of the fitted line. The fitted line uses a weighted average fit.

620 line, DC coupling could easily be used because the absorption was so strong. With DC coupling, we got an absolute voltage that corresponded to a power or intensity level. The 325 GHz line is less intense. When measuring it, AC coupling had to be used. This implies that we were nowhere near saturation as the absorption was weaker. Because we AC coupled the 325 GHz data, the final step of taking the natural log was unnecessary and it did not work, particularly at the higher pressures (100 and 150 mTorr).

Finally, we combined all of the data in Tables 3.7 (except the 1 mTorr data point) and 3.8 and calculated one final pressure broadening parameter. This is shown in Fig 3.14. The 1 mTorr data point was deleted because of the uncertainty of its value and the fact that 1 mTorr really only represents the Doppler broadening regime.

From Fig. 3.14, γ = 37.41(1) MHz/Torr for FWHM. This value is 1.05% less than Koshelev's value. There is no overlap between our broadening parameter and that of Koshelev out to three standard deviations.

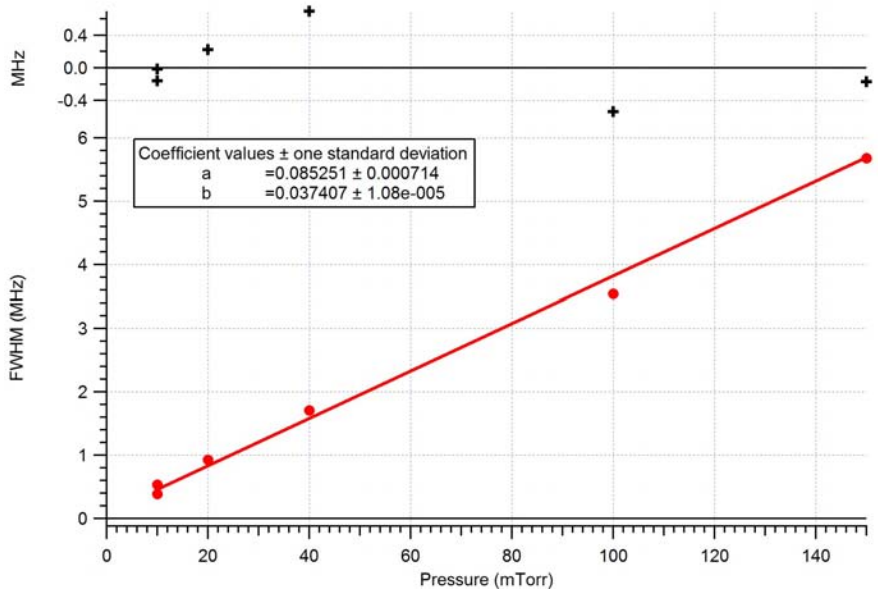

Figure 3.14: FWHM versus pressure for the 325 GHz line using all data points. γ is the calculated slope of the fitted line. The fitted line uses a weighted average fit.

Transient (Time Domain) Experiments

More recently, so called time domain or transient techniques have been developed to study the absorption lines of gas phase molecules including water vapor. For water vapor, these studies were primarily done on the 22 GHz absorption line using a technique called frequency switching [42] [11] [43]. A search of the literature did not find any time domain studies on either the 325 GHz or the 620 GHz absorption lines of water vapor.

The transient experiments in this study involved measurements using coherent transient spectroscopic methods. The transient (or time domain) techniques attempted include: frequency switching (a.k.a. free induction decay), the π-τ-$\frac{\pi}{2}$ pulse sequence (a.k.a. rotary echo) method, and the fast passage method. The specific techniques used for each of these methods will be explained in detail below.

4.1 The Theory of Coherent Spontaneous Radiation and Transient Microwave Spectroscopy

A new technique for studying the absorption characteristics of molecules in the MMW region is transient, or time domain spectroscopy. The purpose of time domain spectroscopy is to directly observe and study molecular relaxation processes. These relaxation processes are often called non-stationary processes because they are transient as opposed to steady-state. Observation of transient processes is not possible with steady state absorption spec-

troscopy [42]. Transient processes, or effects, occur when coherent radiation that is incident on a two level quantum system is swept through resonance in a time much shorter than the relaxation time of the system [9]. This causes the system to change its equilibrium state to a new equilibrium state and then relax back again to the original. As this processes occurs, the molecular relaxation times, T_1 and T_2 can be directly observed and measured. T_1 and T_2 correspond to the longitudinal (a.k.a. the population or the energy) relaxation and the transverse (a.k.a. the polarization or the coherence) relaxation times respectively [44].

4.1.1 The Optical Bloch Equations

The transient response of a two state molecular system can be described using a set of three, coupled, ordinary differential equations called the Optical Bloch Equations. The Optical Bloch Equations have been adapted from and are analogous to the Bloch Equations used to described the motion of magnetization vector $\overleftarrow{M}$ in electron paramagnetic and nuclear magnetic resonance spectroscopy. We will review the Magnetic Bloch Equations briefly to set the stage for the Optical Bloch Equations. Mathematically, when a magnetic field $\overleftarrow{B}$ is applied to a magnetic material with magnetization vector $\overleftarrow{M}$, the magnetization vector moves according to [45]

$$\frac{d\overleftarrow{M}}{dt} = -\gamma \overleftarrow{M} \times \overleftarrow{B} \tag{4.1}$$

This is identical to the equation for the motion for a spinning top or gyroscope when a torque is exerted by gravity. In Eq. 4.1, γ is the gyromagnetic ratio, the ratio of the angular momentum to the magnetic moment. The solution is just the precession of $\overleftarrow{M}$ about $\overleftarrow{B}$ at the Larmor frequency

$$\omega_0 = -\gamma B_0 \tag{4.2}$$

In EPR and NMR, the field $\overleftarrow{B}$ is composed of two parts. The first part is a large static component $B_0\hat{k}$. The coordinate system for such a problem is set up so that the magnetic field static component is in the positive z direction. Therefore $B_0\hat{k}$ is the longitudinal component of $\overleftarrow{B}$. The second part is a time varying component $\overleftarrow{b}$ orthogonal to $B_0\hat{k}$. Magnetic field vector $\overleftarrow{b}$ is the transverse component of $\overleftarrow{B}$ and is in the xy plane.

However, the preceding description is incomplete. When the magnetic dipoles align themselves with the magnetic field, energy is lost. In order to have energy conserved, some coupling mechanism must be present. The coupling effect is added to Eq. 4.1 as follows [45]

$$\frac{dm_{x,y}}{dt} = -\gamma\overleftarrow{M} \times \overleftarrow{B}_{x,y} - \frac{m_{x,y}}{\tau_2} \tag{4.3}$$

$$\frac{dM_z}{dt} = -\gamma\overleftarrow{M} \times \overleftarrow{B}_z - \frac{M_z - M_0}{\tau_1} \tag{4.4}$$

These are known as the Bloch equations. In this work they will be referred to as the Magnetic Bloch Equations. They are the equations of motion for the magnetization vector $\overleftarrow{M}$ in a magnetic field $\overleftarrow{B}$. M_z is the "longitudinal" component of the magnetization vector $\overleftarrow{M}$ and m_x and m_y are the "transverse" components of the time varying magnetization vector $\overleftarrow{m}$. $\overleftarrow{m}$ is in a plane perpendicular to the constant component of the magnetic field $\overleftarrow{B}$. τ_1 and τ_2 are the longitudinal and transverse relaxation times respectively. When broken down into component form the Magnetic Bloch Equations become [45]

$$\frac{dm_x}{dt} = -\gamma(M \times B)_x - \frac{m_x}{\tau_2} \tag{4.5}$$

$$\frac{dm_y}{dt} = -\gamma(M \times B)_y - \frac{m_y}{\tau_2} \tag{4.6}$$

$$\frac{dM_z}{dt} = -\gamma(M \times B)_z - \frac{M_z - M_0}{\tau_1} \tag{4.7}$$

Coherent optical spectroscopy is the optical analogue of magnetic resonance spectroscopy [44]. In this case we have a quantum two level system, a molecule, being illuminated by time varying EM radiation given by

$$E = 2\mathcal{E}\cos(\omega t - kz) \tag{4.8}$$

Instead of describing the motion of a magnetization vector $\overleftarrow{M}$, the Optical Bloch Equations describe the motion of a psuedospin vector which has transverse components representing the real and imaginary parts of a complex polarization and a longitudinal component representing the population difference between the two energy levels. The Optical Bloch Equations in component form are [9]

$$\frac{dP_r}{dt} + \Delta\omega P_i + \frac{P_r}{T_2} = 0 \tag{4.9}$$

$$\frac{dP_i}{dt} - \Delta\omega P_r + \kappa^2\mathcal{E}\left(\frac{\hbar\Delta N}{4}\right) + \frac{P_i}{T_2} = 0 \tag{4.10}$$

$$\frac{d}{dt}\left(\frac{\hbar\Delta N}{4}\right) - \mathcal{E}P_i + \frac{\hbar}{4}\left(\frac{\Delta N - \Delta N_0}{T_1}\right) = 0 \tag{4.11}$$

where P_r and P_i are the real and imaginary parts of the polarization, $\Delta\omega = \omega_0 - \omega$ (ω_0 is the resonant or transition frequency), $\kappa = \frac{2}{\hbar}|\langle a|\mu|b\rangle|$ (μ is the transition matrix dipole moment; a and b denote the lower and upper energy states respectively), $\mathcal{E}$ is the amplitude of the electric field component of the incident radiation, ΔN_0 is the equilibrium value of the population difference, ΔN is the instantaneous population difference, and T_1 and T_2 are the population and polarization relaxation times respectively.

If we let $n = \frac{\hbar \Delta N}{4}$ and $n_0 = \frac{\hbar \Delta N_0}{4}$, as done by Brailovsky et al. [46] we simplify the Optical Bloch Equations into

$$\frac{dP_r}{dt} + \Delta\omega P_i + \frac{P_r}{T_2} = 0 \tag{4.12}$$

$$\frac{dP_i}{dt} - \Delta\omega P_r + \kappa^2 \mathcal{E} n + \frac{P_i}{T_2} = 0 \tag{4.13}$$

$$\frac{dn}{dt} - \mathcal{E} P_i + \left(\frac{n - n_0}{T_1} \right) = 0 \tag{4.14}$$

Eq. 4.12 and Eq. 4.13 are analogous to Eq. 4.5 and Eq. 4.6. The relaxation time, T_2, in Eq. 4.12 and Eq. 4.13 is often referred to as the transverse relaxation time as it appears in the same place in the Optical Bloch Equations as τ_2 does in the Magnetic Bloch Equations and is treated the same mathematically. Eq. 4.14 is analogous to Eq. 4.7. In this case, the "motion" being described is the change in population difference between two quantum states instead of the motion of a longitudinal magnetization vector. The relaxation time, T_1, in Eq. 4.14 is often referred to as the longitudinal relaxation time as it appears in the same place in the Optical Bloch Equations as τ_1 does in the Magnetic Bloch Equations and again is treated the same mathematically.

4.1.2 Relaxation times

Using continuous wave time domain spectroscopy techniques, the polarization and population relaxation times can be measured directly. In a quantum two level molecular system in thermal equilibrium, there will usually be molecules populating both states, the higher and the lower, due to thermal excitations. How each energy level is populated will be described by a Boltzmann distribution. The original equilibrium population difference is the difference between the number of molecules in the two states when no resonant radiation

is incident on the system. When resonant radiation is incident on the system many more molecules become excited and populate the higher energy state at the expense of the population of the lower energy state. This causes a change in the population distribution of the system. A new equilibrium population difference is created. The population relaxation time, T_1, is the time it takes for the new population difference at the excited state to decay or relax back to the original population difference after the exciting radiation is removed. Further, when radiation is incident on the molecules, their electric dipole moments tend to align with the polarization of the radiation. The radiation will put the molecules in phase. The polarization relaxation time, T_2, is the time it takes for the aligned molecules to lose their coherence (dephase) after the exciting radiation is removed. In this process, the molecules emit coherent spontaneous radiation at the molecular resonant frequency. As the incident radiation moves off resonance, the emitted radiation is mixed with the incident radiation (now off resonance). What is seen at the detector is a beat frequency which is the difference between the emitted and incident radiation [9].

4.1.3 Analytical Solutions to the Optical Bloch Equations

Closed form solutions to the Optical Bloch Equations are possible only under special conditions. Different solutions exist for the cases of transient absorption and transient emission [47]. Wolf [9], McGurk [48], and Mäder [49] all derive analytical solutions to the Optical Bloch Equations for fast passage type processes. In these derivations the assumption is made that the output power from the source is very low and that the sweep time is very fast relative to relaxation times. Because of these assumptions, the approximation is made that the population difference across the sweep is almost unchanged from the equilibrium level, in other words $\Delta N \approx \Delta N_0$. This assumption sets the third Optical Bloch Equation equal to zero. From there, these authors develop closed form solutions for the polarization as a function of time. Wolf [9] tests this approximation across the fast sweep and fast passage regimes. In his paper, Wolf calculates the analytical solution to the Optical

Bloch Equations (OBE) using $\Delta N \approx \Delta N_0$. Wolf's closed form solution is [9]

$$\hat{P}(\Delta\omega_f) = \frac{\kappa^2 \mathcal{E} \hbar \Delta N_0}{\sqrt{\alpha}} \frac{\sqrt{\pi}}{4\sqrt{2}} (-1)^{\frac{1}{4}} \exp\left[-\frac{\Delta\omega_f}{\alpha T_2}\right] \times \exp\left[-\frac{i}{2\alpha}\left(\frac{1}{T_2^2} - \Delta\omega_f^2\right)\right] \times [\text{erf}(t_f) - \text{erf}(t_i)] \quad (4.15)$$

where α is the sweep speed given by

$$\alpha = \frac{d(\Delta\omega)}{dt} \quad (4.16)$$

the complex error function is

$$\text{erf}(x) = \int_0^x e^{-t^2} dt \quad (4.17)$$

x being a complex number, the substitution

$$t(\Delta\omega) = -\frac{(-1)^{\frac{1}{4}}}{\sqrt{2\alpha}}\left(\Delta\omega + \frac{i}{T_2}\right) \quad (4.18)$$

is made and finally $t(\Delta\omega_f)$ and $t(\Delta\omega_i)$ are written instead of t_f and t_i respectively.

The resultant equation, Eq. 4.15, consists of harmonic components which are exponentially damped in time as the resonant absorption frequency is passed. The frequency of the oscillation is a function of the frequency difference between the resonant frequency of the molecules and the incident radiation. The decay constant is a function of the polarization relaxation time.

Wolf also calculates a numerical solution to the OBE without the $\Delta N \approx \Delta N_0$ assumption. He then plots the behavior of amplitude of the imaginary part of the polarization, P_i, versus the sweep rate, α (P_i corresponds to absorption). The plots of the analytical and numerical solutions agree only in the region where the sweep rate is very fast as seen in

Fig. 4.1.

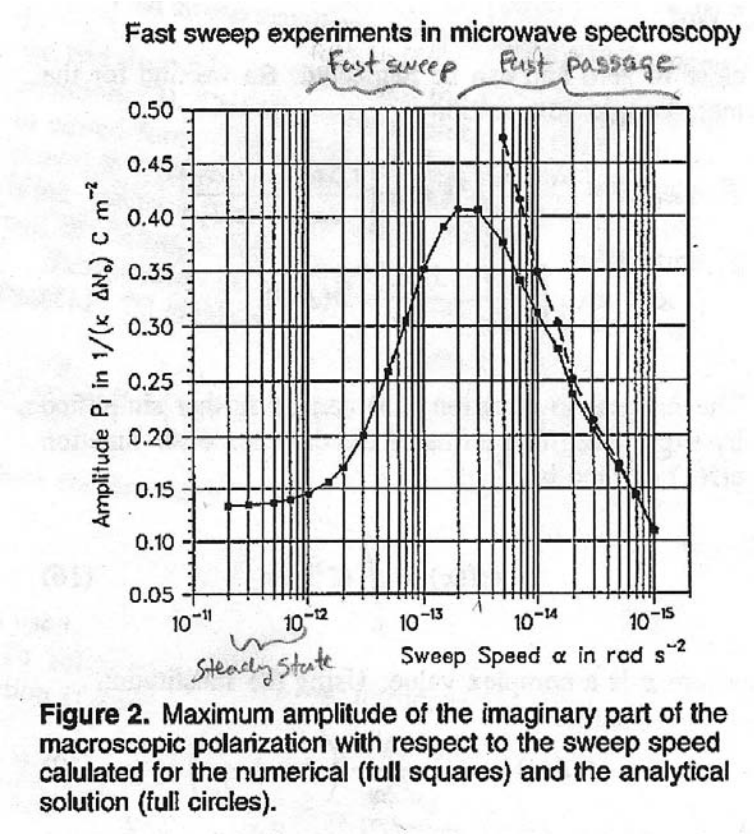

Figure 4.1: Amplitude of P_i versus α. From Wolf [9]. Note that there are typos in the horizontal axis units. The signs in the exponents should be positive not negative as shown.

Wolf divides the curve in Fig. 4.1 into three regimes. The steady state regime, where the amplitude of P_i is pretty much independent of α. This regime corresponds to frequency domain spectroscopy which was discussed in the previous chapter. The fast sweep regime, where the amplitude of P_i increases with increasing α. Finally, the fast passage regime, where the amplitude of P_i decreases with increasing α. The fast sweep and fast passage regimes correspond to the transient spectroscopy experiments discussed in this chapter.

The Wolf study implies that the $\Delta N \approx \Delta N_0$ assumption is not valid in the fast sweep regime. It is only valid in the fast passage regime. Therefore, there is no known closed form (analytical) solution to the Optical Bloch Equations in the fast sweep regime.

4.2 Time Domain Studies of the 620 GHz Line

The next set of experiments focused on the study of the time domain aspects of absorption physics. The aim was to roughly follow the experimental procedure described by Kasuga, Kano, and Shimizu [11]. In this experiment, Kasuga et al. used the rotary echo and free induction frequency switching methods to determine the population and polarization relaxation times T_1 and T_2. The rotary echo method was used to measure a composite relaxation constant called T_{eff}, the effective relaxation time. T_{eff} is given by [11]

$$\frac{1}{T_{eff}} = \left[\left(\frac{1}{T_2}\right)^2 + \frac{T_1}{T_2}\left(\frac{\mu E}{h}\right)^2\right]^{\frac{1}{2}} \tag{4.19}$$

In an early paper, Kasuga, Kuze, and Shimizu reported the measurement of T_2 using the free induction frequency switching method [42]. Given T_{eff}, T_2, and Eq. 4.19, the longitudinal relaxation time T_1 was calculated by these authors.

4.2.1 Frequency Switching

Excellent descriptions of the free induction or frequency switching method of transient microwave spectroscopy are given by Kasuga et al. [42], Amano and Shimizu [10], and Tanaka et al [50].

In this method, the frequency of the radiation is modulated by applying a square wave to the radiation source. The square wave switches the radiation between two frequencies. One frequency is the resonant frequency of the absorption line being studied. The other frequency is an off resonance frequency. How far off of resonance the frequency is modulated depends on what is being studied in the experiment but the minimum is usually considered to be 1 FWHM. Usually the off resonance frequency is several MHz away from resonance. The rate of modulation (the frequency of the square wave) is usually in the kHz range so its period is $\gg T_2$ and the IF (Intermediate Frequency) is $> 1/T_2$ (so several oscillations can be observed). The transient effect on the absorption signal is seen when

the square wave transitions from on to off resonance. In response to the on to off resonance transition, the absorption signal exhibits a damped oscillation with a decay constant of T_2. The figure below gives some specific examples of the transient response of the absorption signal to the on to off resonance transition. This figure was taken directly from Amano and Shimizu [10] and show the response of ammonia, NH_3. Note that Amano's caption calls the response a transient nutation, this seems incorrect. A nutation occurs during a transient absorption process (transition from off resonance to on) and is used to measure T_{eff}. Frequency switching (a.k.a. Free Induction Decay), which measure T_2, involves transient emission (transition from on resonance to off). [47].

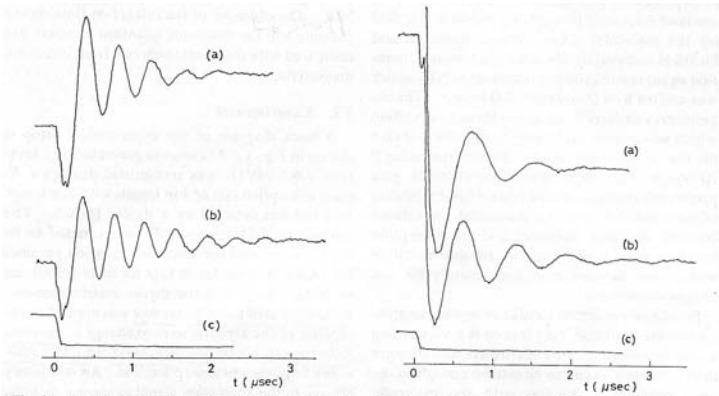

Fig. 2. Transient nutation of the $J=2$, $K=1$ inversion transition of NH_3. (a) p (pressure of NH_3)= 23 mTorr; (b) $p=13$ mTorr; (c) pulse shape applied to the repellor of the klystron.

Fig. 3. Transient nutation of the $J=5$, $K=4$ inversion transition of NH_3. (a) $p=20$ mTorr; (b) $p=$ 12 mTorr; (c) pulse shape applied to the repellor of the klystron.

Figure 4.2: Transient response of NH_3 to the on to off resonance transition during frequency switching. From Amano and Shimizu [10].

The responses on the left, labeled Fig. 2., and on the right, labeled Fig. 3. are for two different NH_3 transitions. The upper and lower responses are at different pressures.

In our experiment, the Agilent E8254A signal generator was set to to the parameters similar to those given in the Table 3.2. The modulation rate and depth parameters were varied over a large continuous range in the attempt to get a good looking transient response.

A transient response was eventually seen but the results of this experiment were perplexing. A decaying oscillation was seen but on the rising edge of the square wave not the

falling edge. The rising edge of the modulating square wave corresponded to the off to on resonance transition, not the on to off transition as expected. This behavior corresponds more to transient nutation rather than free induction decay. Further, the frequency of the oscillation was not constant. It appeared to contain multiple frequency components. Several parameters in the experiment were varied including: the power of the THz radiation, the modulation rate, the modulation depth, the position of the gas cell relative to the optics, and finally the pressure. In each case there was no change to the shape or oscillation frequencies of the response. The fact that the absorption signal response was independent of power, rate, depth, and especially pressure and that this damped oscillatory response was only seen on the off to on resonance transition indicated that this was not the free induction decay response that we were looking for. The suspicion was that what was being seen were transient effects of the equipment itself.

4.2.2 Rotary Echo

The rotary echo method is described in detail in papers by Kasuga et al. [11], Schwendeman [51], and Mäder et al [52]. The rotary echo method is part of a larger, more complex technique called the π-τ-$\frac{\pi}{2}$ pulse sequence technique. The π-τ-$\frac{\pi}{2}$ pulse sequence is essentially the same as that used in NRM spectroscopy and has been called the electric dipole analog of NMR [52].

Rotary echo is somewhat similar to frequency switching. However, instead of using a square wave with a 50% duty cycle to modulate the frequency of the THz radiation, a special pulse sequence is used to transition on and off of resonance. Fig. 4.3 (taken directly from Kasuga [11]) shows the pulse sequence used and the absorption signal response.

The absorption signal response is called a rotary echo, or nutation signal. The critical parameters to this technique are the spacing and widths of the pulses. At $t = 0$, the driving radiation is on resonance and stays that way for a period of time T. At $t = T$, the radiation

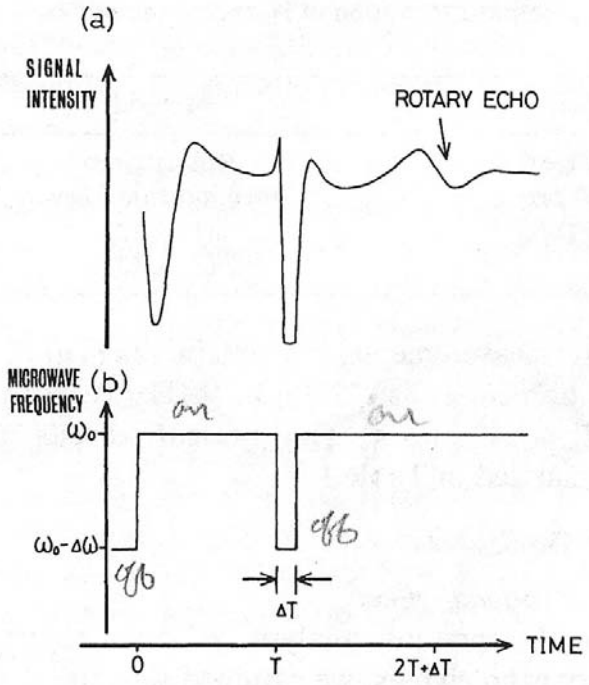

Fig. 2. Rotary echo signal (a) and pulse sequence of frequency switching (b). A short square pulse with width ΔT and amplitude $\Delta\omega$ applied at $t=T$ causes a phase shift of π. The echo nutation appears before $t=2T+\Delta T$ as the dipoles rephase and the macroscopic polarization becomes appreciable.

Figure 4.3: Frequency modulating pulse sequence and transient response of the absorption signal in the rotary echo method. From Kasuga [11]

is taken off resonance by a short pulse of depth $\Delta\omega$ and of width ΔT. At $t = T + \Delta T$, the pulse is removed and the driving radiation is back on resonance. During this frequency pulse transition, a phase shift occurs between the induced dipoles in the molecules and the driving radiation. This phase shift is given by

$$\Delta\phi = \Delta\omega \cdot \Delta\mathrm{T} \tag{4.20}$$

When

$$\Delta\phi = (2n + 1)\pi \tag{4.21}$$

is satisfied, the individual dipoles rephase at $t = 2T + \Delta T$ and the rotary echo transient appears as shown in Fig. 4.3. Based upon Eq. 4.21, the modulating pulse is a π pulse. For H_2O, the rotary echo transient is seen when $\Delta\phi$ = π, 3π, 5π ..., but not when $\Delta\phi$ = 2π, 4π, 6π...; this agrees with Eq. 4.21 and is shown in Fig. 4.4 also taken directly from Kasuga [11]). Rotary echo measurements are made by measuring the amplitude of the echo for various values of t by varying ΔT such that $\Delta\phi$ = π, 3π, 5π et. The amplitudes of the measured echoes are then plotted against t resulting in a line. The slope of that line gives the effective relaxation rate constant T_{eff}.

In this thesis, an attempt was made to use the rotary echo method on the 620 GHz H_2O absorption line to measure T_{eff}. However, the Agilent E8254A signal generator is not an arbitrary wave generator (AWG) and so could not create the pulse sequences desired. An Agilent 33220A AWG was available and therefore was used to replace the internal function generator in the E8254A. However, after connecting the AWG, it was soon determined that it too would not be able to generate the desired pulse sequence. This points to possible future work. If an adequate AWG can be procured, the rotary echo experiment could be performed. The data collected would be invaluable as a search of the literature did not reveal that this technique has been used on the H_2O 325 or 620 GHz absorption lines.

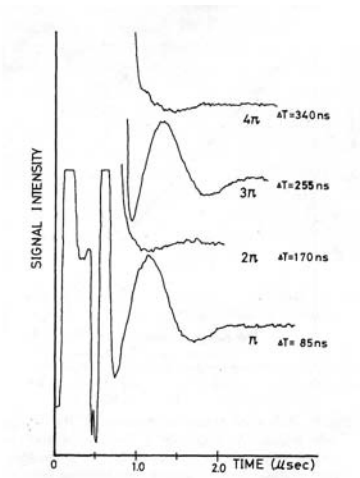

Fig. 3. Rotary echo signals of the $6_{16} \leftarrow 5_{23}$ transition of H_2O. When the phase shifts are π and 3π, the nutation echo signals are observed. When phase shifts of 2π and 4π are given, no echoes are observed.

Figure 4.4: Rotary echo transient signals for n = 1, 2, 3, and 4 in $\Delta\phi = (2n + 1)\pi$. Note, only n = odd produces the desired transient. Note also, the $6_{16} \leftarrow 5_{23}$ transition corresponds to the H_2O absorption line at 22 GHz. From Kasuga [11].

At this point in the project, it was determined that the best course of action would be to return to the frequency switching method. The objective here was to try to determine if the transient effects seen earlier were in fact instrumentation effects.

4.2.3 Analysis of the VDI WR1.5ZBD Detector Bandwidth

The WR1.5ZBD consists of a diode detector and waveguide that couples the radiation captured by the receiving horn antenna. In this portion of the study, the bandwidth of the VDI WR1.5ZBD was examined. There are two types of detector bandwidths. There are the optical and the electronic or video bandwidths. The optical bandwidth is the bandwidth over which the detector is sensitive to electromagnetic radiation. The VDI model WR1.5ZBD detects radiation in the 500 - 750 GHz frequency range. Therefore, it has an optical bandwidth of 150 GHz. This is 150/625 = 25% of the center band frequency and is considered to be very good. The video bandwidth is defined as the fastest change in the signal the detector can sense. The video bandwidth limits the fastest transistions that can be detected.

It is the video bandwidth of the WR1.5ZBD that was called into question in this study and what was examined.

The ringdown associated with T_1 and T_2 should be in the low μs range as this was the range reported in the literature for the 22 GHz H_2O line [11]. According to the theory, the ringdown at 22 GHz should not be all that different from that at 620 GHz. This is because the decay constant is determined by the relaxation constants which are themselves functions of pressure not frequency.

The ringdown was not seen on the oscilloscope using the frequency switching technique on the 620 GHz absorption line. Therefore, a small study was undertaken to determine if the video bandwidth of the VDI WR1.5ZBD detector was the limiting factor. The idea behind this test was to frequency tune the system to be on the edge of the absorption line and use the 1f (first derivative) detection capabilities of a lock-in amplifier to determine the highest intermediate frequency we could see. The Agilent 33220A AWG was used to drive a reference input signal to the Agilent E8254A signal generator which then drove the VDI transmitter. The Agilent AWG also drove an SRS SR844 RF lock-in amplifier reference input, and the Tektronix DPO3014 oscilloscope (although as it turned out we did not need the oscilloscope, we just looked at the magnitude of the signal as a DC level, i.e. a number on the RF Lock in). The RF lock-in amplifier was used to test the detector response. A schematic of this experimental setup is shown below in Fig. 4.5.

The AWG was used to generate a reference signal. The E8254A signal generator was set to FM, with a modulation depth of 40 kHz as this depth was found to maximize output. The modulation rate was initially set to 30 kHz. The noise and detector output voltages were then measured and the S/N ratio calculated and recorded. The modulation rate was then incrementally increased and the S/N ratio measured, calculated, and recorded at each FM rate. Table 4.1 shows the results; Fig. 4.6 shows the behavior graphically.

As can be seen, the detector video response is not flat across the 5 MHz bandwidth but

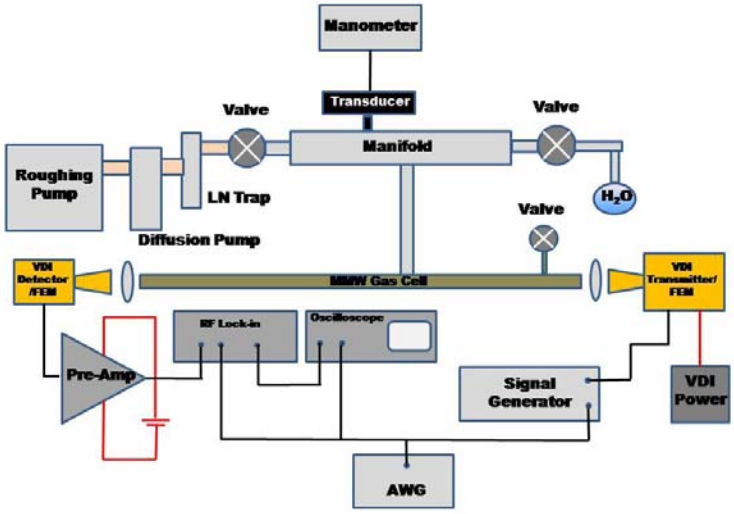

Figure 4.5: Block diagram of the experimental setup for the measurement of the MMW signal detector.

FM Rate	S/N
30 kHz	35 dB
100 kHz	33 dB
200 kHz	31 dB
500 kHz	25 dB
5 MHz	0 dB

Table 4.1: S/N at various modulation rates at modulation depth of 40 kHz

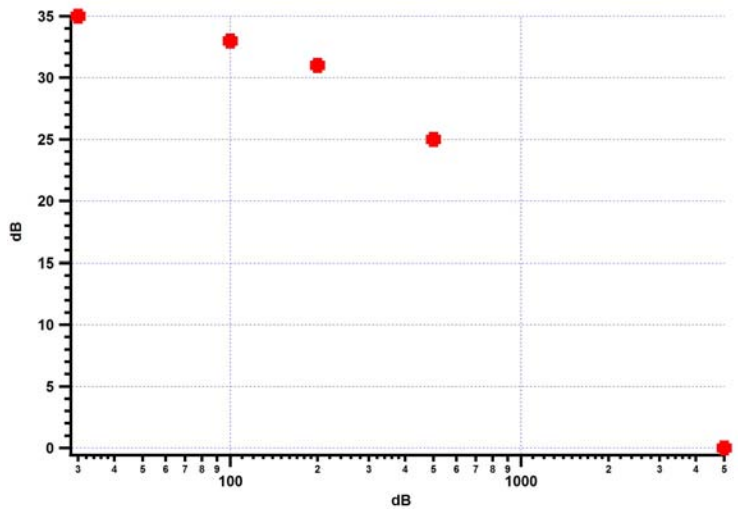

Figure 4.6: S/N versus FM rate at the 620 GHz absorption line.

rolls off. It appears that the S/N rolls off at a rate of about 12 dB/decade beyond 30 kHz. The - 3dB point is at approximately 150 kHz. This corresponds to a transient ringdown of approximately 6 μs. The conclusion is that the VDI WR1.5ZBD detector cannot measure transient effects with time constants below 6 μs.

4.3 Time Domain Study of the 325 GHz Line

Despite the fact that the video bandwidth of the VDI WR1.5ZBD was insufficient to measure the transient effects, the video bandwidth of the VDI WR3.4SHM was sufficient. Since this SHM was for use with a frequency range that included 325 GHz but not 620, the next step in this work was the study of the time domain responses of the 325 GHz absorption line. Frequency switching, also known as free induction decay, and fast passage measurements were attempted.

4.3.1 Frequency Switching

In this experiment, the Agilent E8254A signal generator was initially set to the parameters given in the table below:

Modulation	FM
Modulating Waveform	Square Wave
Frequency(MHz)	13547.03829167
FM Deviation(MHz)	1.000
FM Rate(kHz)	10.000
Amplitude(dBm)	10.0
FEM Transmitter Output(mW)	2.9

Table 4.2: Signal generator setup for 325 GHz transient spectroscopy using frequency switching

Note that the modulation depth set to 1.000 MHz and that the center frequency was set to be 1.000 MHz below the resonant frequency. This arrangement caused the modulated

frequency to be on resonance when the square wave was high and off resonance when the square wave was low. Note also that with the 24x multiplier chain in use, the actual frequency jump was 24 x 2 MHz or 48 MHz. This experiment was initially attempted at 100 mTorr and then at 10 mTorr. This was just the initial signal generator set up. In this experiment several modulation depth/rate combinations were tried.

The result shows a damped oscillation with a period of oscillation of about 11 μs. This was much longer than expected. In fact, the decay constant, T_2, was only expected to be 2-3 μs. The shape of the response did change with pressure. At 100 mTorr the response looked like the overdamped response of a second order system. At 10 mTorr, the response had overshoot and looked like the response of an underdamped second order system. However, the period of the oscillation was unchanged. The experiment was repeated at these pressures this time with the modulation depth increased up to 5 MHz. We expected the period of the oscillation to change with modulation depth; it did not. We began to suspect that what we were seeing was not the transient response of the water vapor molecules but was instead associated with the settling time of the signal generator. In the past, there had been reports that one of the issues with using pulsed modulation is the settling or stabilization time of the switched frequency [53]. If the stabilization times are longer than the relaxation time of the molecules, the technique does not work. We suspected that this might be the situation with the Agilent E8254A synthesizer.

4.3.2 Analysis of the Agilent E8254A Signal Generator

It was decided that a check of the Agilent E8254A signal generator settling time would be made. This could be done in a manner similar to how the VDI WR1.5ZBD detector was tested, by sitting on the edge of the transition line (where the modulation is the greatest) and comparing the amplitude of the response against the intensity of the absorption line at various line widths (pressures). When the signal generator switches between frequencies, it needs a finite amount of time in order to lock on to the target frequency and become stable

at that frequency. This settling time must be less than the time it takes for the molecular relaxation processes to finish. Otherwise, the molecular relaxation processes cannot be observed. To test this idea, we dithered about the resonant frequency of the molecules as seen in Fig. 4.7.

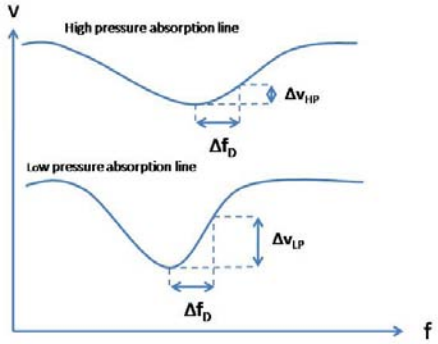

Figure 4.7: The voltage amplitude fluctuation Δv is much greater for a low pressure narrow line than for a high pressure broad line for a given dither frequency Δf.

If the signal generator settling time is too long, we should expect to see the following. With a broad line width, higher pressures, we should see a very small fluctuation in the amplitude of the oscillations (small Δv) relative to the line intensity for a given frequency ditherΔf. With a narrow line width, low pressure, we should see a larger fluctuation in amplitude of the oscillations (large Δv) relative to the line intensity for a given frequency ditherΔf. In these tests, all system parameters are held constant except pressure.

The signal generator was set up to oscillate about the resonant frequency of 325 GHz. The rate or frequency of this oscillation was 1 kHz. The depth of this oscillation was 1 MHz. The results are in Table. 4.3. Note, the line intensities were measured from the baseline to the peak.

As is seen in the table, the amplitude of the oscillation is a function of the line width

Pressure	V_{osc}	$V_{intensity}$	$V_{osc}/V_{intensity}$	T_{settle}
1.0 mTorr	4.64 mV	10.16 mV	0.457	330μs
10 mTorr	6.59 mV	15.1 mV	0.436	330μs
100 mTorr	2.89 mV	86.52 mV	0.033	274μs

Table 4.3: Measured amplitudes of the 11 μs oscillations, the line intensities, their ratios, and the settling times at various pressures

and pressure. The ratio of the amplitude of the oscillation to the amplitude of the intensity was significantly smaller for high pressure than for low pressure. Further, the settling times are well beyond those expected for the relaxation processes in a molecular transient response. It was our conclusion that the Agilent E8254A's settling time was too long for the frequency switching method being attempted here to be effective.

4.3.3 Fast Sweep

With the conclusion that the frequency switching method would not work in this study due to the limitation of the Agilent E8254A signal generator's settling time, we decided next to try a method in which the synthesizer maintained phase continuity and the settling time was irrelevant. The fast passage methods of time domain spectroscopy do not use a square wave to modulate the illuminating radiation's frequency. Instead, they use a modulation waveform that is continuous through the resonant frequency and that sweeps through the resonant frequency at a rate given by:

$$\alpha = \frac{d\omega}{dt} \tag{4.22}$$

where $\alpha \gg \frac{1}{T_2^2}$ is necessary to achieve fast passage. Thus, we hoped to avoid the problem of settling time as the Agilent synthesizer would only have to sweep through the resonance in a continuous fashion. Wolf [9] gives a thorough explanation of the fast passage method. Fig. 4.8 [9] shows the expected transient response of the imaginary part of the macroscopic polarization, P_i, for various sweep rates, α.

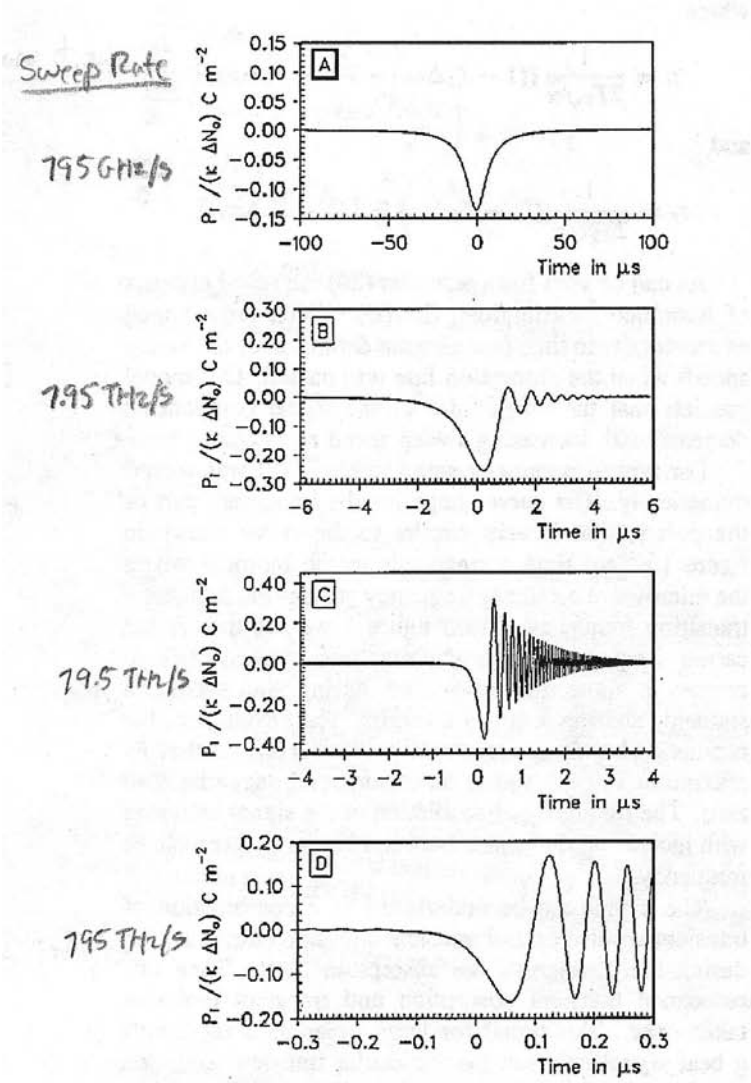

Figure 1. Calculated imaginary parts of the macroscopic polarization for the fast sweep regime versus time relative to the absorption line centre (time = 0) for the sweep rates 50×10^{11} rad s^{-2} (A), 50×10^{12} rad s^{-2} (B), 50×10^{13} rad s^{-2} (C), and 50×10^{14} rad s^{-2} (D).

Figure 4.8: Transient responses of the imaginary part of the macroscopic polarization, P_i, at various sweep rates, α. From Wolf [9].

In this study, two modulating waveforms were chosen, a triangle wave and a sine wave. Both waveforms were used to modulate the sweep of the incident radiation over the 325 GHz transition resonance. A discussion of those measurements follows next.

4.3.4 Fast Sweep Measurements at 325 GHz

The next experiment attempted was in the fast sweep regime. As can be seen in Fig. 4.1, the fast sweep regime is characterized by a sweep rate between 2π to 40π THz/s.

The experimental set up was same as for the original frequency domain measurements, see Fig. 3.1, with one difference. The SRS Model SR5600 low noise preamplifier was replaced by a Mini-Circuits ZFL-500LN+ low noise amplifier. The ZFL-500LN+ is a higher bandwidth amplifier than the SRS600 and therefore better able to process the microsecond transient signals we expected to see. The ZFL-500LN+ is housed in an inline coaxial package. It requires external power. An Agilent E3620A dual output adjustable DC power supply was used for this purpose. The supply voltage to the detector was unipolar, +15 volts and ground.

The Agilent E8254A signal generator was set to the settings given in Table 4.4

Modulation	FM
Modulating Waveform	Triangle Wave/Sine Wave
Frequency(MHz)	13548.03829167
FM Deviation(MHz)	1.000
FM Rate(kHz)	100.0
Amplitude(dBm)	10.0
FEM Transmitter Output(mW)	2.9

Table 4.4: Signal generator setup for 325 GHz fast sweep measurements.

The triangle wave modulation was used first. This modulation, with depth and rate given in Table 4.4, resulted in a frequency sweep rate of α = 9.6 THz/s. Measurements were made at pressures of 1, 10, 20, 40, 100, and 150 mTorr. Fig. 4.9 shows the modulation signal input. Fig. 4.10 shows a typical transient response of the water vapor. This particular

response was at a pressure of 40 mTorr. Fig. 4.11 shows the response with the time scale zoomed in. Fig. 4.12 shows the same response as Fig. 4.11 with the baseline effects removed.

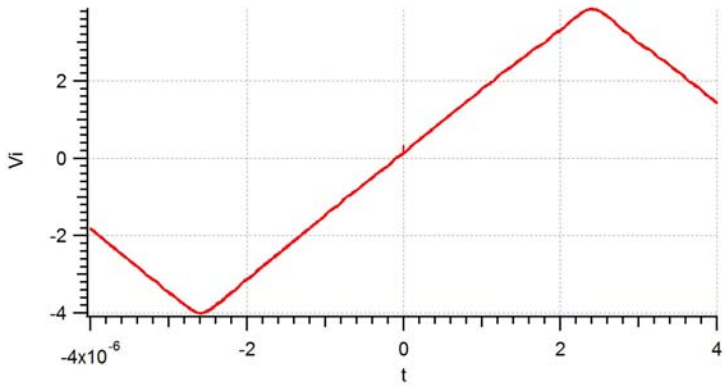

Figure 4.9: 325 GHz fast passage triangle wave modulating signal input.

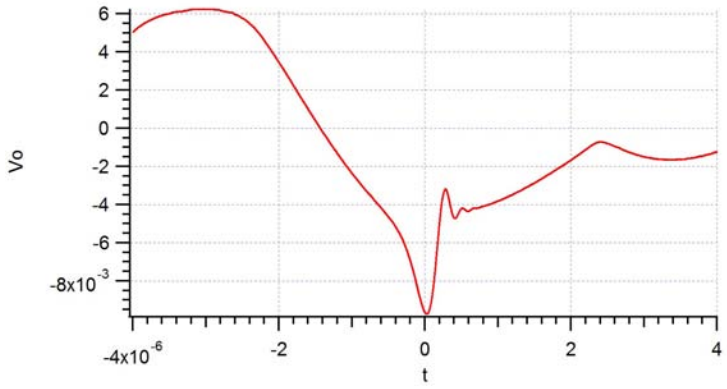

Figure 4.10: 325 GHz fast passage transient response at 40 mTorr.

As can be seen from Fig. 4.10 through Fig. 4.12, we are seeing the expected transient response due to the fast sweep of the resonant frequency. The experiment was repeated using a sine wave to modulate the incident radiation frequency. The sine wave modulation, with depth and rate given in Table 4.4, resulted in a frequency sweep rate of $\alpha = 4.8\pi$ THz/s ($\approx$ 15.1 THz/s). Fig. 4.13 shows the modulation signal input. Fig. 4.14 shows a

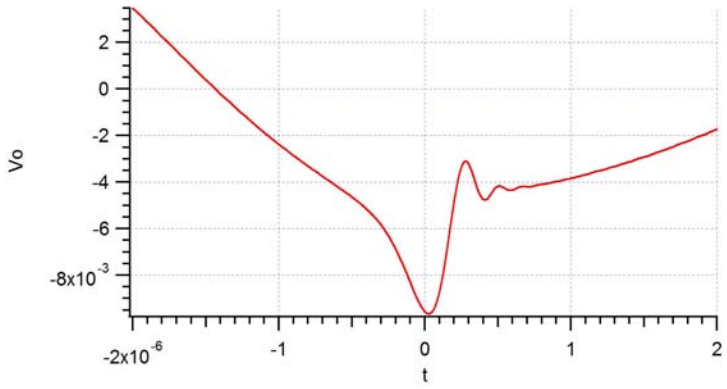

Figure 4.11: 325 GHz fast passage transient response at 40 mTorr (zoomed in time scale).

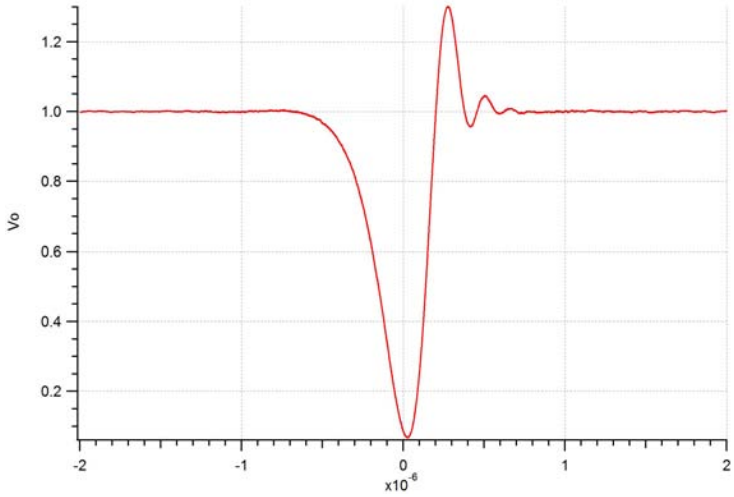

Figure 4.12: 325 GHz fast passage transient response at 40 mTorr (zoomed in time scale) with the baseline effects removed.

typical transient response of the water vapor. This particular response was at a pressure of 40 mTorr. Fig. 4.15 shows the response with the time scaled zoomed.

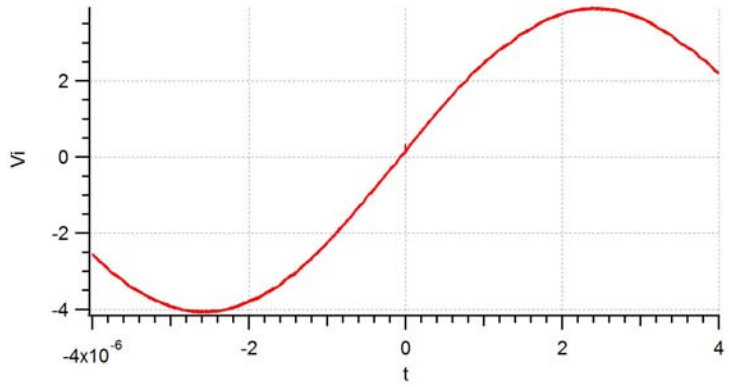

Figure 4.13: 325 GHz fast passage sine wave modulating signal input.

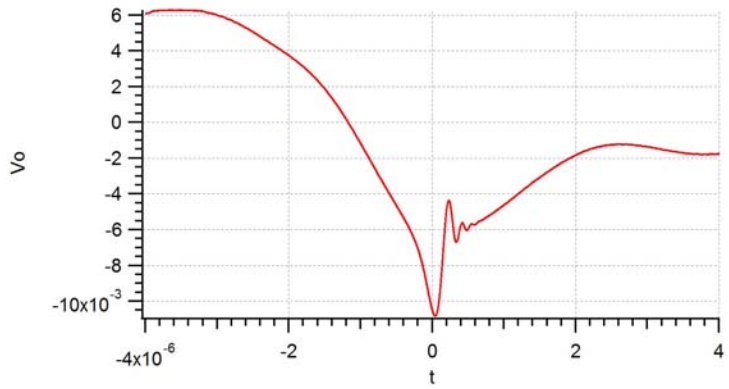

Figure 4.14: 325 GHz fast passage transient response at 40 mTorr.

The sine wave modulation produces better transient responses than the triangle wave. This is due to the fact that the sweep rate for the sine wave at resonance is greater than the sweep rate for the triangle wave ($\alpha_{sine} > \alpha_{triangle}$). The slope of a sine wave is greater than the slope of a triangle wave at the midpoint. Finally, we should note that the 100 kHz modulation rate was the limit for the triangle wave modulation. The sine wave modulation limit is 1 MHz. We were not even close to that. Fig. 4.16 shows the same response as Fig. 4.15 with the baseline effects removed.

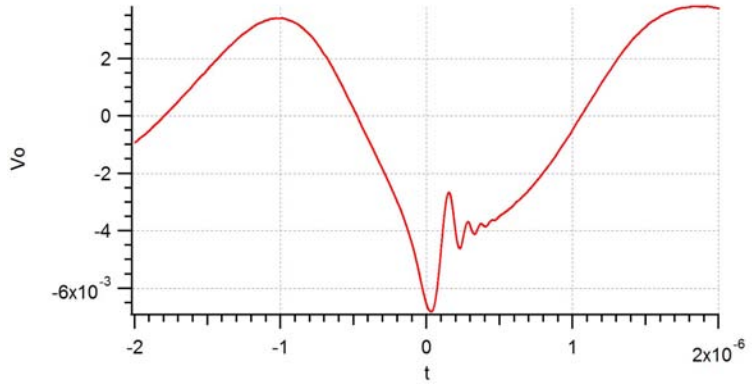

Figure 4.15: 325 GHz fast passage transient response at 40 mTorr (zoomed in time scale).

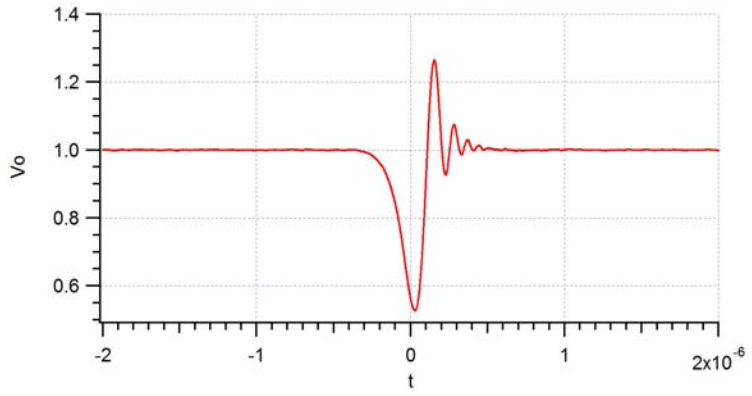

Figure 4.16: 325 GHz fast passage transient response at 40 mTorr (zoomed in time scale) with the baseline effects removed.

4.3.5 Study of the 325 GHz Transient Response

There are no known analytical solutions to the Optical Bloch Equations in the fast sweep regime. As can be seen by looking at either Fig. 4.12 or Fig. 4.16, the basic response is that of an exponentially decaying sinusoidal function. However, the frequency of the harmonic terms is time dependent. Fig. 4.17 shows the 325 GHz line transient response versus a simple exponentially decaying sine wave labeled $ywave$.

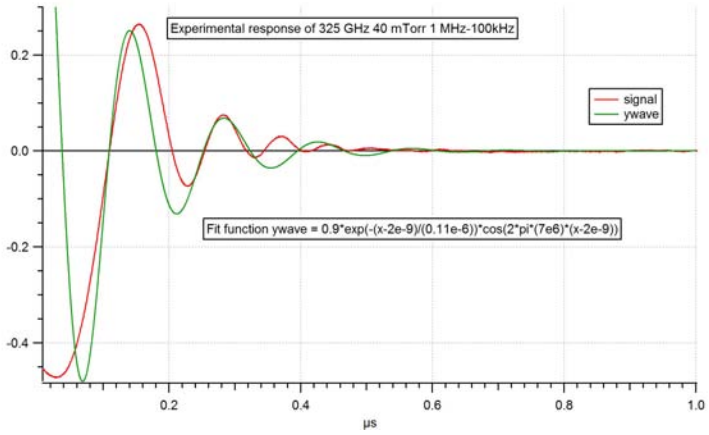

Figure 4.17: 325 GHz fast passage transient response at 40 mTorr(with the baseline effects removed) versus a decaying sinusoidal function.

This fit was done in Igor Pro. The function $ywave$ was built from elementary exponential decay and sinusoidal functions in an attempt to get a rough fit. It was overlaid across the plot of the signal transient response to highlight the differences between the two. As can be seen in the figure, the harmonic term of the signal response does not have a constant frequency but has a frequency that increases with time. Therefore, $ywave$ is not very good fit.

The next step was to attempt to fit a function built from a decaying exponential and a ”chirp” function (sinusoidal function with a linearly increasing frequency). The base function used was

$$f(x) = Ae^{-\alpha(x-x_0)}\sin(F(x-x_0)(G(x-x_0)-\phi) \tag{4.23}$$

Figure 4.18 shows the results for an FM deviation of 1 MHz (2 MHz span) and a modulation rate of 100 kHz. A triangle wave was used as the modulating signal. The sweep time on the oscilloscope was 5 μs. This fit was also done using Igor Pro. The sweep rate for the incident radiation was 9.6 THz/s or 6.032 x 10^{13} rad/s^2. Note that the bottom graph is the original data overlaid with the fitted curve, the middle graph is the residual, and the top graph is the same as the middle but vertically magnified by 10x.

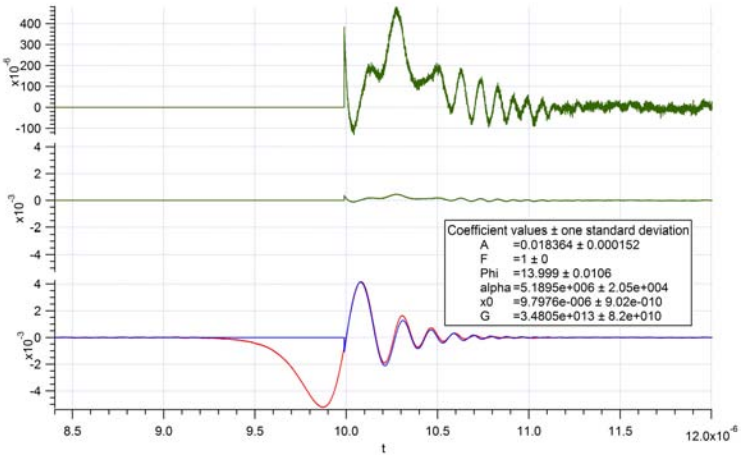

Figure 4.18: 325 GHz fast passage transient response versus an exponentially decaying chirp function.

As can be seen, the fit is better than the pure exponentially decaying sinusoid. However, the exponentially decaying chirp function is not a perfect fit either. The chirp fit does model the behavior of the transient response but only if the fit starts around 10 μs. Before 10 μs, the fit function starts to break down, getting worse the earlier it is applied. 10 μs was the point in time where the sweep crossed the molecular resonant frequency. This makes me wonder how much of the response is transient and how much steady state? If the response is cut in half, the left half would look very much like the front of a steady state type response (treated in Chapter 3), while the right half shows the characteristic ring down behavior of a transient response. This makes some sense though as the physics is not the same in both halves. The incident radiation's frequency is being swept through the resonant frequency of the molecules. Before 10 μs, the incident radiation is approaching

resonance and the molecules are starting to polarize and therefore absorb energy. Once the resonance point is passed, transient emission occurs as the molecules dephase. We then see the characteristic exponentially decaying beat frequency between the radiation emitted by the molecules (at the molecular resonant frequency) and the incident radiation. Therefore, the left side is the result of absorption caused by polarization of the molecules and the right side is the result of transient emission, two different phenomena. Given this, I believe that the fit really only needs to work on the right half of the response.

In order to fit a curve to the entire transient signal, a full blown numerical solution to the Optical Bloch Equations is needed. A numerical simulation which solves the Optical Bloch Equations was developed using Matlab Student Version 7.1 from The MathWorks. The code for this simulation is given in the Appendix. The simulation consists of seven files: the main program file called bloch.m, the differential equation program file dpdt.m, a program file delta_omega.m that calculates $\Delta\omega$ at each time step, a bandpass digital filter file bp_filter.m, and three data files signal40.txt, signal20.txt, and signal10.txt. A short description of each file follows.

The main file, bloch.m, contains the function $bloch$. Function $bloch$ sets up all the constants and initial conditions for the Optical Bloch Equations and then calls the built in Matlab ordinary differential equation solver ode45 to numerically solve the system. Note that since the Optical Bloch Equations consist of a system of three coupled ordinary differential equations, three solutions will be returned, all as functions of time: the real part of the polarization, the imaginary part of the polarization, and the population difference between the two levels. Most of the constants used in the calculation are standard. A couple deserve some comment. $T1$ and $T2$ are the population and polarization relaxation times. They are set equal to one another as there is good evidence that they are approximately equal in the gas phase through the microwave and infrared regions [47]. The variable mu is the dipole matrix element for water vapor at 325 GHz. Its value was retrieved from the HITRAN molecular spectroscopy database [54] [55]. Finally, the variable N, is the total

molecular concentration in the gas at the given pressure. The formula for N was taken from Gordy and Cook [5]. The initial conditions were set up per the numerical solution calculated by Wolf [9]. In addition, $bloch$ reads in data from one of the text files (signal40.txt, signal20.txt, or signal10.txt). These data files contain the experimentally measured transient response of the water vapor at 40, 20, and 10 mTorr as digitized and recorded by the oscilloscope. The baselines have been removed from these data files. A sample plot of this response at 40 mTorr is shown in Fig. 4.12. These responses were due to fast sweeps using triangle wave modulation with modulation rates of 100 kHz and modulation depths of 48 MHz. The data file read will be the one corresponding to the current pressure being analyzed. Data from this file is read into the vector sig. Vector sig contains two columns of data: the time base and the response. $bloch$ uses the time base from sig as the time base for the simulation. This way, the conditions for the simulation are as close as possible to those existing during the experiment. The number of data points the simulation calculates is 10,000. This matches the number of data points in the experimentally measured response. The three numerical solutions to the Optical Bloch Equations are returned in the form of two vectors called t and p. t contains the time base; p, contains the three solutions. Of the three solutions, we are interested in the imaginary part of the polarization which is the second of the three solutions. This solution is extracted from p, normalized, and stored in a new vector p_i. The user of the program has the option of applying a built in band pass filter to p_i via the bp_filter.m file. The filtering option is selected by passing a "1" into the main function $bloch$ when calling it. The filtering is bypassed by passing a "0" into $bloch$. The filtering is programmed as an option as the Matlab Signal Processing Toolbox is required to run it. Not all Matlab systems come with this toolbox. The student version of Matlab does not. Therefore, application of the filter was left optional so the program could run on student versions of Matlab. Whether filtered or not, a Fast Fourier Transform (FFT) is taken on p_i. At this point, no analysis is done on the FFT. Finally, the computed solution, p_i, and the measured experimental response,sig, are compared. The two waveforms

are plotted together over the same time base. The residual between the two signals is also calculated and plotted. The Root Mean Square (RMS) value of the residual is calculated as well to determine how well p_i and sig match as simulation input parameters are varied.

The file dpdt.m contains the function $dpdt$, which is essentially the definition of the Optical Bloch Equations that the Matlab ode45 solver will solve. The form of the equations used is from Brailovsky [46]. The $dpdt$ function calls $delta\_omega$ during each time step to generate the proper $\Delta\omega$ for that time.

The file delta_omega.m contains a simple function $delta\_omega$ which calculates and returns $delta\_omega$ ($\Delta\omega$) at time t, where $delta\_omega$ is the frequency difference between the current frequency, $omega$, and the resonant frequency, $omega0$.

The file bp_filter.m contains the function bp_filter. bp_filter uses the Matlab built in function $fdesign.bandpass$ to create a digital Infinite Impulse Response (IIR) bandpass filter of the Butterworth type. IIR filters are digital filters that have an impulse response that is non-zero over an infinite amount of time. The Butterworth type filter is a filter with a pass band that is as mathematically flat as possible, no ripples in the pass or stop bands. The Butterworth IIR is known for stability and processing efficiency but at the cost of a slower roll off with frequency. The parameters that determine the pass and stop bands as well as the attenuation in these bands are listed in the program. bp_filter is set up to pass signals between 100 kHz and 50 MHz.

The three data files signal40.txt, signal20.txt, and signal10.txt contain the digital values for the transient responses at 40, 20, and 10 mTorr respectively. The transient responses have been processed to the extent that their baselines have been removed. This was done via polynomial curve fitting using Igor Pro.

The process for "fitting" the simulation results to the experimental responses was done as follows. First, the data file corresponding to the pressure being studied was coded into the function $bloch$. The pressure variable P_mm was set to correspond to the pressure being studied. The variable $T2$ was set to some initial guess value. The program was executed.

The plots of the simulated and measured responses were studied as was the residual plot. The RMS value of the residual was recorded. Next, the value of $T2$ was changed to a lower value and the program executed again. The value for the second residual RMS was compared against the first RMS value. The next $T2$ is then selected. If the value of the second RMS was higher than the original RMS (indicating a larger residual), the third $T2$ value will be higher than the original. If the value of the second RMS was lower than the original (indicating a smaller residual), the third $T2$ value will be lower than the original. The program was executed again and the new (third) RMS value recorded and compared against the previously lowest value. The next $T2$ value was selected. This iterative process was repeated until the optimal $T2$ value was determined. The optimal $T2$ value is that value which corresponds to the lowest residual RMS value. Once the optimal $T2$ value was identified, it was used to calculate the FWHM value for that pressure per Tanaka et al [50]

$$FWHM = 2\Delta\nu = \frac{1}{\pi}\left[\left(\frac{1}{T_2}\right)^2 + x^2\left(\frac{T_1}{T_2}\right)\right]^{\frac{1}{2}} \tag{4.24}$$

where $x = \mu\mathcal{E}/\hbar$. In the limiting case of low MMW power the $1/T_2$ term is much larger (in our case by about 10^8) than the second term so we used

$$FWHM = 2\Delta\nu = \frac{1}{\pi T_2} \tag{4.25}$$

Figs. 4.19 - 4.21 show the plots of the simulation transient responses, the measured transient responses, and the residuals for 10, 20, and 40 mTorr. Table 4.5 shows the optimal T_2 values, their associated FWHM values, the FWHM values calculated from the Voigt profiles from the steady state spectroscopy measurements and analysis, and the difference between the FWHM values.

As can be seen in the figures, the simulated and measured transient responses did not

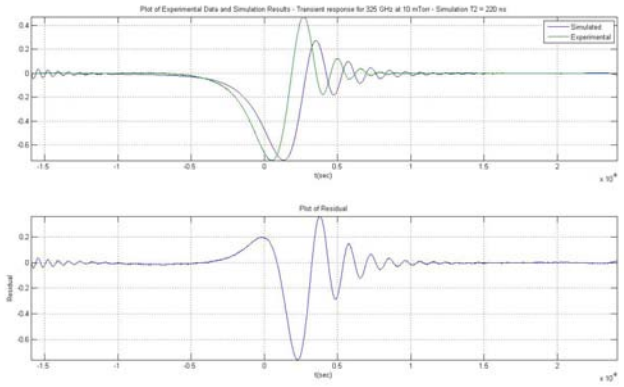

Figure 4.19: Above - 325 GHz fast passage transient response at 10 mTorr, measured response versus simulated. Simulation T_2 = 220 ns. Below - residual.

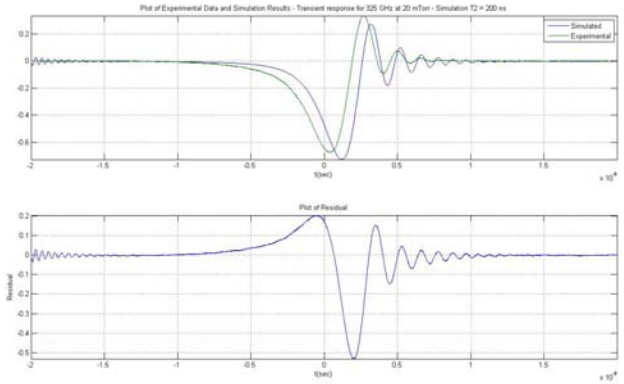

Figure 4.20: Above - 325 GHz fast passage transient response at 20 mTorr, measured response versus simulated. Simulation T_2 = 200 ns. Below - residual.

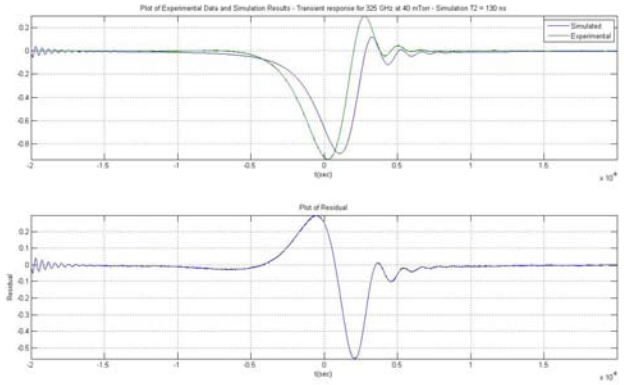

Figure 4.21: Above - 325 GHz fast passage transient response at 40 mTorr, measured response versus simulated. Simulation T_2 = 130 ns. Below - residual.

Pressure (mTorr)	T_2 (ns)	FWHM (MHz - transient)	FWHM (MHz - Voigt)	% Difference
10	220	1.4469	1.279	+13.1
20	200	1.5915	1.5453	+2.99
40	130	2.4485	2.157	+13.5

Table 4.5: Experimental versus measured FWHM for 325 GHz transient response

line up in time even though the same time base is used for both. In addition, the simulations show many more oscillations than the measured responses do. A similar result was reported by Duxbury et al when comparing measured transient responses to those calculated via solution to the Optical Bloch Equations in the infrared region [56]. Duxbury's explanation is that the transient response discrepancies are due to the effects of Doppler broadening. This explanation may apply in our case as we are operating at very low pressures and the Optical Bloch Equations do not take Doppler broadening into account.

Further, the FWHM values calculated from the transient simulation are larger than those calculated from the steady state linewidth measurements. This implies that the T_2 values calculated from the transient simulation are smaller than those that would be calculated from the steady state measurements. Whether the T_2 difference is due to experimental or physical effects is not known. Schwendeman comments on seeing similar discrepancies between transient and steady state measurements of T_2 [51].

Using the FWHM values calculated from the transient responses, the pressure broadening parameter, γ, may be calculated. Fig. 4.22 shows the fit of the FWHM versus pressure curve and its slope, γ.

The slope of the fitted curve in Fig. 4.22 is 34.73 MHz/Torr. The HWHM value published by Koshelev et al. in 2007 is 18.51(3) MHz/Torr [41]. This corresponds to a FWHM γ of 37.02(6) MHz/Torr. Our value is 6.19% less than this published value. The pressure broadening parameter that we calculated earlier from the combined steady state measurement data was 37.41(1) MHz/Torr. The difference betweeen the pressure broadening parameter calculated from the transient measurements and the pressure broadening

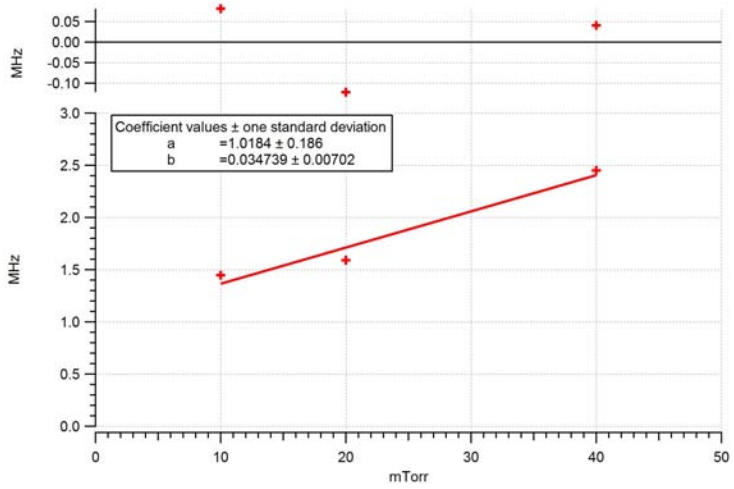

Figure 4.22: Pressure broadening parameter, γ, for H_2O at 325 GHz calculated from the transient response.

parameter calculated from the steady state measurements is 7.16%.

Note that we did attempt to measure the transient responses of the 325 GHz water vapor absorption line at 100 mTorr and 150 mTorr. Due to pressure broadening, we were unable to see the transient responses at these higher pressures.

Summary and Discussion

In this study, we have examined the phenomena of attenuation of MMW/THz radiation by the atmosphere. There are three primary sources of that attenuation: 1) absorption of the radiation by gas molecules that make up the atmosphere (mostly water vapor and O_2), 2) scattering by hydrometeors and particulates suspended or falling in the atmosphere, and 3) scintillation caused by small pockets of higher/lower humidity air that refracts the wavefront of the radiation causing distortion and phase noise. This study concentrated on the theoretical descriptions of absorption and scattering and the experimental study of absorption by H_2O.

Rotational energy of molecules is quantized and MMW radiation is absorbed by molecules when they transition to higher energies. MMW radiation is emitted when molecules transition to lower energies. The description of quantum rotational states is governed by the Schrödinger equation, solutions to which give the energies (eigenvalues) and rotational states (eigenstates or linear combinations thereof) for the molecule. The eigenstates for molecular rotation can be fairly simple, as in the case of diatomic (linear) molecules, or very complicated, as in the case a symmetric rotors. H_2O is an asymmetric rotor and therefore has very complicated motions and a very rich spectra. The shape of the individual lines that make up the molecular spectra were studied. It was found that spectral lines are not lines at all, but have a finite width to them. This width varies under the conditions of measurement with temperature and pressure being the dominant parameters. There are five causes for line broadening. The two of most concern in this study were Doppler broadening

and collision/pressure broadening. Doppler broadening is due to velocities of the molecules relative to the radiation during the interaction. Doppler broadening increases with temperature. Collision/pressure broadening is due to collisions between the molecules during the interaction with the radiation. These two processes account for unique lineshapes: Gaussian for Doppler and Lorentzian for collision/pressure. At atmospheric pressure, collision broadening dominates. There are several analytical solutions that attempt to describe spectral lineshapes. However, none of them accurately describes real world lineshapes at atmospheric pressure. They underestimate absorption in the wings. This is known as anomalous absorption. Anomalous absorption is thought to be due to a most likely fallacious assumption common to all of these models, that collisions are instantaneous. Non-instantaneous collisions would give rise to collision induced absorption that would account for the shortcoming of the models.

When MMW radiation encounters macroscopic particles, it is scattered. The details of scattering processes are explained by quantum electrodynamics and are beyond the scope of this study. However, we did discuss the effects of scattering. The effects of the scattering are determined by the ratio of the radar cross section of the scatterer to the wavelength of the radiation. For MMW radiation, Rayleigh scattering governs interactions with particles the size of fog droplets and smaller. Mie scattering governs the interactions with particles the size of raindrops. Optical scattering governs the interactions with particles the size of hailstones and larger. Scattering occurs when a photon ”collides” with a molecule. This ”collision” alters the trajectory of the photon. It is knocked of its original course and carries its energy away with it. Because of this, the energy received at the intended target is reduced. The propagating signal is attenuated.

Molecular spectroscopy is used to study the spectra and therefore the behavior of molecules. In this thesis, two methods of spectroscopy where used to study the behavior of H_2O: steady state and transient (a.k.a. frequency domain and time domain respectively).

The steady state spectroscopy experiments measured the pressure broadening parame-

ter, γ, for the 620 and 325 GHz transition lines of H_2O. The experimental setup is discussed in detail in Chapter 3. In steady state spectroscopy, the incident radiation is swept linearly with frequency over the molecular resonant frequency at a rate that is slow relative to any molecular relaxation process. In this regime, the peak absorption is independent of sweep rate and only absorption processes are present. Line widths were measured at various pressures for each transition. Voigt curves were fitted to each measured curve. It was necessary to develop a procedure for removing the baseline and the Doppler broadening (Gaussian) component from each measured line during the fit. The FWHM was then calculated for each curve. The FWHM was then plotted against pressure for each transition line. The relationships were linear or very close to linear. From each of these FWHM versus pressure lines, the value of γ was determined as γ is the slope of the line. Our calculated γ values were within 2.69% and 1.05% of published values for the 620 and 325 GHz transition lines respectively. Two factors are to be noted with regard to the steady state study. The residual curves for most of the lines had a W shape and the fitted lines for the FWHM versus pressure had nonzero y-intercepts. These anomolies have been seen in previous studies and are believed to be an effect of ignoring the speed dependence of relaxation and molecular confinement [40]. These anomalies are believed to be artifacts of the Voigt lineshape assumption and can be mitigated or possibly eliminated with the use of more sophisticated profile fitting. This would be a recommended area for future investigation.

The transient spectroscopy experiments measured the polarization relaxation time, T_2, for the 325 GHz transition line for H_2O. The fast sweep method was used. The experimental setup is discussed in detail in Chapter 4. Fast sweep is a type of transient spectroscopy. In fast sweep, the incident radiation is swept over the molecular resonant frequency at a rate that is much faster then any molecular relaxation process. In this regime, peak absorption increases with sweep rate and both absorption and emission processes are present. For our experiments, the sweep was modulated both linearly, with a triangle wave, and non-linearly, with a sine wave. Only the triangle wave (linear sweep) was analyzed. The

transient response of the 325 GHz H_2O transition was measured at 10, 20, and 40 mTorr. We attempted to measure T_2 for each of these transient responses. This was done via curve fitting. In preparation for the fitting, the baselines for the measured transient responses were removed.

The fast sweep phenomena can be described by a system of three couple ordinary differential equations known as the Optical Bloch Equations (OBE). Mathematically, the form of the OBE is identical to the Bloch Equations used to describe NMR processes. There is no closed form solution to the OBE in the fast sweep regime. Only numerical solutions are available. A Matlab program was developed to solve the OBE; the relaxation time T_2 was a variable in this program. Further, the program read in the measured response data for comparison against the calculated response. Plots of the measured responses, the calculated responses, and their residuals were generated. An iterative process was developed to determine which value of T_2 produced the simulation waveform that matched the measured waveform the closest. Based upon the optimal T_2 values, FWHM values were calculated for each pressure (there were only three). These FWHM values were then plotted against pressure to calculate γ as was done in the steady state analysis. The value of γ calculated using the transient response data was within 6.19% of the published value. Thus, the transient γ was actually closer to the published value than our original steady state γ. Two comments should be made with regard to the transient study. First, despite the fact that they used the exact same time base, none of the calculated transient responses lined up in time with the measured transient responses and the calculated results show many more oscillations than the measured do. A similar result was reported by Duxbury [56]. The exlanation here is that the difference between the calculated and measured responses is due to Doppler broadening. The OBE do not take Doppler broadening into account so this may be reasonable. Second, the FWHM values calculated from the transient responses are all larger than those calculated from the steady state responses. Due to their reciprocal relationship, this means that the relaxation times, T_2, are smaller for the transient responses

than for the steady state. This effect has been seen by Schwendeman [51]. It is not known whether this effect is due to experimental or physical causes. Future study on this project would certainly want to focus on these anomalies. In particular, perhaps some type of Maxwell-Boltzmann velocity distribution, which contributes to Doppler broadening, can be coupled into the OBE simulation.

An interesting result to look at is the comparison of the pressure broadening curves derived from the steady state and the transient spectroscopic methods. This is basically a plot that combines Fig. 3.14 with Fig. 4.22. This comparison is shown in Fig. 5.1 and is in some respects the capstone for this work.

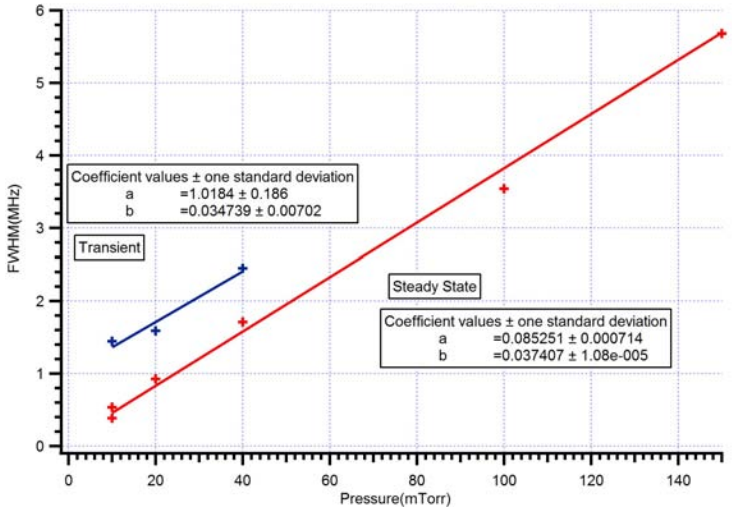

Figure 5.1: Pressure broadening parameter, γ, for H_2O at 325 GHz calculated from the steady state (red) and the transient response (blue).

The plot shows that the slopes of the two lines, the γs, are very close to being equal. However, the data values are offset. Schwendeman's 1978 review paper [51] reports that differences are seen between T_2 values measured using transient methods and T_2 values measured using steady state methods. Note, T_2 is inversely proportional to FWHM. These differences are seen across all pressures and are seen in several of the studies Schwendeman reviewed. In some studies, the transient values are larger than the steady state values. In other studies, the steady state values are larger than the transient values. Schwendeman

does not give a conclusive explanation for this. He is not certain whether these differences occur because of experimental effects or physical effects. He does note that T_2, and T_1, are defined differently for different experiments. He also notes that some of the scatter of the data from single studies and the scatter of the data between different studies may be due to lack of correction for temperature variations. In our studies, variations in the ambient temperature were not taken into account.

Further, there are uncertainties in the pressure measurements due to the absorption of the gas under test by the inner wall of the gas cell and due to uncertain partial pressures. These could add systematic errors to the observations. In our studies, water vapor was let into the gas cell via a valve. The valve was then closed. The pressure of the gas cell was then lowered to the desired value and the measurements were made. This process did not factor in any absorption of the gas by the cell walls. It is possible that different amounts of wall absorption occurred in different experiments which would lead to an offset between data points when making comparisons between experiments. It is also possible that since the flask containing the water source was never purged of air, the ratio of water vapor to air admitted into the gas cell was not the same between experiments. This would result in a variation of water vapor partial pressures between experiments and a data offset. In our experiments and analyses, variation of water vapor partial pressure was not taken into account. It is interesting to note that in our 325 GHz steady state experiment we have two FWHM values for 10 mTorr that were taken in separate experiments. These values do not agree. This says that an offset existed not only between transient and steady state experiments but also between separate steady state experiments as well.

Although these types of systematic variations could cause offsets between the data points taken in different experiments, the slopes of the curves fitted to these data points should still be about the same. This is because the pressure broadening parameter itself would remain fairly constant across small temperature, wall absorption, and partial pressure variations. This is exactly what we saw.

One final point to notice from the figure is the lack of data points for the transient curve at higher pressures. This illustrates a potential shortcoming of the transient method in that one cannot see a transient response at higher pressures without significantly increasing sweep rate. This means moving from the fast sweep to the fast passage regime. The fast passage regime was beyond our ability to explore with the existing instruments in the lab.

Finally in regards to the equipment used, it was experimentally determined that the Virginia Diodes Inc, (VDI) WR1.5ZBD detector was inadequate for use in the transient spectroscopy experiments due to its lack of video bandwidth. Our transient spectroscopic experiments required the measurement of transient signals with time constants below 1 μs. The WR1.5ZBD detector available for our study did not have the video bandwidth to do this. Further, it was experimentally determined that the Agilent E8254A signal generator was inadequate to use in any alternative transient spectroscopy measurements such as frequency switching or rotary echo. Again, transient spectroscopic experiments are characterized by transient signals with time constants of 1 μs or less. In order to make the experiments work properly, frequency sources must have settling times less than these transients. The Agilent E8254A did not.

Bibliography

[1] Fiorino, S. T., Bartell, R. J., Krizo, M. J., Marek, S. L., Bohn, M. J., Randall, R. M., and Cusumano, S. J., 2009. "A computational tool for evaluating THz imaging performance in brownout or whiteout conditions at land sites throughout the world". *Proceedings of the SPIE - The International Society for Optical Engineering,* **7324**, p. 732410 (12 pp.).

[2] Steven C. Wofsy, A. L. R. P. o. A., and Science, E., 2006. Structure of the atmosphere. http://www.learner.org/courses/envsci/visual/visual.php?shortname=structure_atmosphere.

[3] Meeks, M. L., 1976. *Astrophysics - Part B: Radio Telescopes*, Vol. 12 of *Methods of Experimental Physics*. Academic Press, New York, NY 10003.

[4] Townes, C. H., and Schawlow, A. L., 1955. *Microwave Spectroscopy*. McGraw-Hill, New York. [by] C. H. Townes [and] A. L. Schawlow.; Bibliography: p.649-682.

[5] Gordy, W., and Cook, R. L., 1984. *Microwave Molecular Spectra*. Wiley, New York.

[6] Kulpa, S. M., and Brown, E. A., 1979. Near-Millimeter Wave Technology Base Study: Volume I. Propagation and Target/Background Characteristics. Tech. Rep. HDL-SR-79-8, Defense Advanced Research Projects Agency, Nov 1979. Special rpt.

[7] Kopp, C., 2010. Russian / PLA Low Band Surveillance Radars, Technical Report APA-TR-2007-0901. http://www.ausairpower.net/APA-Rus-Low-Band-Radars.html.

[8] Nave, C. R., 2006. HyperPhysics - Rayleigh Scattering. http://hyperphysics.phy-astr.gsu.edu/hbase/atmos/blusky.html#c2.

[9] Wolf, F., 1994. "Fast sweep experiments in microwave spectroscopy". *J. Phys. B: Appl. Phys.,* **27**, pp. 1774–1780.

[10] Amano, T., and Shimizu, T., 1973. "Observation of Transient Nutation Effect in Microwave Transitions of Ammonia Molecule". *Journal of the Physical Society of Japan,* **35**(1), pp. 237–241.

[11] Kasuga, T., Kano, S., and Shimizu, T., 1980. "Measurement of Longitudinal Relaxation Rate Constant of Rotational Transition of H_2O by the Microwave Frequency-Switching Method". *Japanese Journal of Applied Physics,* **19**(11), pp. 2031–2036.

[12] Duling, I., and Zimdars, D., 2009. "Terahertz imaging: Revealing hidden defects". *Nature Photonics,* **3**(11), pp. 630–632.

[13] Medrano, C., 2008. Monitoring Terahertz Technology. Tech. Rep. 3, ARAMIS, 11/30.

[14] Federici, J. F., Gary, D., Barat, R., and Zimdars, D., 2005. "Thz standoff detection and imaging of explosives and weapons". *Proceedings of the SPIE - The International Society for Optical Engineering,* **5781**(1), pp. 75–84.

[15] Johnson, D., and Brooker, G., 2008. "Research radar for unmanned navigation". pp. 165–170. 2008 International Conference on Radar.

[16] Suen, J. Y., Singh, R. S., Taylor, Z. D., and Brown, E. R., 2008. A W-band quasi-optical homodyne Doppler radar for detection of very slow-moving targets.

[17] Zvanovec, S., Piksa, P., Cerny, P., Mazanek, M., and Pechac, P., 2007. Gas Attenuation Measurement by Utilization of Fabry-Perot Resonator.

[18] Redo-Sanchez, A., Kaur, G., Xi-Cheng, Z., Buersgens, F., and Kersting, R., 2009. "2-d Acoustic Phase Imaging with Millimeter-Wave Radiation". *Microwave Theory and Techniques, IEEE Transactions on,* **57**(3), pp. 589–593.

[19] Kim, S., and Nguyen, C., 2004. "On the development of a multifunction millimeter-wave sensor for displacement sensing and low-velocity measurement". *Microwave Theory and Techniques, IEEE Transactions on,* **52; 52**(11), pp. 2503–2512.

[20] Hils, B., Thomson, M. D., Loeffler, T., von Spiegel, W., am Weg, C., Roskos, H. G., de Maagt, P., Doyle, D., and Geckeler, R. D., 2008. "Terahertz profilometry at 600 GHz with 0.5 mu m depth resolution". *Optics Express,* **16**(15), JUL 21, pp. 11289–11293.

[21] Kim, S., and Nguyen, C., 2003. "A displacement measurement technique using millimeter-wave interferometry". *Microwave Theory and Techniques, IEEE Transactions on,* **51; 51**(6), pp. 1724–1728.

[22] Kemp, I. V., 2009. "Sub-MM Wave Imaging and Waveguiding Techniques for Non-Destructive Materials Evaluation". Master's thesis, Wright State University.

[23] Bilitza, D., 2010. International reference ionosphere. http://ccmc.gsfc.nasa.gov/modelweb/ionos/iri.html, February.

[24] Nave, C. R., 2006. HyperPhysics - Rotational Spectra and Structure of a Linear Molecule. http://hyperphysics.phy-astr.gsu.edu/hbase/HFrame.html.

[25] Laboratory, J. P., 2010. Molecular spectroscopy. http://spec.jpl.nasa.gov/ftp/pub/catalog/catform.html.

[26] Debye, P., 1960. *Polar Molecules*. Dover Publications, New York, NY.

[27] Van Vleck, J. H., and Weisskopf, V. F., 1945. "On the Shape of Collision-Broadened Lines". *Reviews of Modern Physics,* **17**(2 and 3), pp. 227–236.

[28] Gross, E. P., 1955. "Shape of Collision-Broadened Spectral Lines". *Physical Review,* **97**(2), pp. 395–403.

[29] Ben-Rueven, A., 1969. *Advances in Atomic and Molecular Physics*, Vol. 5. Academic Press, New York, NY.

[30] Feynman, R. P., 2006. *QED: The Stange Theory of Light and Matter*. Princeton University Press, Princeton.

[31] Horstmeyer, S., 2008. Summary Table - Typical Raindrop Sizes. http://www.shorstmeyer.com/wxfaqs/float/rdtable.html.

[32] Straton, A., 1941. *Electromagnetic Theory*. McGraw-Hill, New York, NY.

[33] Jackson, J. D., 1998. *Classical Electrodynamics*. Wiley Press, New York.

[34] Becker, G. E., and Autler, S. H., 1946. "Water Vapor Absorption of Electromagnetic Radiation in the Centimeter Wave-Length Range". *Physical Review,* **70**(5 and 6), pp. 300–307.

[35] Van Vleck, J. H., 1946. "The Absorption of Microwaves by Uncondensed Water Vapor". *Physical Review,* **71**(7), pp. 425–433.

[36] King, G. W., Hainer, R. M., and Cross, P. C., 1947. "Expected Microwave Absorption Coefficients of Water and Related Molecules". *Physical Review,* **71**(7), pp. 433–443.

[37] Hall, R. T., and Dowling, J. M., 1967. "Pure Rotational Spectrum of Water Vapor". *The Journal of Chemical Physics,* **47**(7), pp. 2454–2461.

[38] Carlon, H., 1978. "Phase Transition Changes in Molecular Absorption-Coefficient of Water in Infrared - Evidence for Clusters". *Applied Optics,* **17**(20), pp. 3192–3193.

[39] Podobedov, V. B., Plusquellic, D. F., and Fraser, G. T., 2004. "Thz laser study of self-pressure and temperature broadening and shifts of water vapor lines for pressures up to 1.4kPa". *Journal of Quantitative Spectroscopy & Radiative Transfer,* **87**(3-4), SEP 1, pp. 377–385.

[40] Priem, D., Rohart, F., Colmont, J. M., Wlodarczak, G., and Bouanich, J. P., 2000. "Lineshape study of the J = 3 $\leftarrow$ 2 rotational transition of CO perturbed by N_2 and O_2". *Journal of Molecular Structure,* **517-518**, pp. 435–454.

[41] Koshelev, M. A., Tretyakov, M. Y., Golubiatnikov, G. Y., Parshin, V. V., Markov, V. N., and Koval, I. A., 2007. "Broadening and shifting of the 321-, 325-, and 380-GHz lines of water vapor by pressure of atmospheric gases". *Journal of Molecular Spectroscopy,* **241**, pp. 101–108.

[42] Kasuga, T., Kuze, H., and Shimizu, T., 1978. "Determinations of relaxation rate constants on the 22 ghz rotational transition of h_2o by coherent transient spectroscopy". *Journal of Chemical Physics,* **69**(11), pp. 5195–5198.

[43] Shimizu, T., Morita, N., Kasuga, T., Sasada, H., Matsushima, F., and Konishi, N., 1979. "Studies of Molecular Relaxation by Infrared and Microwave Coherent Transients". *Applied Physics,* **21**(1), pp. 29–34.

[44] Steinfeld, J. I., 1985. *Molecules and Radiation, An Introduction to Modern Molecular Spectroscopy*. The MIT Press, Cambridge, MA.

[45] Omar, M. A., 1993. *Elementary Solid State Physics*. Addison-Wesley Publishing, Reading, MA.

[46] Brailovsky, A. B., Khodos, V. V., and Vaks, V. L., 2004. "Measurement of the Power Density of Electromagnetic Radiation by the Method of Microwave Nonstationary Spectroscopy". *Radiophysics and Quantum Electronics,* **47**(10-11), pp. 916–920.

[47] McGurk, J. C., Schmalz, T. G., and Flygare, W. H., 1974. "A Density Matrix, Bloch Equation Description of Infrared and Microwave Transient Phenomena". *Advances in Chemical Physics,* **25**, pp. 1–68.

[48] McGurk, J. C., Schmalz, T. G., and Flygare, W. H., 1974. "Fast passage in rotational spectroscopy: Theory and experiment". *Journal of Chemical Physics,* **60**(11), pp. 4181–4187.

[49] Mäder, H., and Bromsdorf, H., 1978. "Microwave Transient Phenomena of Symmetric Top Molecules. An Extended Bloch Type Description". *Z. Naturforsch.,* **33a**, pp. 1493–1497.

[50] Tanaka, K., Akiyama, S., Ikeura, T., and Hirota, E., 1980. "Measurement of the Transverse Relaxation Time T2, of the Inversion Doublets of NH_3 from a Free Induction Decay Signal". *Journal of the Physical Society of Japan,* **48**(3), pp. 951–957.

[51] Schwendeman, R. H., 1978. "Transient Effects in Microwave Spectroscopy". *Annual Review of Physical Chemistry,* **29**, pp. 537–538.

[52] Mäder, H., Ekkers, J., Hoke, W., and Flygare, W. H., 1975. "A π, τ, $\pi/2$ type pulse sequence method of the determination of T_1 in rotational transitions". *Journal of Chemical Physics,* **62**(11), pp. 4380–4387.

[53] Brailovsky, A. B., Khodos, V. V., and Vaks, V. L., 1999. "Millimeter Range Spectrometer with Phase Switching-Novel Method for Reaching of the Top Sensitivity". *International Journal of Infrared and Millimeter Waves,* **20**(5), pp. 883–896.

[54] Rothman, L., 2009. The HITRAN database. http://www.cfa.harvard.edu/HITRAN/.

[55] Rothman, L., I.E.Gordon, A.Barbe, D.ChrisBenner, P.F.Bernath, M.Birk, V.Boudon, Brown, L., A.Campargue, J.-P.Champion, K.Chance, L.H.Coudert, V.Danaj, V.M.Devi, Fally, S., J.-M.Flaud, R.R.Gamache, A.Goldmanm, D.Jacquemart, I.Kleiner, Lacome, N., W.J.Lafferty, J.-Y.Mandin, S.T.Massie, S.N.Mikhailenko, C.E.Miller, Moazzen-Ahmadi, N., O.V.Naumenko, A.V.Nikitin, J.Orphal, V.I.Perevalov, A.Perrin, A.Predoi-Cross, C.P.Rinsland, M.Rotger, M.Simeckova, M.A.H.Smith, K.Sung, S.A.Tashkun, J.Tennyson, R.A.Toth, A.C.Vandaele, and J.VanderAuwera, 2009. "The HITRAN 2008 molecular spectroscopy database". *Journal of Quantitative Spectroscopy and Radiative Transfer,* **110**, pp. 533–572.

[56] Duxbury, G., Langford, N., McCulloch, M. T., and Wright, S., 2005. "Quantum cascade semiconductor infrared and far-infrared lasers: from trace gas sensing to non-linear optics". *Chemical Society Reviews,* **34**, pp. 921–934.

Matlab file bloch.m

```
function bloch(filt)

% 3/9/10 John Cetnar
% Solves the Optical Bloch Equations numerically for a two level system.
% If filter is true, the solution to the imaginary (quadrature) component
% of the polarization is filtered with a BP filter, else no filter is
% applied.  In either case, the imaginary (quadrature) component is
% plotted; the FFT is calculated and plotted.
%
% Inputs:
%   filt = Boolean value that determines whether to apply the BP filter
%          or not.  If filter = 1 apply BP filter.  If filter = 0, do not
%          apply the BP filter. Used since the filter utility is part of
%          Matlab Signal Processing Toolbox which is not available on all
%          versions (Student Version).
%
% Variables:
%   T2 = Polaration (dephasing) relaxation time
%   T1 = Population relaxation time
%   mu = matrix transition element for the dipole moment
%   P = power of the driving radiation
%   E0 = amplitude of the driving electric field
%   h = Plank constant
%   hbar = reduced Planke constant
%   k = Boltzmann constant
%   omega = frequency of the driving radiation
%   omaga0 = resonant frequency of the transition
%   depth = modulation depth
%   N = the number of molecules per unit volume
%   E1 = energy of the lower state
%   N1 = the number of molecules per unit volume in the lower state
%   N2 = the number of molecules per unit volume in the upper state
%   delta_ N_eq = equilibruim population difference between the upper and
%                 the lower state
%   kappa = dipole moment times 2/hbar
```

```
%   p1_0 = initial real part of the polarization
%   p2_0 = initial imaginary part of the polarization
%   p3_0 = initial population difference
%   n = number of points in the solution vector
%   nfft = number of points in the FFT (Fast Fourier Transform) operation
%   tspan = time scale in the solution vector
%   p1 = real part of the polarization
%   p2 = imaginary part of the polarization
%   p3 = population difference
%   p_i = imaginary part of the polarization w/o filtering, same as p2.
%   fp_i = p_i filtered with a band pass filter 100 kHz - 50 MHz
%   pfft = FFT of p_i
%   f = Frequency scale for the FFT of p_i
%   mu0 = permeability of free space
%   c = speed of light in vacuum in m/s
%   f0 = resonant frequency in Hz
%   rate = modulation rate in Hz
%   dev = modulation deviation (depth) in Hz
%   r = radius of gas cell in meters
%   T = Temperature in Kelvin
%   Pmm = Pressure in mm Hg = Pressure in Torr
%   srate = sample rate of the oscilloscope
%   sig = experimental data read in from file signal.txt

% Define program numerical calculation constants
n = 10000;                  % number of data points
nfft = 2^nextpow2(n);       % Next power of 2 from length of y
srate = 100e6;              % sampling frequency (100 MHz oscilloscope)

% Define physical constants
h = 6.626e-34;
hbar = h/(2*pi);
c = 3.00e8;
mu0 = 4*pi*1e-7;
k = 1.38e-23;

% Define relaxation times
T2 = 130e-9;
T1 = T2;

% Define dipole moment strength for 325 GHz line
mu = 0.188 * (3.336e-30);
kappa = mu/hbar;

% Define experimental input constants
```

```
f0 = 325e9;
dev = 1.0e6;
rate = 100e3;
P = 10.0e-3;
r = 1.0e-2;
T = 300;
P_mm = 40e-3;
omega0 = 2*pi*f0;
depth = 2*pi*(24*dev);

% Define the number of molecules per unit volume, Eq. 3.25 from GC
N = 9.68e18 * P_mm/T;
E1 = h * c * 6 * (100);
N1 = N * exp(-E1/(k*T));
N2 = N * exp(-(E1 + h*f0)/(k*T));
delta_N_eq = N1 - N2;

% Calculate E field amplitude
E0 = sqrt(2*mu0*c*P/(pi*r^2));

% Define initial conditions
p1_0 = 0;
p2_0 = 0;
p3_0 = delta_N_eq;

% Read in experimental data
sig = dlmread('signal40.txt');

% Set up time base adjustment
t_a = 0;

% Solve Bloch equations
tmax = sig(10000,1) + t_a;
tspan = sig(:,1) + t_a;
p0 = [p1_0 p2_0 p3_0];
[t,p] = ode45('dpdt', tspan, p0, [], T1, T2, kappa, E0, delta_N_eq,...
   tmax, omega0, depth);

% Extract imaginary (quadrature) component of the polarization and
% normalize.
p_i = p(:,2)./(max(p(:,2)) - min(p(:,2)));

if filt
    % Apply BP filter and plot response
    fp_i = filter(bp_filter,p_i);
```

```
    % Calculate the FFT
    pfft = fft(fp_i,nfft)/nfft;

else
    % Calculate the FFT of simulation signal
    pfft = fft(p_i,nfft)/nfft;
end;

% Plot sig and p_i
subplot(2,1,1),plot(t,p_i,t,sig(:,2));
title('Plot of Experimental Data and Simulation Results - ...
   Transient response for 325 GHz at 40 mTorr - Simulation T2 = 130 ns');
xlabel('t(sec)');
legend('Simulated','Experimental');
axis tight;
grid on;

% Plot residual
res = p_i - sig(:,2);
subplot(2,1,2),plot(t,res);
title('Plot of Residual');
xlabel('t(sec)');
ylabel('Residual');
axis tight;
grid on;

% Display rms of the residuals and FWHM at current T2
res = res.^2;
sqrt(mean(res))
FWHM = 1/(pi*T2
```

Matlab file dpdt.m

```
function [d_dt] = dpdt(t, p, flag, T1, T2, kappa, E0, delta_N_eq,...
   tmax, omega0, depth, hbar)

% Optical Bloch equations:  Brailovsky et al., Measurement of the Power
% Density of Electromagnetic Radiation by the Method of Microwave
% Nonstationary Spectroscopy, Rad. Phys. and Quant. Elec., 47(10-11),
% 916-920(2004).

% p(1) is Pr, p(2) is Pi, p(3) is hbar*delta_N/4

d_dt = [-delta_omega(t,tmax,omega0,depth)*p(2) - 1/T2*p(1);
        delta_omega(t,tmax,omega0,depth)*p(1) - 1/T2*p(2) - kappa^2*E0*p(3);
        E0*p(2) - (p(3)- delta_N_eq)/T1];
```

Matlab file delta_omega.m

```
function d = delta_omega(t, tmax, omega0, depth)

% Calculates delta_omega at time t where delta_omega is the frequency
% difference between the current frequency, omega, and the resonant
% frequency, omega0.
%
% t = current time
% tmax = maximum time
% omegao= center frequency
% depth = modulation deviation +/- from omega0
% omega = current frequency

omega = omega0 + depth*(t/tmax);
d = omega - omega0;
```

Matlab file bp_filter.m

```
function Hd = bp_filter
%BP_FILTER Returns a discrete-time filter object.

%
% M-File generated by MATLAB(R) 7.7 and the Signal Processing Toolbox 6.10.
%
% Generated on: 16-Apr-2010 11:13:24
%

% Butterworth Bandpass filter designed using FDESIGN.BANDPASS.

% All frequency values are in kHz.
Fs = 1000000;  % Sampling Frequency

Fstop1 = 0.8;         % First Stopband Frequency
Fpass1 = 4;           % First Passband Frequency
Fpass2 = 2000;        % Second Passband Frequency
Fstop2 = 10000;       % Second Stopband Frequency
Astop1 = 140;         % First Stopband Attenuation (dB)
Apass  = 1;           % Passband Ripple (dB)
Astop2 = 140;         % Second Stopband Attenuation (dB)
match  = 'stopband';  % Band to match exactly

% Construct an FDESIGN object and call its BUTTER method.
h  = fdesign.bandpass(Fstop1, Fpass1, Fpass2, Fstop2, Astop1, Apass, ...
                      Astop2, Fs);
Hd = design(h, 'butter', 'MatchExactly', match);

% [EOF]
```